TIP-BASED NANOFABRICATION AND ELECTROMECHANICAL PROPERTIES OF GRAPHENE

A Dissertation

Presented to the Faculty of the Graduate School

of Cornell University

In Partial Fulfillment of the Requirements for the Degree of

Doctor of Philosophy

by

Hadi Hosseinzadegan

August 2013

TIP-BASED NANOFABRICATION AND ELECTROMECHANICAL PROPERTIES OF GRAPHENE

Hadi Hosseinzadegan, Ph. D.

Cornell University 2013

This thesis describes the work on three categories in top-down approach in nanotechnology: tip-based nanofabrication tools, study on properties of 2D material, graphene, and making devices based on graphene. After describing the working principals of nano optical ruler imaging system (NORIS), modification and improvement of NORIS are described. Then, the NORIS hybrid with commercial nano-imaging tool, the Veeco 3100 AFM/STM tool is described. A wireless image transmission by CC2530 chip for low-noise displacement measurement in this hybrid is described. Next, the piezoresistivity and gauge factor of graphene/silicon-nitride membrane composite are measured and found to be exceptionally high compared to the currently utilized piezoresistive materials such as poly-silicon, and other graphene piezoresistivity results. Fabrication of silicon-nitride membrane with graphene samples, transferred on top of this device is described, followed by describing the measurement setup for piezoresistivity measurement of graphene/Si_xN_y stack. With ultra-high piezoresistivity, measured for this stack, fabrication and measurement of strain gauges is described. Next, scanning probe based nano etching of graphene samples is introduced. Subtractive mass removal using the tip-based graphene etching is used to tune micro electro mechanical (MEMS) resonator with 7.6ppm resolution.

BIOGRAPHICAL SKETCH

Hadi Hosseinzadegan joined thin film laboratory (TFL) at school of electrical and computer engineering, University of Tehran, Tehran, Iran in 2002. During his undergraduate, he worked on implementation of plasma enhanced chemical vapor deposition (PECVD) system for carbon nanotube (CNT) growth. Then, he focused on using vertically aligned CNTs for gated-field emission devices fabrication. Finally, he used these field emission sources to perform nanolithography with resolutions better than 100nm. He received his Bachelor of Science in electrical engineering at University of Tehran, Iran in 2006. He joined the same lab during his masters and worked on fabrication of silicon nanowires using vertical etching of silicon.

He received his Master of Science in electrical engineering at University of Tehran, Iran in 2009 and subsequently moved to Cornell University in Ithaca, New York to work toward a Doctor of Philosophy in Electrical Engineering working with Professor Amit Lal in *Sonic*MEMS laboratory.

To my wonderful wife, Baran

and my beloved parents, Vida & Manouchehr.

ACKNOWLEDGMENTS

I would like to thank my Ph.D advisor, Professor Amit Lal, for his guidance and support through the years. Amit has been a great motivator and advisor during my time here at Cornell. I would also like to thank my committee members, Professor Farhan Rana and Professor Paul McEuen for their advice during my Ph.D. time.

All the members of *Sonic*MEMS who have put up with and helped me: Norimisa Yoshimizu, Serhan Ardanuc, Manoj Pandey, Janet Shen, Alper Bozkurt, Kursad Araz, Steven Tin, Siva Prasad, Kwame Amponsah, Sarvani Piratla, Larry Lu, Yue Shi, Vahnood Pourahmad, Ved Gund, Po-Cheng Chen, Jason Hoople, Justin Kuo, Bobby Nijjar, Sachin Nadig, June Hwang, and specially Kyu Jun Cho who helped me a lot with NORIS modification and NORIS-Veeco hybrid design.

I'd also like to thank my summer intern, Brian Schiffer, who helped me with wireless imaging coding, my 2011 REU student, Cassandra Todd, who helped me with graphene/silicon-nitride membrane fabrication, and my other collaborators on TBN, Professor Clifford Pollock, Professor Sunil Bhave, Professors Chung-Hoon Lee, Prof. Jiwoong Park, Bryan Hicks, and Mark Levendorf.

Cornell ECE has been a great place for me to study and perform research during my PhD and I'd like to thank all ECE faculties, especially Professor Tsuhan Chen, Professor Ehsan Afshari, Professor Alyosha Molnar, Professor Michael Spencer, Professor Michal Lipson, Professor Sheila Hemami, and Professor David Delchamps.

I would like to acknowledge the technical and administrative staff of Cornell NanoScale Science & Technology Facility, Cornell Center for Materials Research, and Georgia Tech cleanroom for providing me the great nanofabrication and measurement tools during my PhD. I'd also like to thank Professor Gary Fedder and Kristen Dorsey in Carnegie Mellon University for their help for my TSMC chip designs.

Many thanks to my wonderful wife, Baran who was always understanding and supportive…

Lastly, I would like to thank my parents who were always kind and lovely and supported me through my entire life.

TABLE OF CONTENTS

LIST OF FIGURES

LIST OF TABLES

CHAPTER 1

INTRODUCTION

This thesis examines the tip-based nanofabrication methods, tools, and devices with applications that use multi-layer graphene films as a test material. Chapter 2 introduces the integration of NORIS [1] (Nano Optical Ruler Imaging System) with commercial Veeco 3100 AFM. An implementation of a robust noise insensitive NORIS that can be adapted to most AFM systems. In addition, we present a piezoresistive AFM tip that is used to demonstrate AFM operation using NORIS. In this new system, a Veeco 3100 AFM is integrated. Furthermore improved vibration isolation of 2× compared to previous NORIS is obtained. A unique combination of metal and elastomeric interfaces is used to reduce mechanical coupling from the base. NORIS optical pattern is projected over the entire AFM stage. Furthermore, piezoresistive AFM tips with force sensitivity of 0.625 V/N and a noise sensitivity of 17.5 μV/nN is developed and integrated with NORIS.

In Chapter 3, we talk about electromechanical properties of multi-layer graphene and measurement of ultra-high piezoresistivity for graphene. We report the first-ever use of graphene as a piezoresistive element in a MEMS device, and report on a giant piezoresistivity in the graphene films used on our devices. In this chapter, we report a

very high piezoresistive gauge factor of $1.8\times10^4$for the graphene/silicon-nitride hybrid composite plate. This gauge factor is orders of magnitude higher than that of most piezoresistive materials used in MEMS, and is much higher than that of reported for graphene films alone. This high value of piezoresistivity could be transformative in reinterpretation of the use of piezoresistivity for various hybrid transduction approaches.

Chapter 4 describes the realization of ultra-high gauge factor graphene/silicon-nitride hybrid based strain sensor, used to transduce pressure. We demonstrate the first-ever pressure sensor utilizing graphene piezoresistors demonstrating the sensitivity as high as 323 μV/V/mmHg. This sensitivity is two orders of magnitudes higher than the commercial Omega PX140x series and 36 times higher than that of the reported SWCNT (single-wall carbon nanotube) transducers [1]. Our sensor consists of a 400nm Si_xN_y membrane on silicon substrate with 5nm/20nm thick Cr/Ti electrodes on top where the graphene layer is transferred on top of this structure. Our sensor is highly nonlinear pressure sensor, with voltage signal provides absolute value of the pressure with different sensitivities for negative and positive pressures. The high sensitivity might still be useful for applications where sensitivity is more important than linearity. Finally, in Chapter 5, precision patterning of multi-layer graphene and frequency trimming of graphene based MEMS resonator are introduced. We report ultra-precise silicon-nitride membrane resonance frequency trimming by

atomic-level graphene removal using tip-based electrolytic etching. We placed the graphene films over the electrodes defined over lows-stress Si_xN_y membranes using a film transfer method. In this method, the graphene film is poly-crystalline with a grain size in the range 50- 800 nm, and can be two or three layers thick. Removing nanometers of graphene film, results in atomic-scale mass control. Using tip-based graphene removal, we report frequency shifts as low as 7.6 ppm by etching graphene films, using STM based anodic reaction.

CHAPTER 2

NANO OPTICAL RULER IMAGING SYSTEM MODIFICATION AND INTEGRATION FOR TIP-BASED NANOFABRICATION

One of the central problems with tip-based nanofabrication is the ability to keep the tip position stable and precisely at a given location after repeated motions, over the time required to nanofabricate over a macroscopic sample. This manufacturing time can be several minutes to hours and stage position accuracy has to be maintained within sub-Angstrom accuracy for atomically precise fabrication. Increasing throughput is also greatly desired to make tip-based nanofabrication a practical technique. One method to increase the throughput is to realize a number of AFM tips operating and moving independently yet with precise distances maintained between the tips. Fundamental science measurements using tools like AFM also benefit from improvements in tip position metrology. For example, being able to measure a gap stably over hours could yield information about effects of very slow surface forces.

While micro- and nanotechnology allows us to manipulate surface with scanning probes at atomic dimensions, it is not possible to do so with precision over large areas such as a 4-inch wafer or even a die, mainly due to the long term hysteresis and positioning accuracy of nano-motion stages. Previously, the Nano-Optical Ruler Imaging System (NORIS [1]) has been introduced, in which an atomically stabilized

laser wavelength is used as a distance-constant. The atomically stabilized light is diffracted through a temperature-stabilized micro-fabricated grating; define a projected ruler onto the space where nanomanipulation occurs. An imager chip intimately attached to the AFM tip can tell tip position by optical correlation of the measured image with the expected diffraction pattern. Using NORIS along with a novel nanodevice synthesis tools will be described in this chapter that enables precision placement, fabrication, and characterization of in-situ synthesis of nanostructures. Also, application of NORIS in positioning of an AFM tip will be described.

2.1 Deflection measurement in commercial AFM tools

In AFM systems, in addition to positioning the tip, the problem of measuring the atomic force induced deflection of the cantilever beam is required. All the present methods use some external physical component which is brought close to the cantilever for measuring defection. The most commonly used technique is to focus a laser beam onto the cantilever and to measure the deflection of the reflected beam with a quadrant photodetector [2]. Although this technique is very sensitive to cantilever deflections [3], this technique requires the use of precisely aligned optical components. This introduces complications in the design and operation of an AFM. One limitation is that it is difficult to scan the cantilever because of the complexity of the deflection sensor associated with it. This normally requires that the sample be

moved while the cantilever and detector are held fixed. This requirement makes imaging of large samples only possible with the sample moving on a stage. Piezoresistive [4] cantilevers provide alternative force detection schemes in which the deflection detector is integrated in the cantilever.

Table 2-1 Comparison of different piezoresistive AFM probe fabrication methods.

Method	Sensitivity	Resolution (Force or Distance)	Application	Tip Material	Cantilever Material	Technology	Tip position	Ref
Piezoresistive and MOSFET Detection	60 µV/pN 560 mV/µm	65 pN		No attached tip		SOI	Vertical	[5]
Piezoresistive cantilever in a commercial CMOS Tech	8 µV/pN 300 µV/nm	100 pN Min= 50 pN	Intermolec-ular force detection	No attached tip		0.8µm CMOS CYE using 2 poly layers	Vertical	[6]
Piezoresistive cantilever in a commercial CMOS Tech	2.4- 11.8 µV/nN	10 pN	Intermolec-ular force detection	No attached tip	Poly	Double-poly layers	Vertical	[7]
CMOS integration with AFM and tip fabrication	1.1 µV/nm 2.5 µV/nm	3nm	Regular AFM Apps	Silicon integrated	Silicon	1) Low Temp (660 C) 2) No tip Sharpening	Front Side	[8]
Parallel AFM with on-chip CMOS	2.5 µV/nm	20- 40 Å (@ contact mode) and bandwidth : 10 kHz)	Regular AFM Apps	Diamond	n-well Silicon	2µm double-metal high voltage CMOS	Front Side	[9]
IBM Work	2-4x10^{-5} /nm	-	Data Storage	Silicon	Silicon	Tip fab: RIE/Oxide/BOE Etch	Front Side	[10]

An integrated sensor provides several advantages over conventional AFM. For example, since the cantilever can be scanned, operations in vacuum and at low temperature would considerably benefit from the lack of external deflection sensing components. Also, the AFM may prove useful in profilometry and integrated circuit inspection, over larger substrate areas.

Table 2-1 shows the comparison of different piezoresistive AFM probe fabrication methods. All fabrication methods in this table have the AFM tip and the piezoresistive network on frontside of the wafer, however, our goal is to fabricate the piezoresistive network on front side and the AFM tip on backside of the wafer. The process flow and methods of our own piezoresistive AFM probe are discussed in section 2.9 and section 2.10 respectively.

2.2 NORIS operation

The basic operating principle of this system has been developed previously by Dr. Norimasa Yoshimizu, a Cornell graduate in *Sonic*MEMS laboratory [11]. Figure 2.1 shows the block diagram of NORIS. The system includes a stabilized external laser cavity. The laser is atomically stabilized to tens of ppb. Following the laser is some optical path length, which is used to allow the laser beam to diffract and increase its beam width. Then laser is guided through a wafer for generation of the diffractive aperture array. The wafer is microfabricated with an aperture array of a reflective thin

film. The thin film pattern acts as a diffractive element, creating an optical pattern in space which is used as a nano-precise optical ruler. Its pattern in a two dimensional slice shown as a number of red spots in the plane of the scanning probe. The scanning probe, here shown as a scanning tunneling tip, is attached to an imaging camera. The camera captures an image of the optical ruler, and then uses that information to calculate its position using sub-pixel digital image processing techniques.

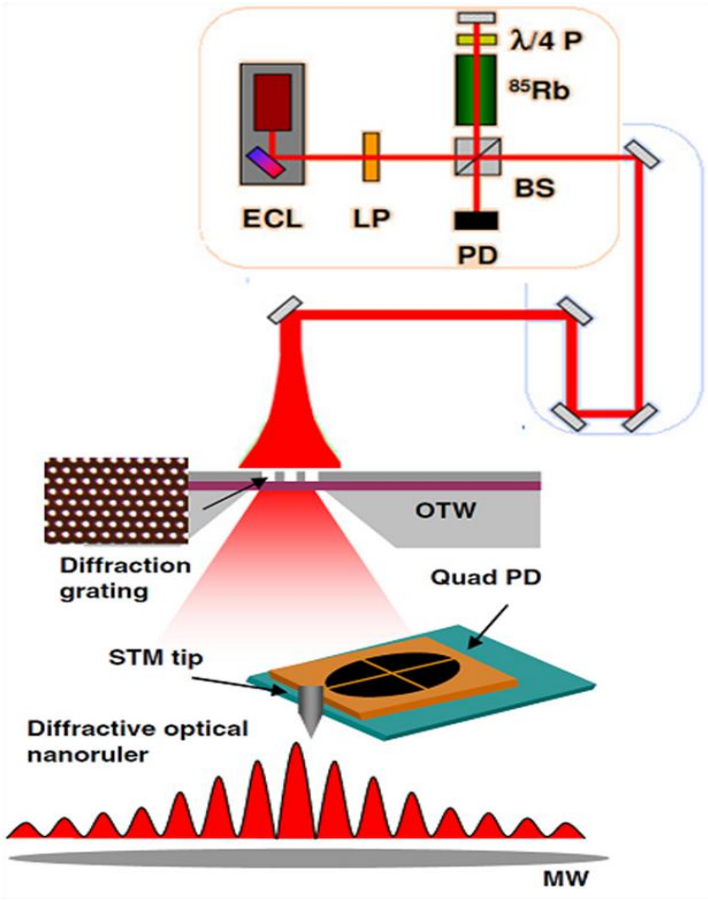

Figure 2.1 Schematic of the microfabricated diffractive optical nanoruler technology. The diffraction optical ruler is detected by a photosensitive device; a nanofabricating tip is rigidly attached to the assembly.

2.3 NORIS modification

We started to modify the NORIS and the goal of this work was to automate the NORIS by getting the calculated position from NORIS and providing the coordinates to the stage to move to the desired position [12]. The system consists of high precision laser with center primary 780 nm wavelength, a grating on a silicon nitride membrane formed with two dimensional array of holes, and a CMOS imager mounted on a piezo actuator. The various components of the system are controlled by a Labview program. The laser lock mechanism is described in section 2.4. When the laser beam hits the silicon-nitride grating, it creates a diffraction pattern projected on the CMOS imager chip mounted on the piezo actuator. The control program captures an image as a reference. Through the control program user can type in distance to actuate and after actuation it captures another image. By cross-correlating the two images (using subpixel image registration algorithm) one can find out the displacement in number of pixels and therefore the distance traveled by the piezo actuator with high precision. Because the metrological reference of the system is a light pattern created by stable laser beam from above rather than capacitive sensor, the system has the potential to realize highly accurate positioning, stable over long terms.

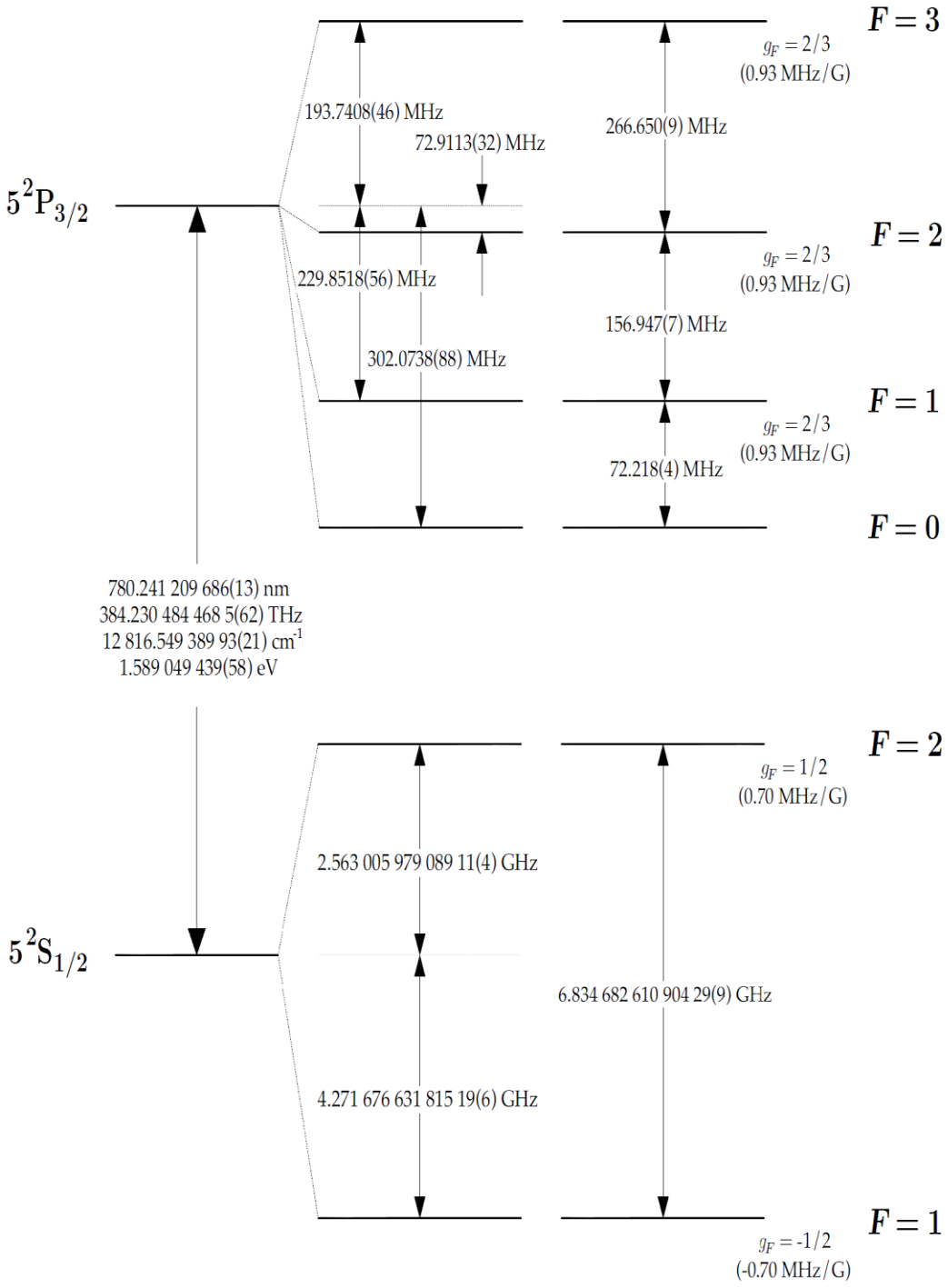

Figure 2.2 87Rb D2 transition hyperfine structure, with frequency splitting between the hyperfine energy levels [13].

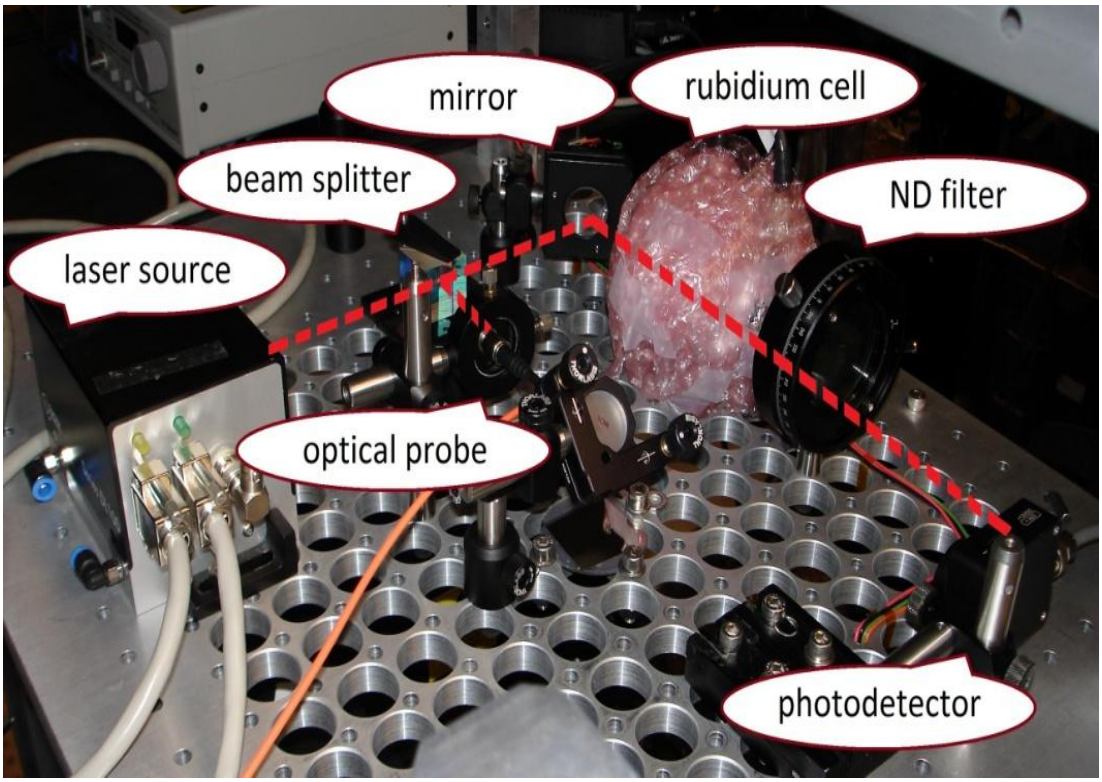

Figure 2.3 Laser setup. Path of laser is shown with red dotted line. The optical probe is connected to a spectrum analyzer. The rubidium cell is placed inside a heater which is set to 80°C and is covered with an insulator.

2.4 Wavelength-locked laser

The accuracy of NORIS is directly affected by the stability of laser that it is crucial for the laser source to generate a highly stable wavelength. For spatial frequencies of ξ in the diffraction pattern, long distances are measured by $L = N/\xi$ where N is the number of times the sinusoidal components of ξ repeat while traveling L. Since $\xi = 1/\lambda$ by definition, L can be rewritten as $L = N\lambda$, and therefore the expression $\delta L/L = \delta\lambda/\lambda$ is valid. If the wavelength changes then the phase of the beam at distance L also

changes and this causes change in intensity measurement at that position even if the amplitude of the beam is fixed. This also means that positioning with 10 nm precision over a 200 mm wafer area requires a laser stability of 50 ppb [14]. However, the wavelength of laser drifts over time due to variety of reasons therefore a feedback loop is required to counter such wavelength drift and this can be achieved by locking the wavelength to where an atomic transition occurs; because atomic transitions are quantized and unique in nature, they can serve as a reference to lock a laser wavelength to. In this experiment D2 transition of rubidium 87 was used and its hyperfine structure is shown in Figure 2.2. By using D2 transition of rubidium 87 the frequency of the laser can be stabilized within 6 MHz which is equivalent to 15 ppb [1]. Figure 2.3 shows the basic setup for the experiment.

When the laser beam with ~780 nm wavelength passes through the rubidium cell (a small glass tube filled with rubidium) the rubidium atoms transit to the excited states by absorbing significant amount of energy from the beam which is shown in Figure 2.3. Such absorption can be observed by exposing a photo detector to the laser beam that went through the rubidium cell while sweeping the wavelength of the laser. If the wavelength is swept by sweeping the current of the laser which is done by applying sinusoidal modulation signal to the laser module the output signal of the photo detector will look like Figure 2.5.

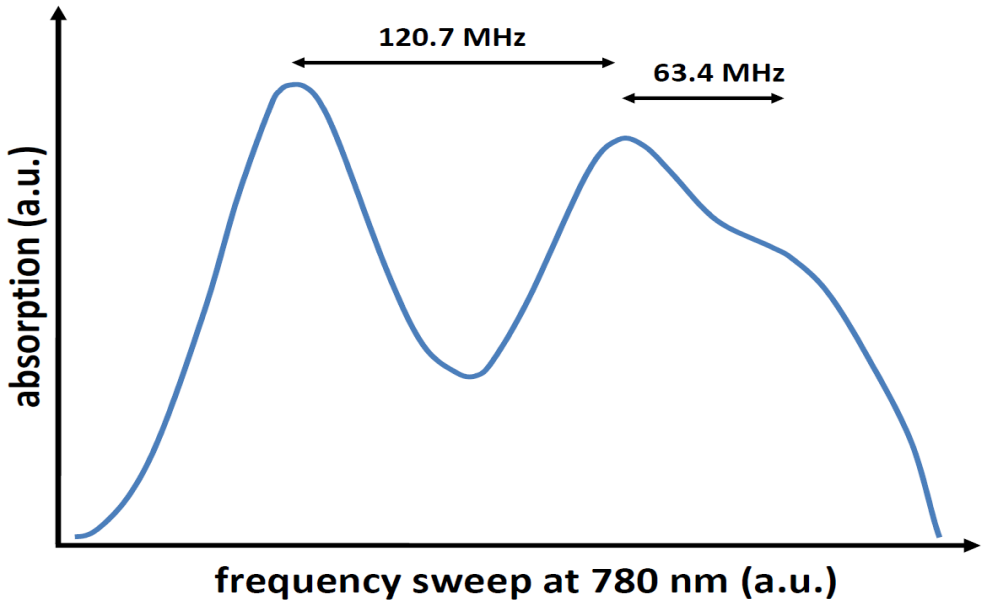

Figure 2.4 Expected absorption spectrum of rubidium at ~780nm [11]. The saturated spectrum shows the three spectral holes, corresponding to the three resonances that were assumed. Two of the spectral holes overlap.

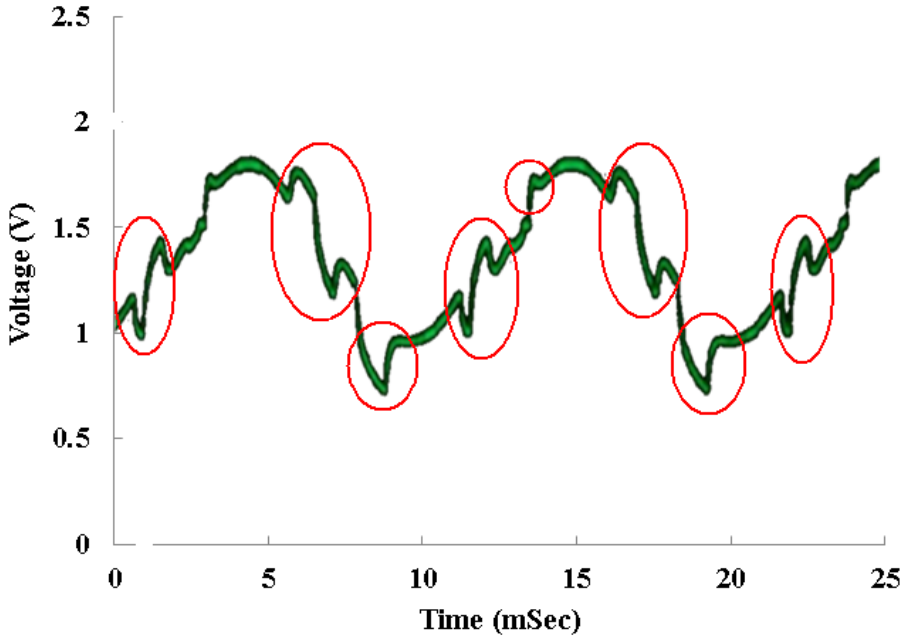

Figure 2.5 V_{PD} with wide range wavelength sweep (~3nm). Modulation frequency is 100Hz.

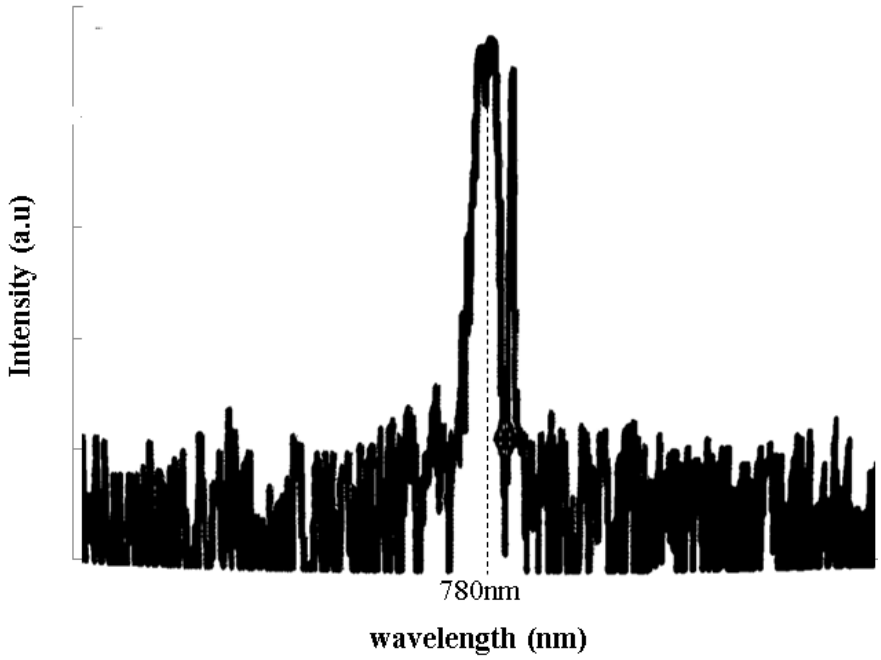

Figure 2.6 Wavelength spectrum during wide range wavelength sweep.

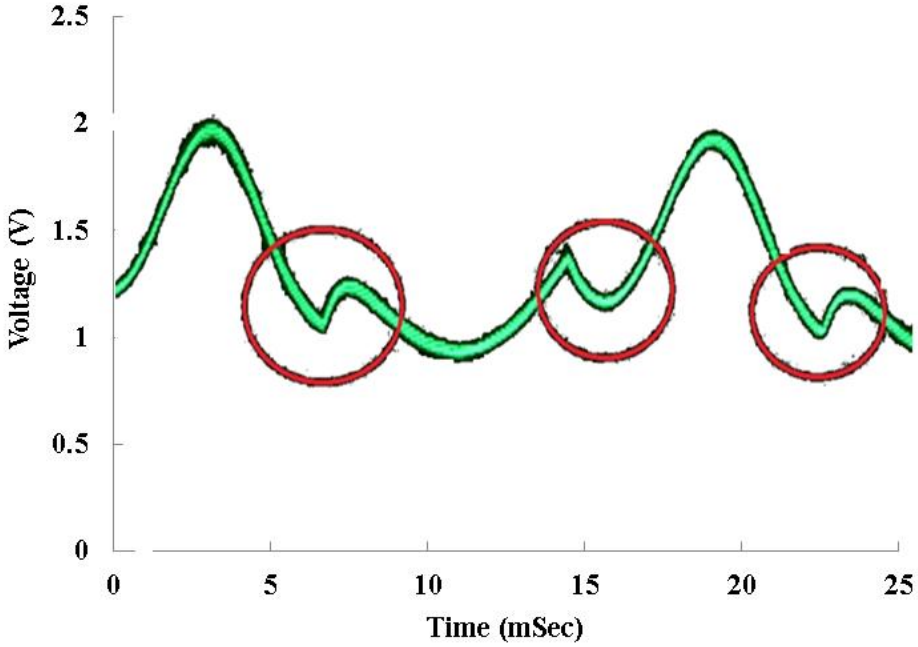

Figure 2.7 V_{PD} with narrow range wavelength sweep (< 1 nm). Absorption shown in red circles. Modulation frequency is 100 Hz.

All the glitches in Figure 2.5 represent absorptions at various atomic transitions (at different wavelength). In Figure 2.6, spectrum analyzer shows multiple peaks for wavelength components and one of them corresponds to 780.24 nm (D2 transition) in which we would like to lock onto. By applying sinusoidal modulation signal with smaller peak-to-peak voltage it is possible to reduce the sweeping range of and thus observe only one absorption signal of our interest. Figure 2.7 shows only one atomic transition which occurs around 780.24 nm. The goal of this experiment is to set the laser current to the point where such absorption is maximized and this requires a setup shown in Figure 2.8, Figure 2.9, and Figure 2.10.

If the V_{ref} is so small that it only sweeps the absorption region the lock-in amplifier will generate an output signal (V_{LIA}) that makes V_{mod} to modulate the wavelength towards the peak of absorption or another word, towards the atomic transition of our interest. Once the wavelength of the laser is locked the feedback loop will counteract any type of wavelength drift might occur over time or noise. Figure 10 shows how the feedback loop counteracts to noise signals caused by mechanical vibration (hitting the metal bar [15] shown in Figure 2.10). When the metal frame is hit the entire structure including the photodetector vibrations and this causes the amount of laser beam entering the photocell to fluctuate. Figure 2.11b shows significant change in V_{LIA} compared to that in Figure 2.11a, because V_{PD} deviates from the stable state and V_{LIA}

has to counteract. As the vibration decays V_{PD} and V_{LIA} settles down to the stable state and the wavelength of the laser remains the same because of the counteraction by V_{LIA}. Figure 2.12 shows that the wavelength of the laser after shock resistance experiment remains the same.

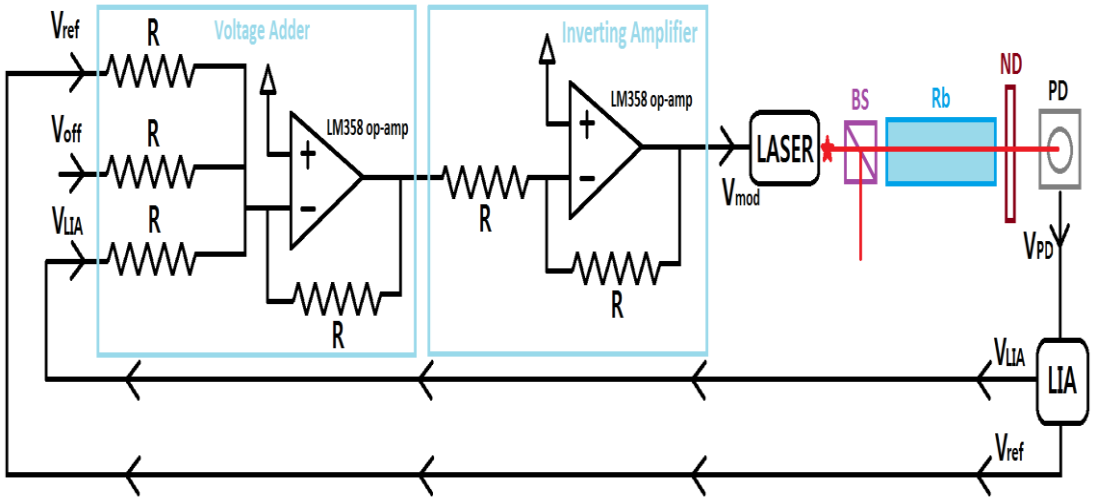

Figure 2.8 Circuit diagram for experimental setup. Refer to appendix A.1 for theoretical backgrounds of this setup. Refer to appendix A.2 for input signals and data acquired from this setup.(PD: photodetector. LIA: lock-in amplifier. BS: beam splitter. ND: neutral density filter.V_{ref}: sinusoidal reference signal. This is the main signal that sweeps the laser current. V_{off}: Offset voltage. Center wavelength can be set with this signal. V_{LIA}: Output signal from the lock-in amplifier. V_{PD}: Output of photodetector. V_{mod}: modulation signal for laser current. Wavelength of laser can be swept using this signal. R= 1kΩ)

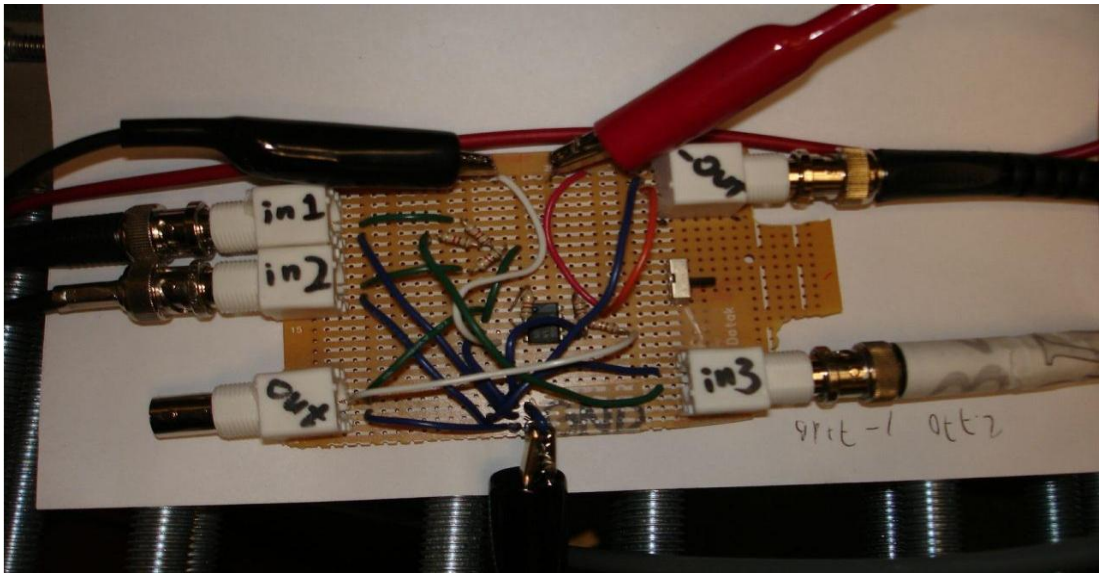

Figure 2.9 Voltage adder shown in Figure 2.8. LM358 op-amp was used. in1, in2, and in3 are V_{ref}, V_{off}, and V_{LIA}, respectively.

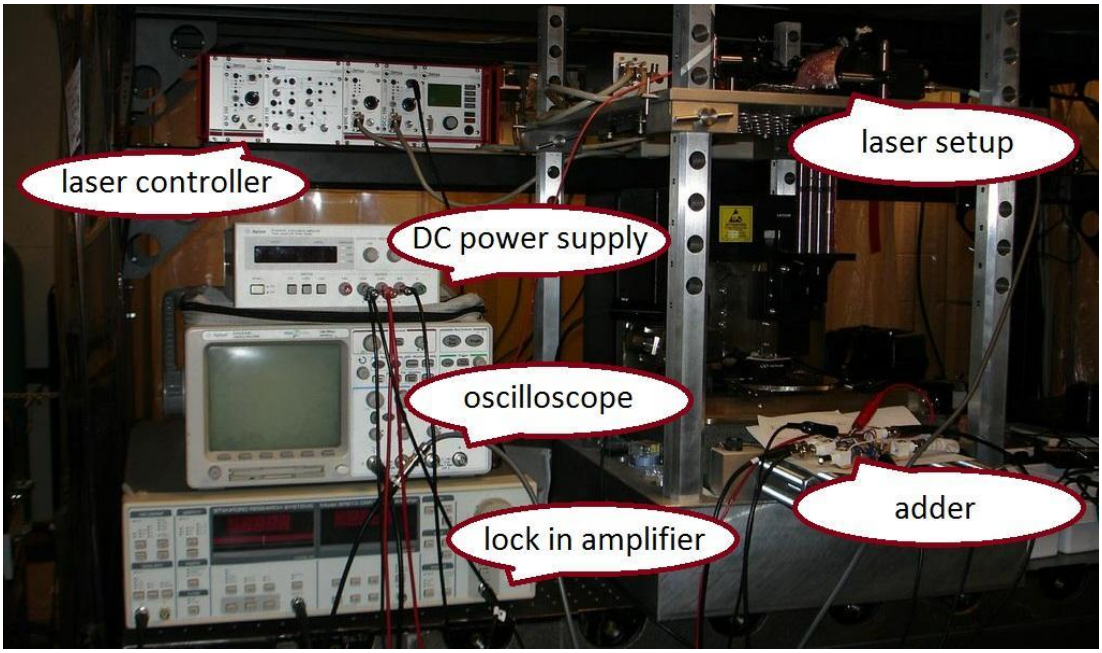

Figure 2.10 Overview of the entire setup. Detailed laser setup is shown in Figure 2.3

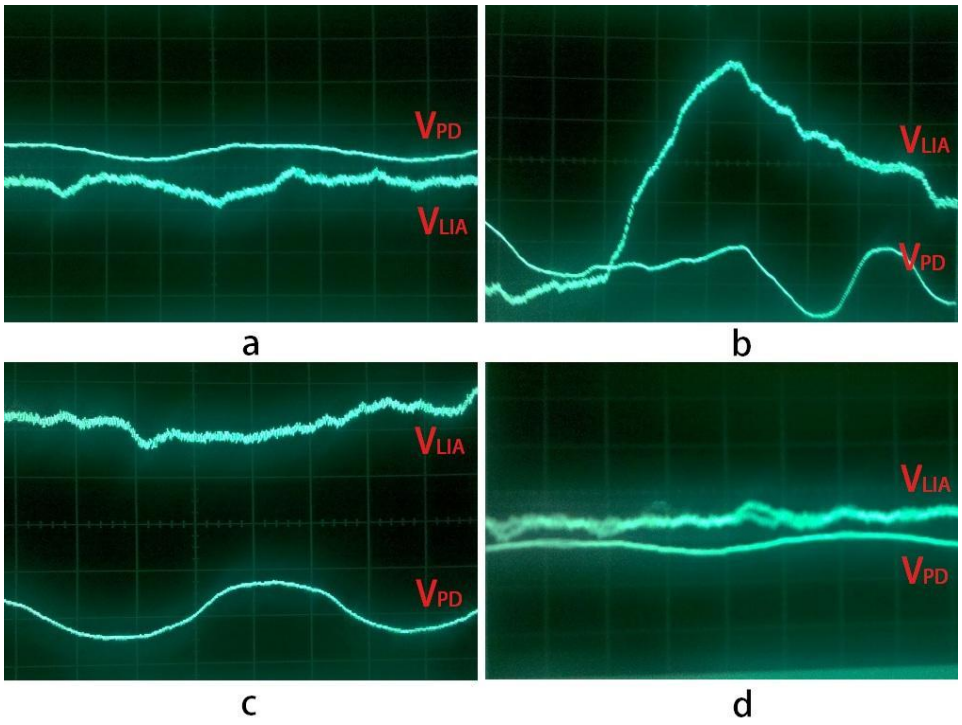

Figure 2.11a. stable state. b. vibrational noises were added (shock). c. counteraction. d. stable state (scale: 1 mv for each grid)

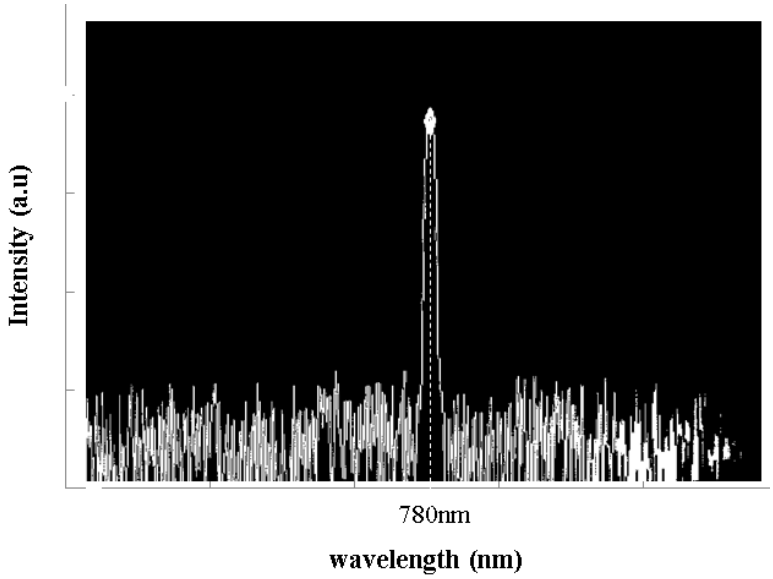

Figure 2.12 Wavelength of the laser after shock resistance experiment which is the same as before.

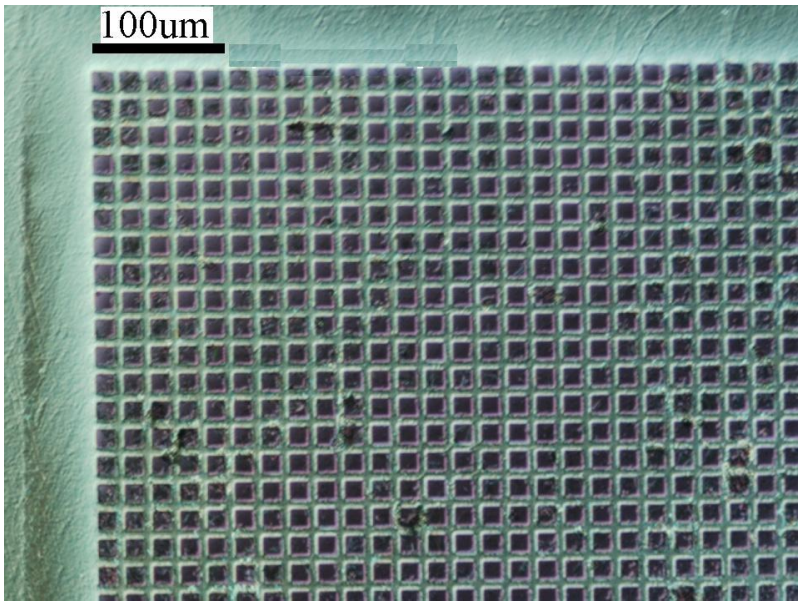

Figure 2.13 Grating on silicon nitride membrane.

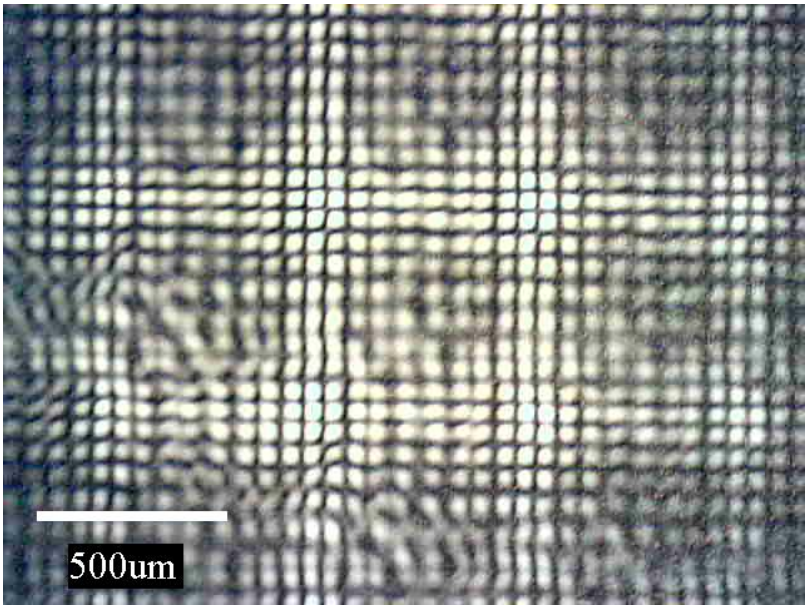

Figure 2.14 Diffraction pattern of the grating with z distance of 32cm between the grating and CMOS imager.

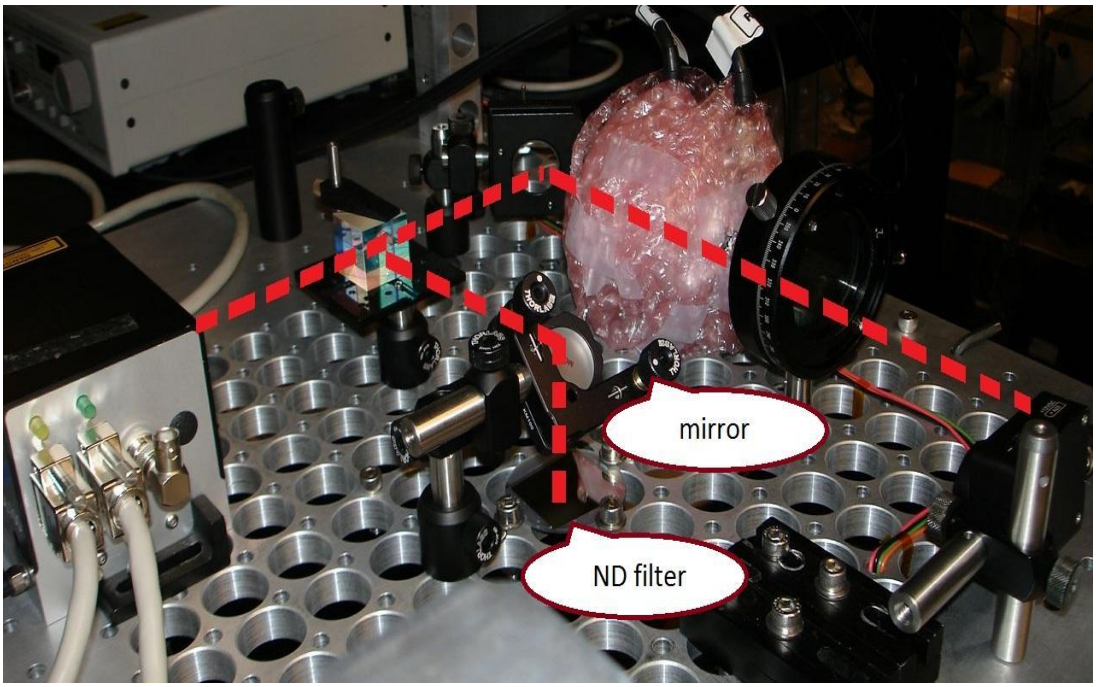

Figure 2.15 New laser setup. Optical probe is removed. Path of laser is shown with red dotted line. ND filter is placed in order to reduce the power of the beam. If the power of the beam is too strong the diffraction pattern will not be acquired by imager properly due to high intensity of the beam.

2.5 Prototyping NORIS

2.5.1 Hardware

By combining the stabilized laser with grating, imager, and piezo actuator, a nanopositioning system can be built. The first step is to redirect a portion of the laser beam to a grating.

The grating (Figure 2.13) can be fabricated by making periodic holes to a silicon wafer and its diffraction pattern is shown in Figure 2.14. The setting of laser is very similar to Figure 2.3 except that now the optical probe is removed and the beam that

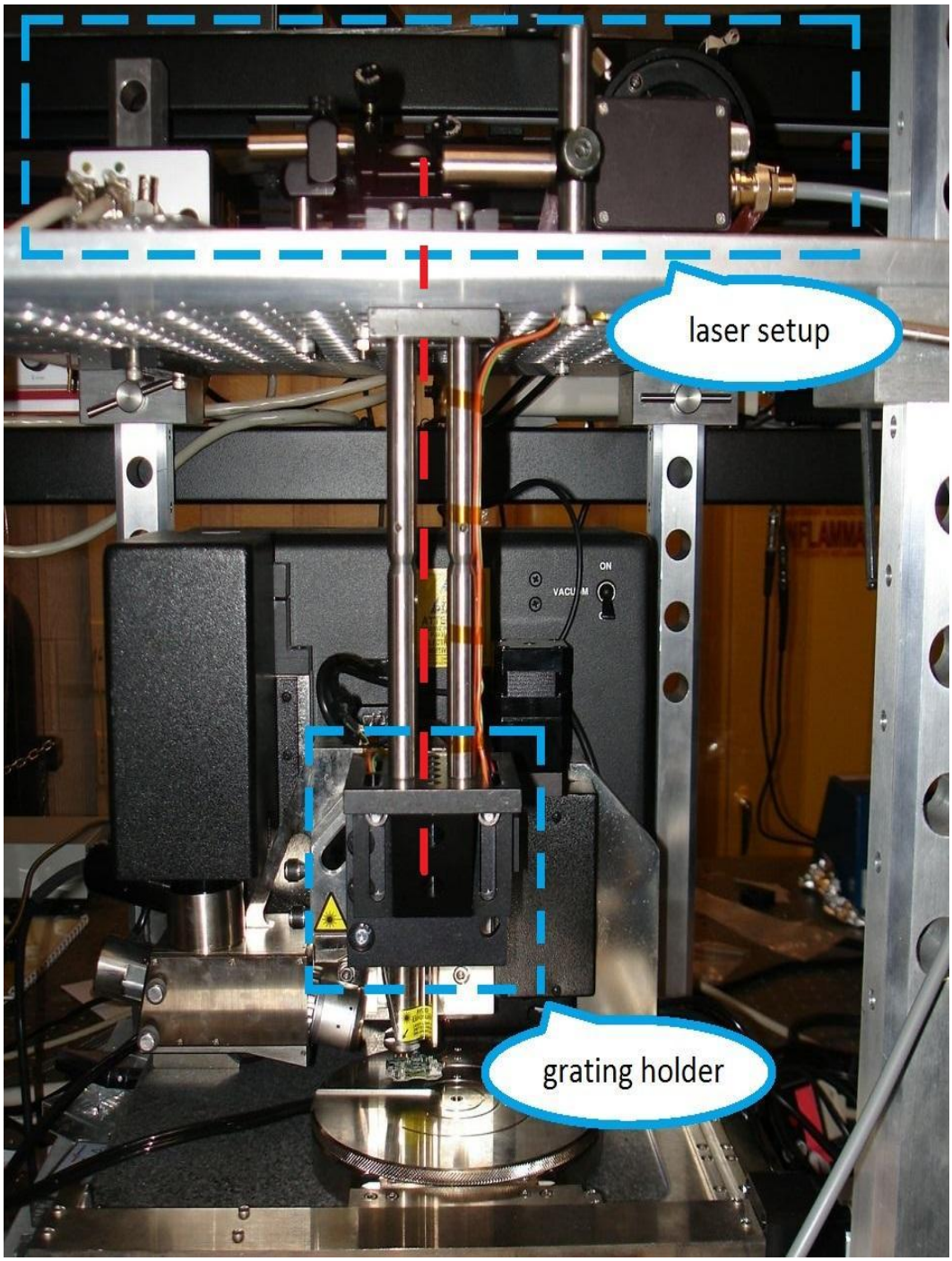

Figure 2.16 Laser setup and grating. Path of laser is shown with red dotted line.

used to go to the optical probe is redirected downward where the grating is placed. The new setup is shown in Figure 2.15.

The grating holder is placed along the path of the beam right beneath the laser setup as shown in Figure 2.16 and the actual grating is mounted inside of a peltier cooler which is required to minimize the thermal expansion of the grating by the laser beam (Figure 2.17). With this setting diffracted beam will shine upon the area right under the grating and this is where the imager with piezo actuator is placed. (Figure 2.18 and Figure 2.19)

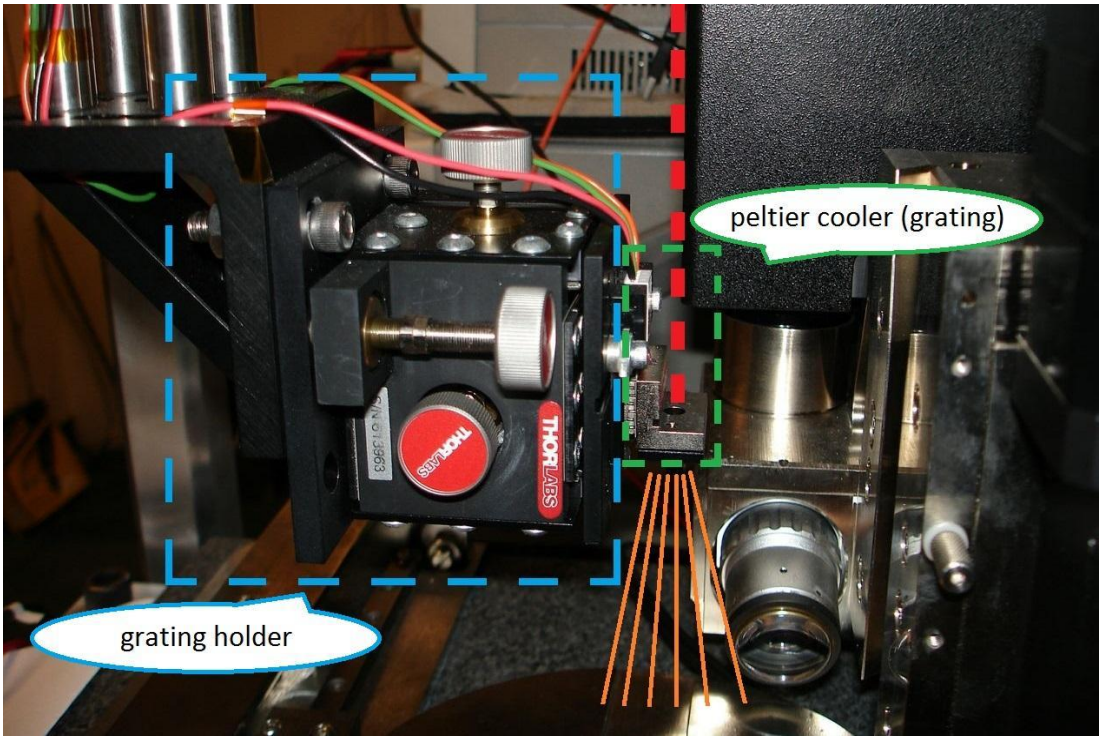

Figure 2.17 Grating holder. Side/zoomed view of Figure 2.16. Path of laser is shown with red dotted line. Path of diffracted pattern is shown with orange lines.

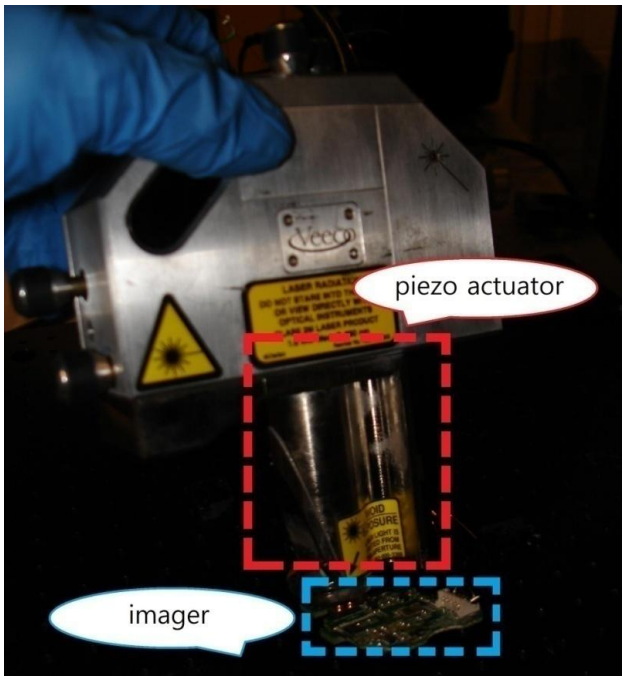

Figure 2.18 The imager is attached to the piezo actuator.

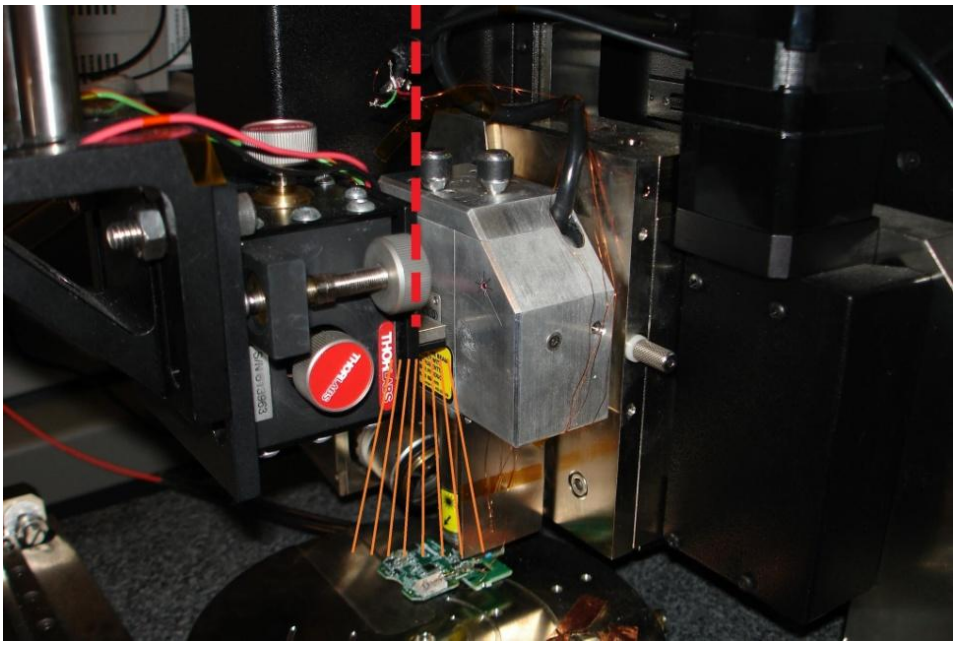
Figure 2.19 The imager is placed right beneath the grating. Path of laser is shown with red dotted line. Path of diffracted pattern is shown with orange lines.

The PCB is designed such that it fits within the commercial Veeco 3100 AFM tool and captures the diffraction pattern, created by NORIS on top of mechanical structure. Figure 2.20 shows the schematic of the Veeco 3100 actuator, before and after integrating the Veeco3100 system with NORIS. As one can see in this picture, the diffraction pattern is captured by CMOS imager and sent to the wireless microcontroller to transmit the imager data as well as piezoresistive AFM probe deflection signal to the computer. The entire CMOS imager and CC2530 microcontroller modules are powered by a 2.5V battery.

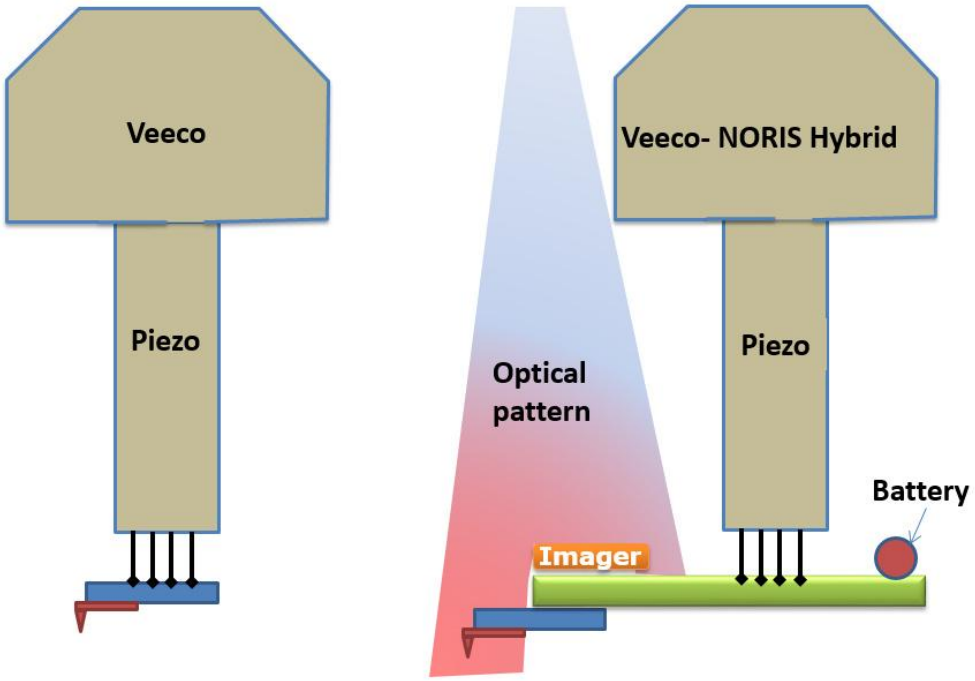

Figure 2.20 Schematic of Veeco3100 piezo actuator holding the AFM/STM probe (left) and Veeco-NORIS hybrid with custom designed PCB which includes the AFM/STM probe, CMOS imager, CC2530 wireless microcontroller, and battery.

Figure 2.21 shows the PCB with custom shape to fit into the piezo actuator of the Veeco3100. Probe mount section in this PCB is designed such that it can hold standard Veeco AFM/STM probes too. This gives us ability to compare the resolution we get from our fabricated probes and available commercial ones.

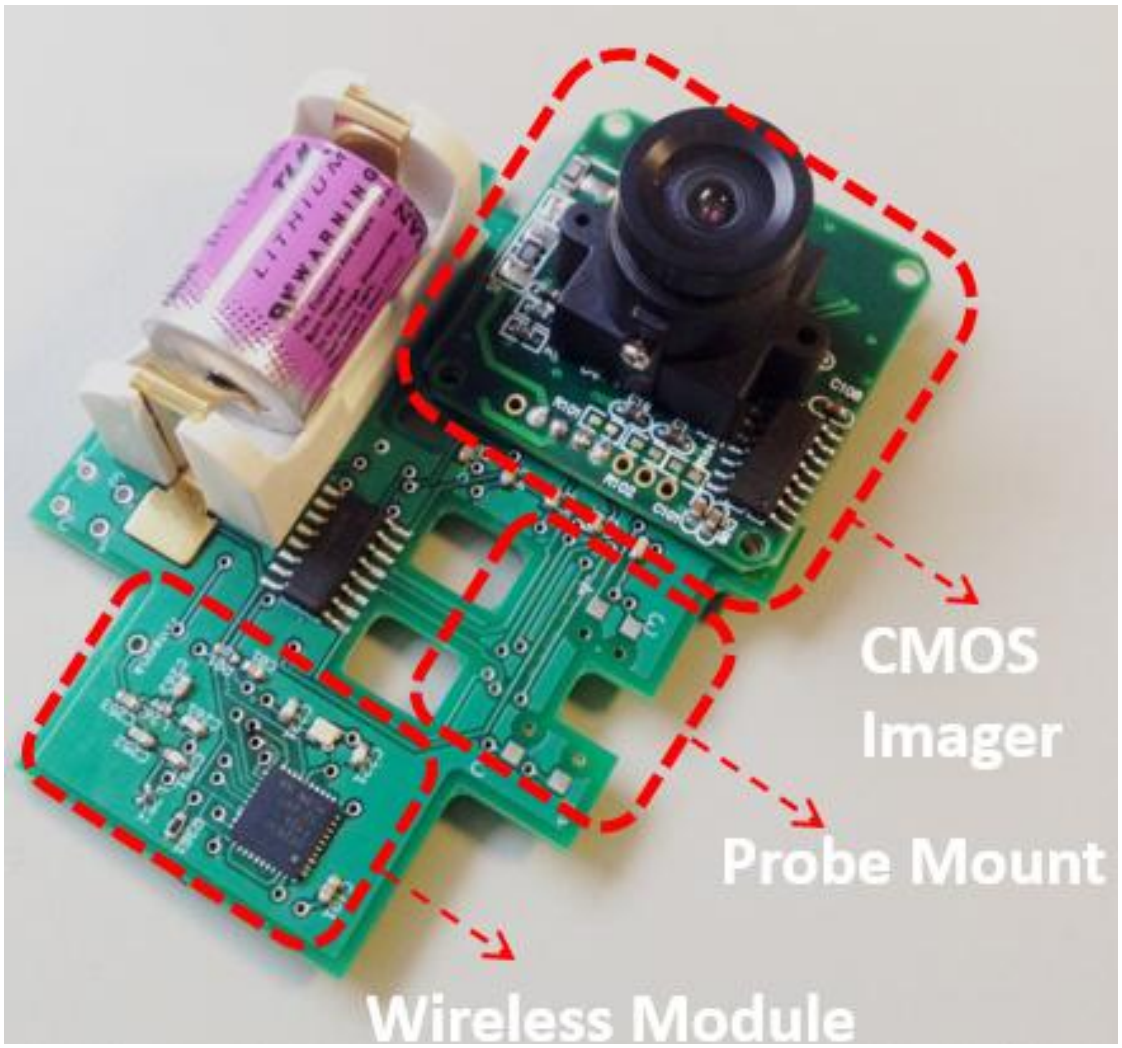

Figure 2.21 Custom designed PCB which captures the signals from CMOS imager and piezoresistive network of the AFM probe and sends them to the wireless module (cc2530 chip)) to transmit the signals to the computer for image and deflection analysis.

After placing the battery into the PCB, it can be easily plugged into the Veeco3100 piezo actuator. Figure 2.22 shows the mounted PCB with commercial AFM probe, plugged into the "probe mount" section of the PCB.

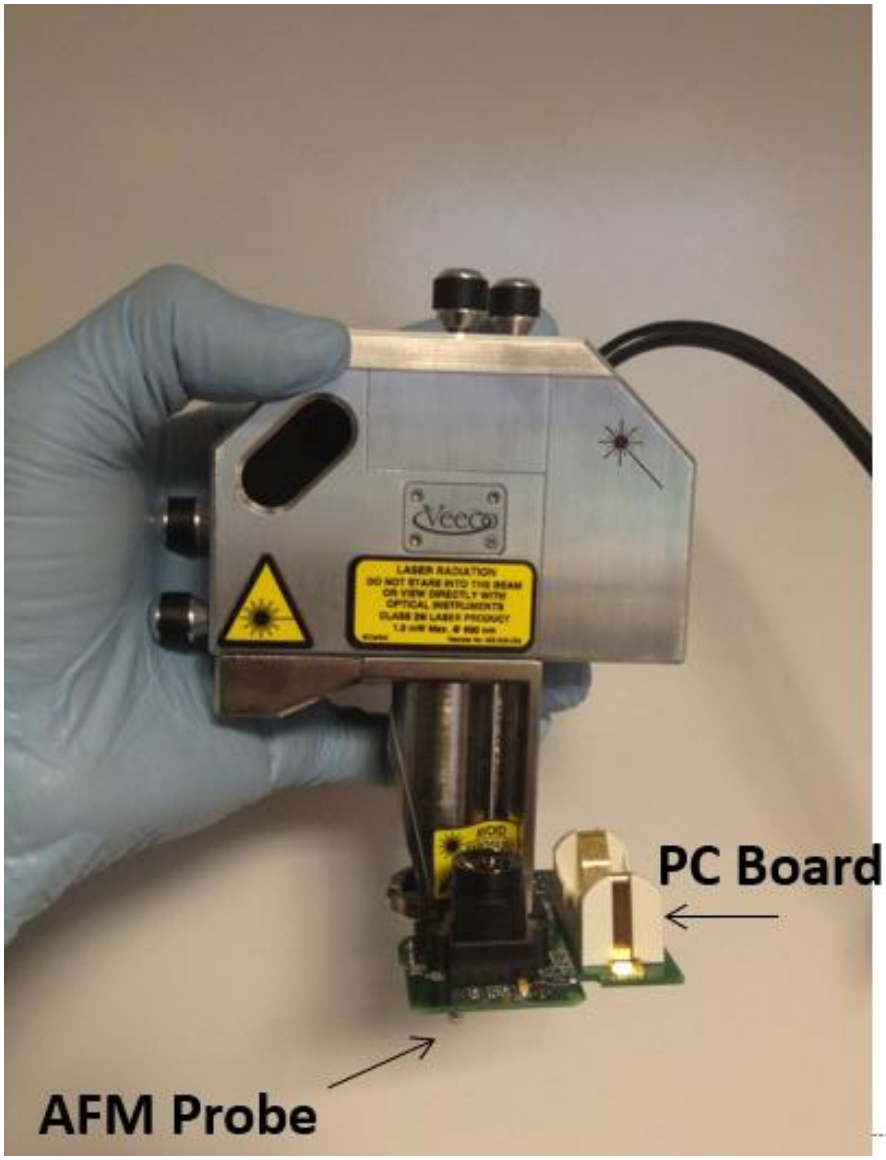

Figure 2.22 Final mount of designed PCB with imager and wireless microcontroller on Veeco3100 piezo actuator.

2.5.2 Software

NORIS is run by a Labview program that controls piezo actuator through USB-6259 data acquisition module which can apply voltages to piezo controllers, captures images, and runs image registration algorithm (refer to appendix A3). Note that capturing images and cross correlation are done by MATLAB script box inside the Labview program. Figure 2.23 and Figure 2.24 are the flow diagram and Labview front panel of the program respectively.

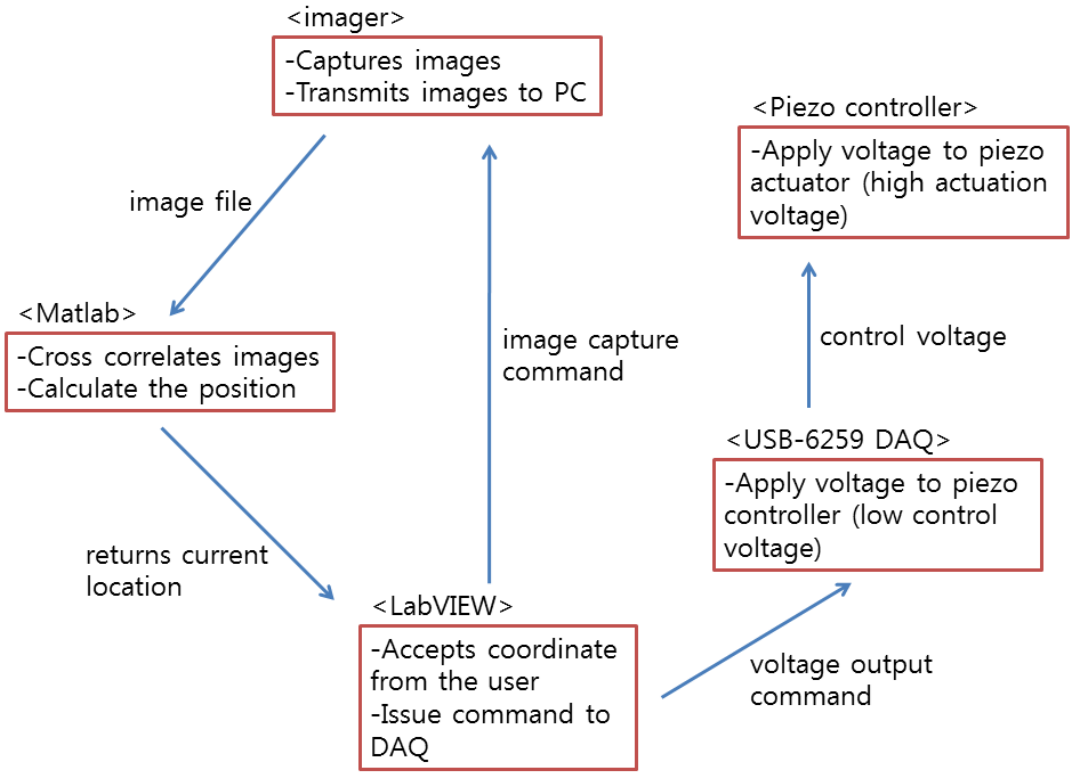

Figure 2.23 Flow diagram of the Labview program.

The program captures a reference image, move piezo actuator(and imager which is attached to the piezo actuator) by some distance that user entered, captures another image, and compare this image and the reference image to calculate the pixel shift thus, the distance traveled by the piezo actuator; the image registration algorithm used

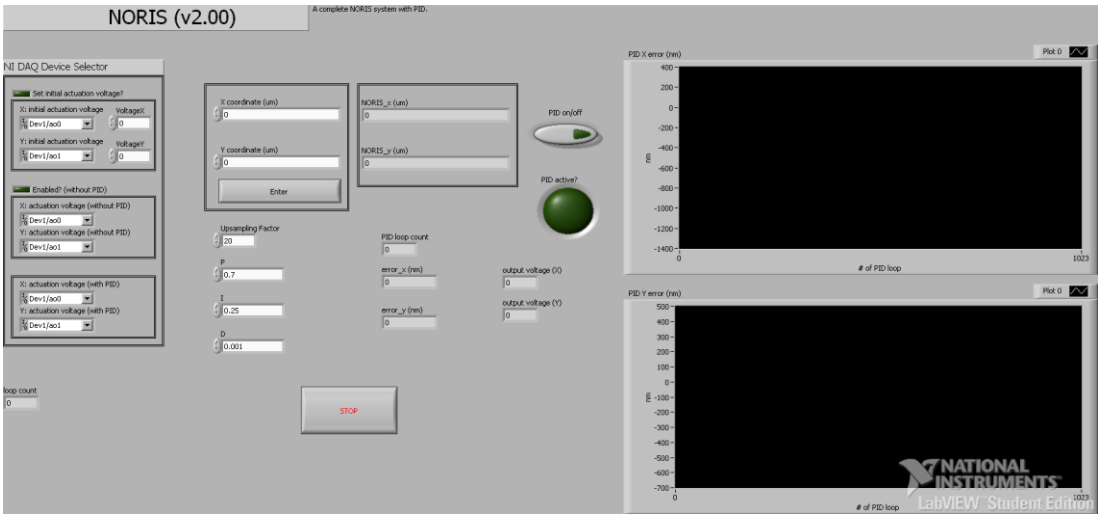

Figure 2.24 Front panel of the Labview program. Users can set the position of the piezo actuator and see the positioning error.

in this program returns difference in pixel that multiplying the size of the pixel (3.6um for the ov7670 imager) to that value gives the difference in the displacement of before and after the actuation. Because the program has PID feedback loop the position of the piezo actuator can automatically converge to the desired location that user entered.

The result of entering an arbitrary position to the program is shown in Figure 2.25. The graph represents difference between the desired position the user entered and the position calculated by the image registration algorithm, or in other words a positioning

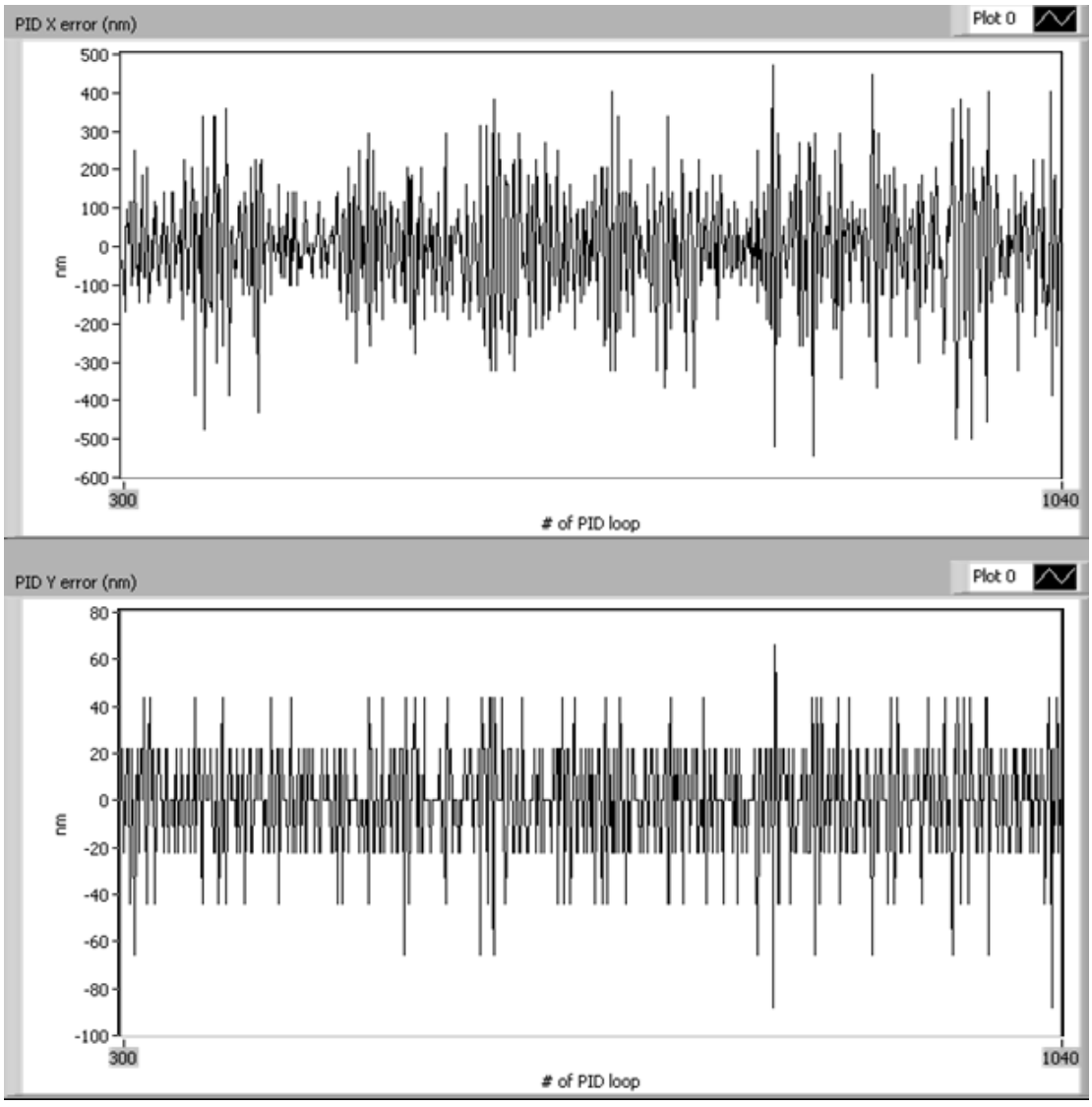

Figure 2.25 NORIS result. Top figure is error in x direction and bottom figure is error in y direction.

error while feedback loop is running to correct the error. Even with PID loop which is implemented in the program the system is showing huge errors. Since the wavelength of the laser is stable and all the parts (mirrors, beam splitter, ND filter, and grating) that affect the path of laser are tightly fixed the only possible source of error

is imager that is not tightly fixed to the piezo actuator. The piezo actuator used in this experiment is the built-in piezo actuator of a commercial atomic force microscope. Although Figure 2.18 doesn't show exactly how the imager and the piezo actuator is connected, the pins that hold the imager in current setting is meant for a probe tip for an atomic force microscope not an imager which is much heavier than a probe tip. Also, the wire connecting the imager and the computer has tension which causes torque to the imager. This problem can be solved by mounting the imager on a piezo actuator that can sustain the weight of the imager and transmit the image wirelessly. Furthermore, it is preferable to have a standalone piezo controller unlike to the current experiment setup which overrides the control protocol of a commercial atomic force microscope for actuation.

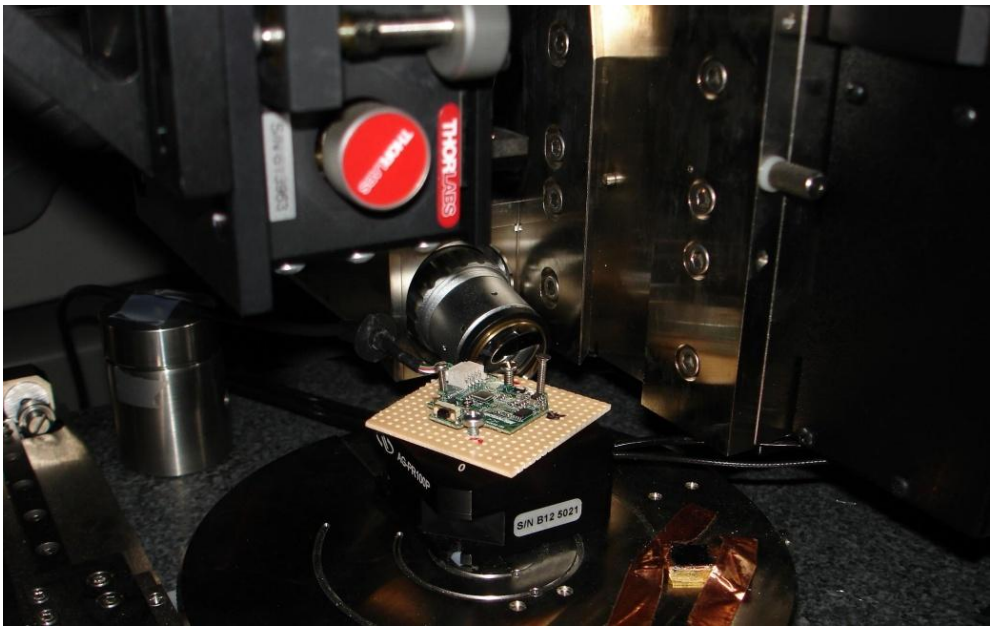

Figure 2.26 The imager is mounted on a stable structure and tightly fixed by screws.

2.6 Mechanical stabilization

To measure the error caused by the unstable mechanical interface between the piezo actuator and the imager, the imager continuously captured images for long period of time and the registration algorithm was run with a reference image (initial capture) and the rest of the images captured during that period of time one by one. This way deviation in position over time can be measured. Two types of experiments were done to observe error caused by the tension of wire and unstable interface separately.

The first experiment has exactly the same setup as the experiment from 2.5 except the imager and the computer is connected with thin wires instead of a thick USB cable. This setting causes significantly less torque than setting from section 2.6 but the interface between the imager and the piezo actuator is still mechanically unstable.

In the second experiment the imager is mounted on a stable structure and tightly fixed by screws however, he imager is connected to the computer with USB cable (Figure 2.26).

Both experiments were run for ten hours and images were captured every five minutes. The result shows that mechanically unstable interface causes vibrational noise and tension caused by the presence of data cable cause the imager to drift over time (Figure 2.27 and Figure 2.28).

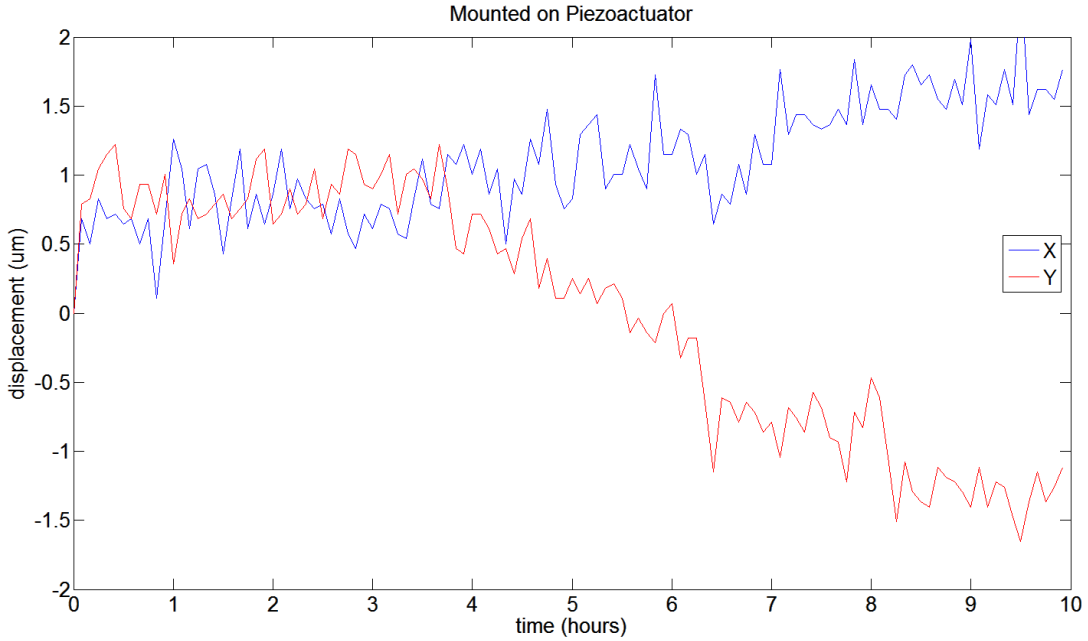

Figure 2.27 Stability test (imager is mounted on piezo actuator).

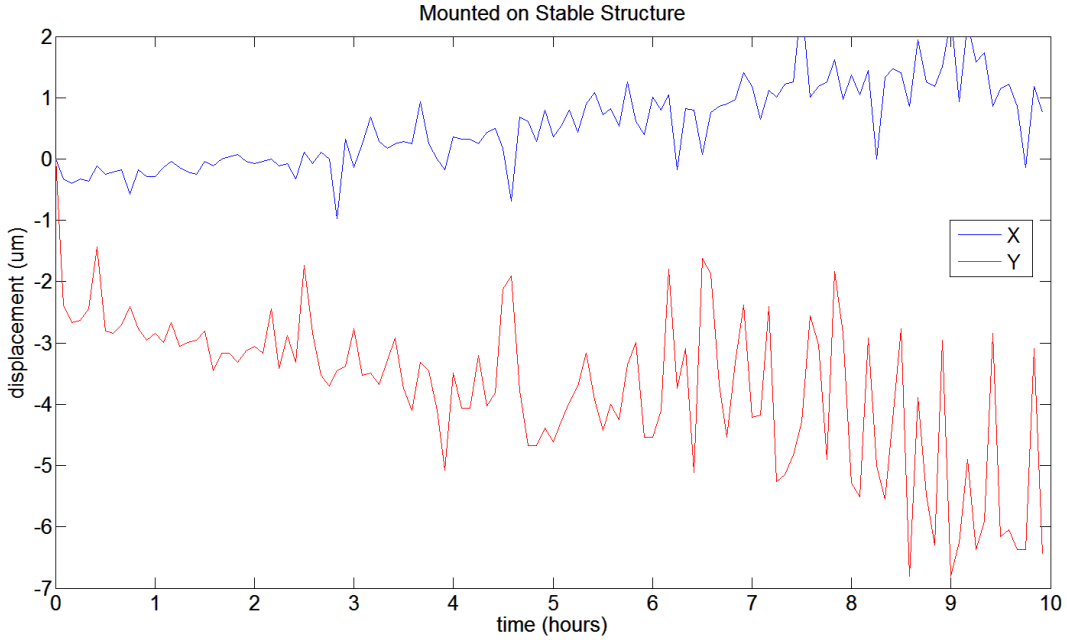

Figure 2.28 Stability test (imager is mounted on stable structure).

2.7 Diffraction pattern formation

NORIS [1] was implemented using the 780 nm diode laser (U-L-M Photonics ULM780-01-TN-S46FOP), and was locked to the D2 line of Rb vapor cell held at 85ºC (Figure 2.1). The stabilized laser was incident on a SixNy/Au grating which was temperature stabilized to 45ºC using a PID loop controller. To form the grating, a silicon wafer coated with silicon nitride is microfabricated with an aperture array of a reflective thin film. The thin film pattern acts as a diffractive element, creating an optical pattern in space which is used as a nano-precise optical ruler. The pattern formed at the AFM stage is a two dimensional diffraction pattern consisting of low and intense spots (Figure 2.29). The piezoresistive scanning probe is attached to an imaging camera. The camera captures an image of the optical ruler, then uses that information to calculate its position using sub-pixel digital image processing techniques.

2.8 Vibrational noise isolation

In order to make NORIS amenable to generic AFM system use, we designed a base that holds the entire AFM system, incorporated within a frame supported by four beams on edges to hold the NORIS optical subsystem above the AFM system (Figure 2.30).

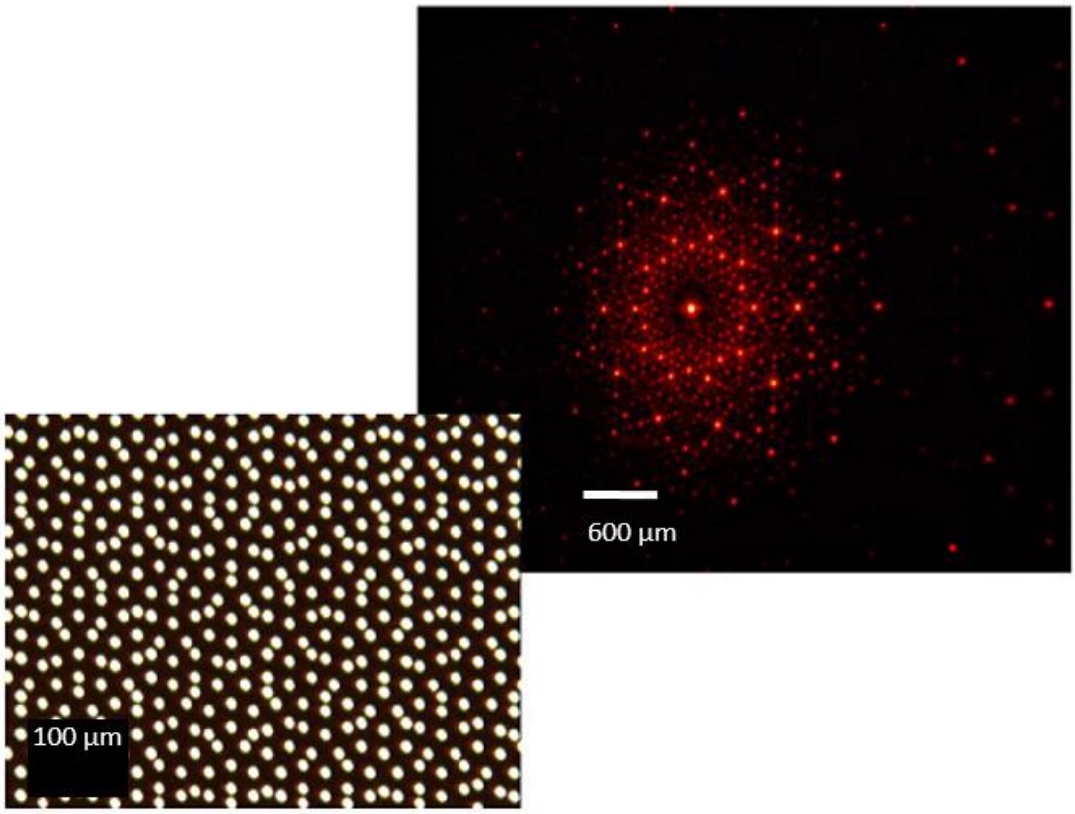

Figure 2.29 Optical diffraction ruler made by fabricating a photomask with the desired aperture pattern. The micrograph on the left shows a back-illuminated photomask of an aperture pattern. Image on the right shows resulting diffraction pattern taken by OV7670 imager.

A unique combination of metal and elastomeric interfaces is used to reduce mechanical coupling from the base. The intention of this structural design was to reduce the vibration motion inside NORIS. Our experimental results demonstrated to us that the existing NORIS system is prone to more than a few elements of noise that might result in vibration. All the laser components were situated on an optical table that does not provide sufficient isolation to the NORIS system. A base platform was

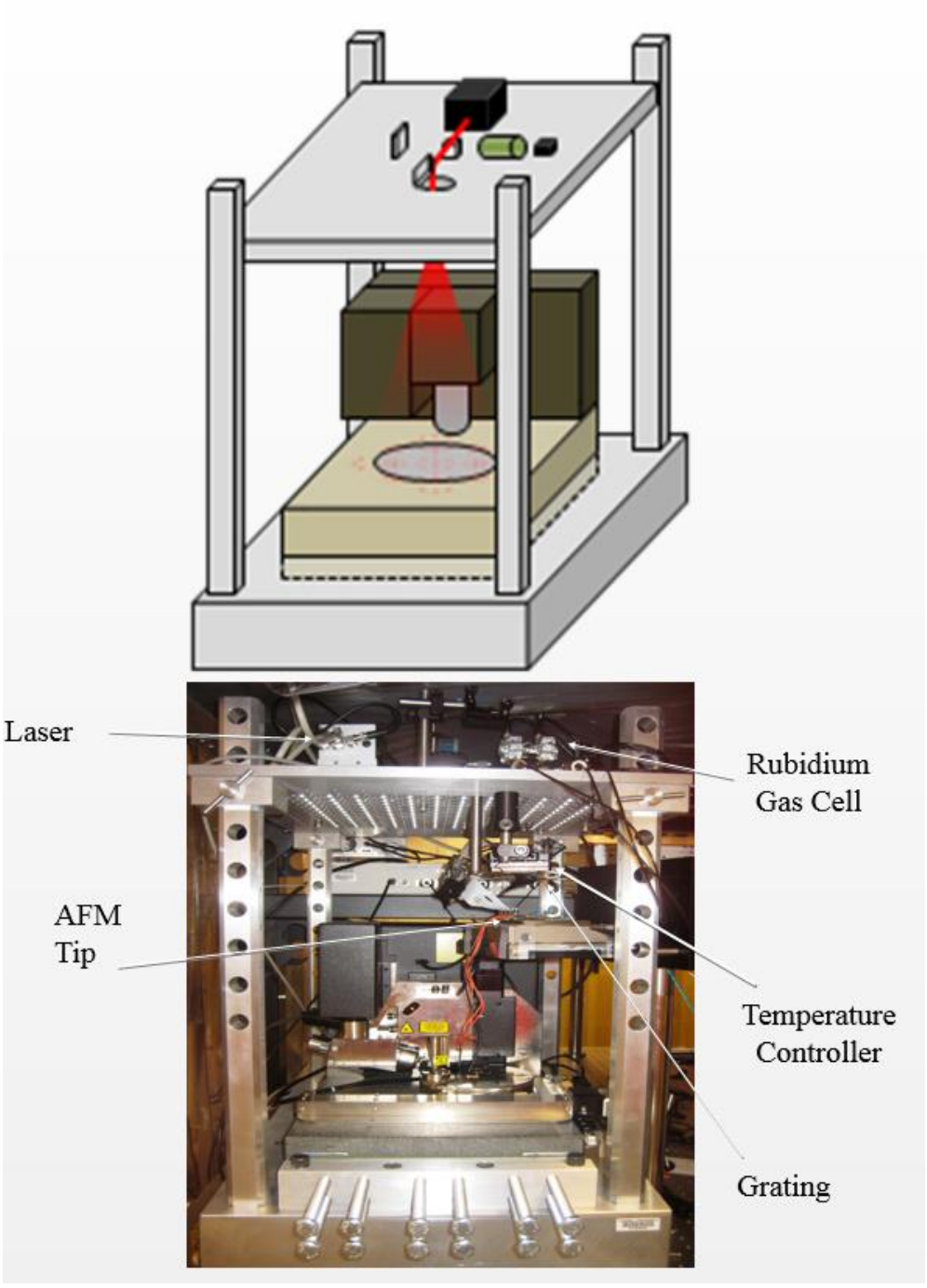

Figure 2.30 Schematic (top) and real picture (bottom) of the New Base for VEECO AFM which incorporates NORIS.

created from 6061 aluminum alloy which has superior vibration damping qualities among aluminum family and the inherent light weight advantage of aluminum alloys. To reduce the vibrations in the axial direction, we created actuation elements that one can use to constraint the AFM. Moreover, one has the capability to adjust the acoustic characteristic of this structure by moving the actuation element in the axial direction for the base platform. The actuation elements consist of 12 bolts in a parallel arrangement which provides the user with a flexibility to modify the damping properties between the base platform and the AFM.

2.9 Piezoresistive AFM cantilever fabrication

Figure 2.31 shows the AFM tip made using a process flow adapted from a previous force probe design [16]. First, a 1µm low pressure chemical vapor deposition (LPCVD) low stress silicon nitride layer was deposited on 4-inch silicon wafers as electrical insulation and wet-etch mask layer. Then a 1µm LPCVD poly silicon is deposited as piezoresistive material. A 0.5µm PECVD silicon oxide insulation layer was deposited on top of the poly layer. A Pt/Cr ground layer was evaporated and patterned to cover the poly traces of all piezoresistor except at the bonding pads. A deep reactive ion etching (DRIE) step on the front side of the wafer was done to define the shape and depth of the two microprobes at the tip of the AFM probes. Finally, a backside-only KOH etching produced the piezoresistive AFM. Piezoresistors were

designed to have the minimum total vibrational noise which is obtained when the piezoresistor length is 2/3 of cantilever length [3].

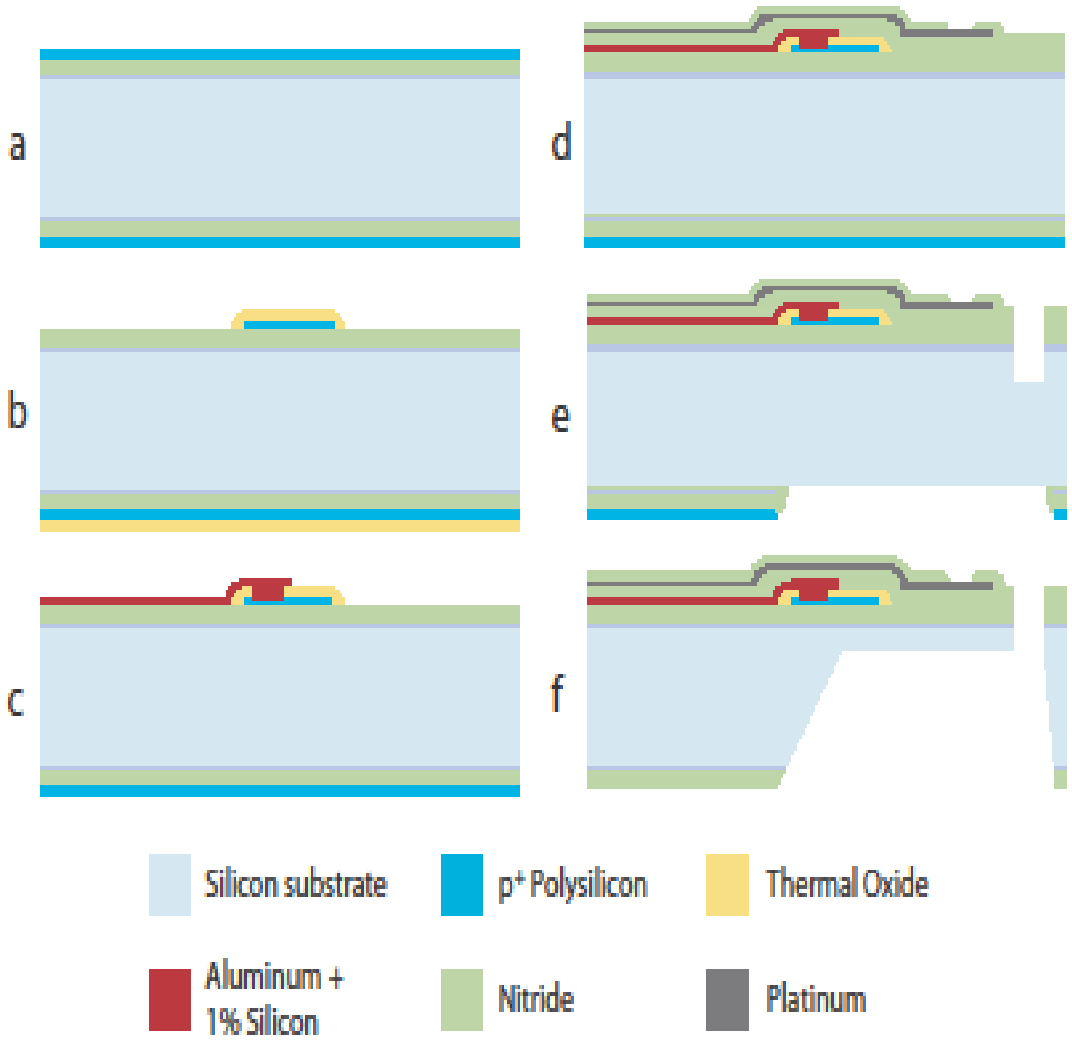

Figure 2.31 Process flow for fabrication of the piezoresistive AFM cantilever.

2.10 Results and discussion

Figure 2.32 shows the Z displacement measurement at NORIS before and after installation of new base. This measurement is done by monitoring the Z output of a NPXY100Z10A nPoint XYZ nanopositioning system over the time while hitting a

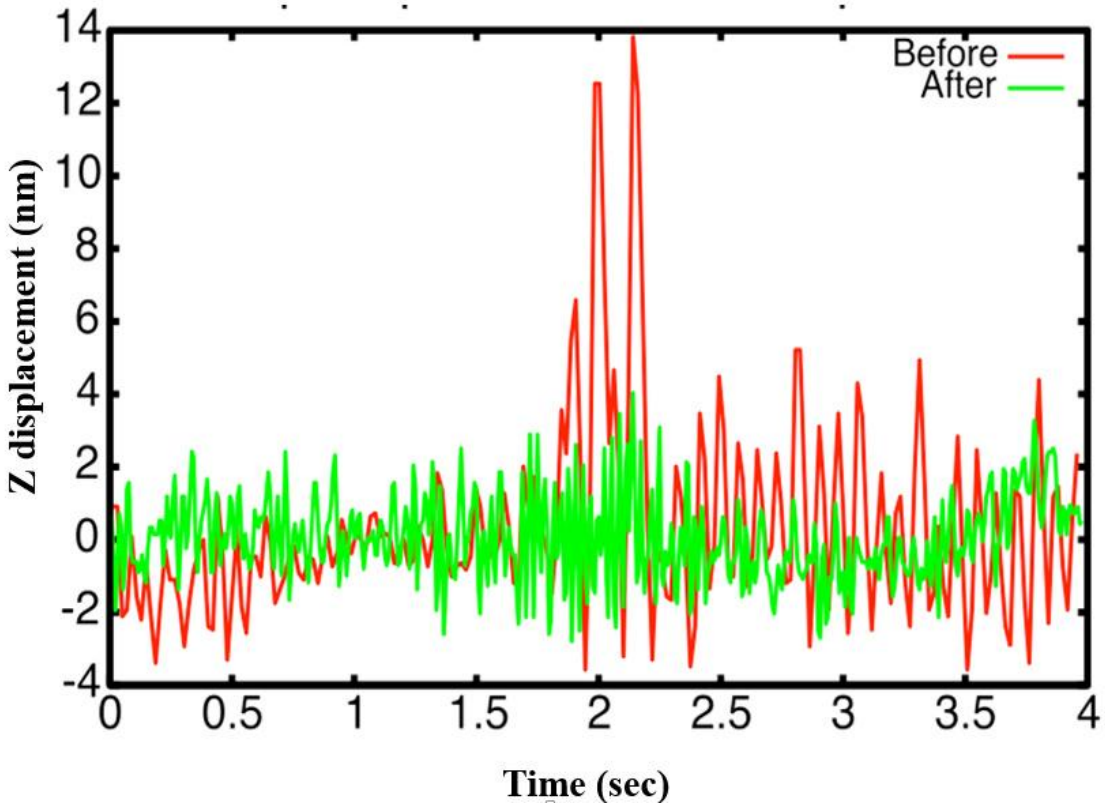

Figure 2.32 Z displacement curve before and after implementation of the new NORIS base.

hammer on the wall close to the whole system every 5 second. As it is evident in this figure, we managed to reduce the vibrations substantially. Standard deviation of Z displacement before and after base installation are 2.7nm and 1.3nm respectively.

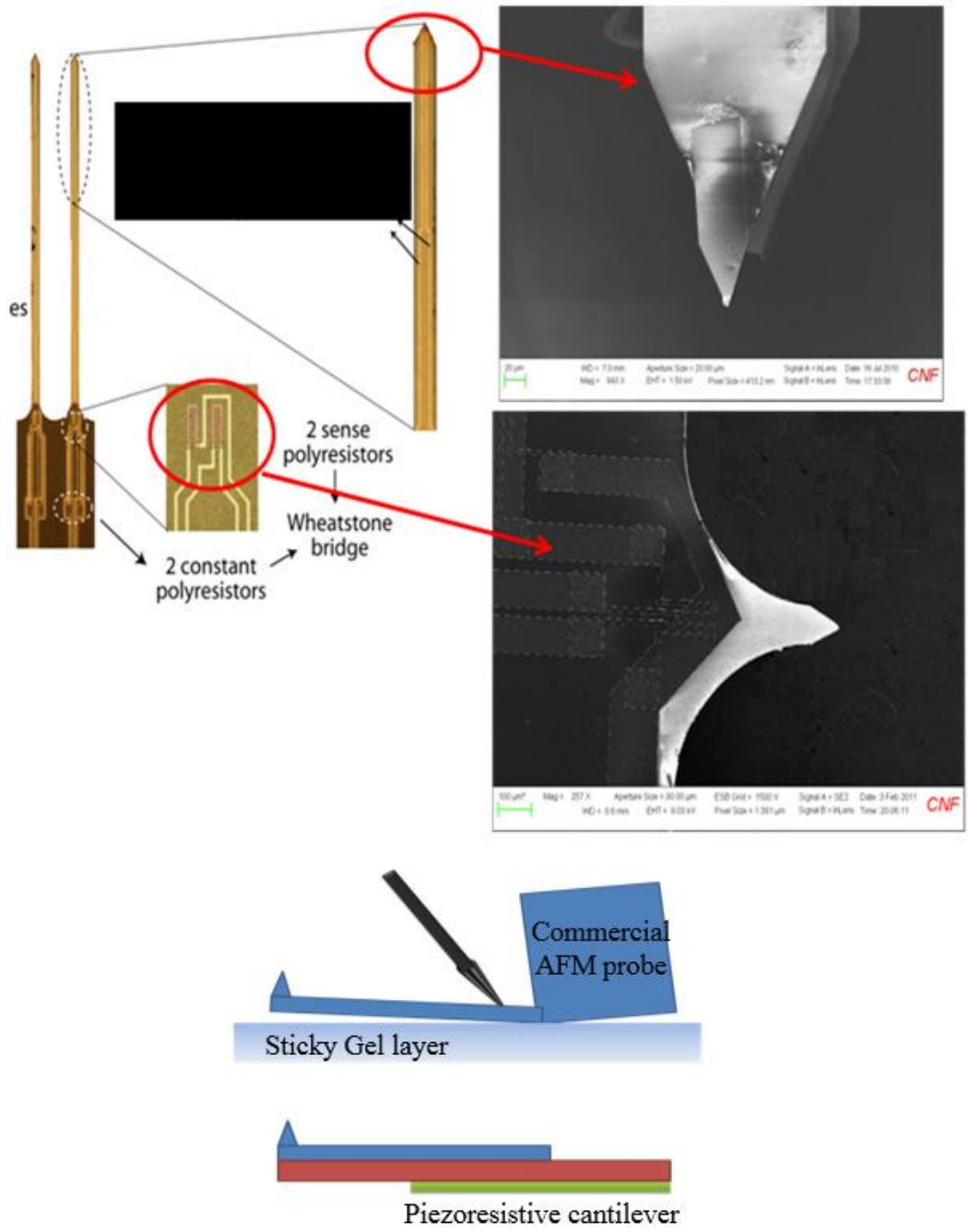

Figure 2.33 Schematic and SEM image of bonding the fabricated piezoresistive cantilevers to the commercial AFM tips (top) and schematic of commercial tip placement on fabricated piezoresistive cantilever (bottom).

By placing an imaging sensor on the moving stage, the stage position can be stabilized to long-term stable ruler to a few nm, which is otherwise impossible under regular stage control system. An OV7670 CMOS imager array samples the optical ruler and a feedback loop is used to calculate its position by Fourier transform cross correlation methods. Since introduction of any wire for data transfer adds vibrational noise to the measurement system, the captures images are being transferred to the computation station wirelessly. Transmission of VGA video from CMOS imager is done over TI CC2530 Zigbee chip. A serial interface bridge chip (OV528) converts the parallel data to serial data and compresses the image in JPEG format and sends it directly to CC2530. The CC2530 chip is a low power RF transmitter/ receiver with 250 kbps rate and send the data within the range of 30m from NORIS. A similar chip which has the USB interface (CC2531) then receives the digital image and sends it to the computer.

The probes were designed specifically for AFM operation and commercial AFM tips are bonded onto the probes. The probes, mounted on another imager chip (Figure 2.33) were tracked under the NORIS system. Since both the stage and the tip are tracked with the same optical ruler, the relative spacing of the probes and the substrate can be held to nm-precision over hours. The preliminary surface scanning data is shown in Figure 2.34. Further improvement for stage calibration and resolution improvement is under investigation.

2.11 Conclusions

Two innovations are presented in this chapter – (1) a new mechanical framework, amenable to use for any AFM system, and (2) piezoresistive AFM tips that are sued to demonstrate AFM operation using NORIS. By implementing a new base using 6061 aluminum alloy, which incorporates NORIS, 70% less sensitivity to the external vibrational noise was achieved. To minimize the total vibrational noise, AFM piezoresistors were designed to have the piezoresistor length by cantilever length equal to 2/3. The achieved piezoresistive AFM tips with force sensitivity is 0.625 V/N. A preliminary AFM scan was achieved with the combined NORIS system.

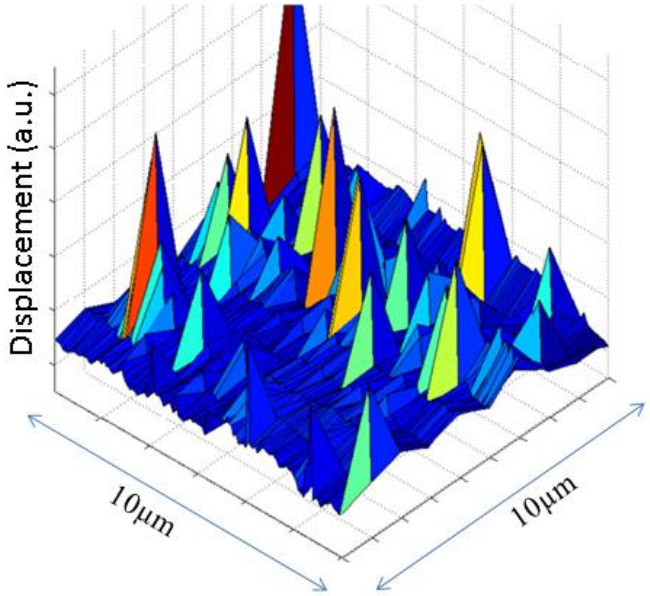

Figure 2.34 Preliminary normalized surface scanning result of a 10μm x 10μm area by this probe. Z displacement is measured by piezoresistive Wheatstone bridge implemented on AFM tip.

CHAPTER 3

ELECTROMECHANICAL PROPERTIES OF GRAPHENE

Graphene and graphite sheets are the two dimensional forms of carbon with sp^2 hybrid bonds [17]. Graphite is a layered material formed by stacks of graphene sheets separated by 0.3 nm and held together by weak van der Waals forces [18]. Graphene, ideally, is a single layer of graphite, a hexagonal structure with each atom forming 3 bonds with each of its nearest neighbors. These are known as the σ bonds oriented towards these neighboring atoms. Graphene monolayer or multilayer films hold the promise for outstanding nanoscale electrical and mechanical properties, owing to their unique monocrystalline structure. The monocrystalline and 2-dimensional structure of graphene is responsible for very fast electron mobility, very high Young's modulus, and negligible internal mechanical hysteresis [19, 20, 21]. Owing to the monolayer nature and the effective confinement of electrons in two-dimensions, any applied strain in graphene films is has the potential to create large changes in conductivity as the electrons are forces to traverse larger potential wells along increased bond-lengths. A recent theoretical work predicts the splitting of the graphene band-gap from conductive to semiconducting state upon applied strain [22]. However, many others have claimed that single-layer graphene cannot have a band-gap [23]. If a band-gap exists, the strain-induced band-gap modulation could be one source of piezoresistivity in graphene. Any practical graphene film often consists of multiple layers of graphene sections with various crystalline grain sizes ranging from a few nm to 100s of microns

[24, 25]. As a graphene film is stressed, the grain boundaries are likely to stretch modulating electron conduction along the boundaries. Surfaces on which graphene is placed can also have effects on graphene operation. The electric fields from the surfaces can also drastically effect conductivity of graphene [20]. This effect has been used to implement graphene field effect transistors [26].

First discovered by Lord Kelvin in 1856 [27], piezoresistivity is the effect of strain on conductivity is the piezoresistivity effect. The term "piezo" is rooted from the term "piezen" from the Greek meaning *to press*. "Piezoelectricity" sounds similar, but with a very different effect, where charge is generated from applied stress. So, the change of resistance is a function of the dimensional change and the resistivity change.

$$\frac{\Delta R}{R} = (1 + 2\nu)\varepsilon + \frac{\Delta \rho}{\rho} \qquad \text{Equation 3-1}$$

where R = resistance, ρ = resistivity, ν = Poisson's ratio and ε = strain.

The former term comes from the dimensional change, and the latter term is the resistivity change. The change of resistance to the applied stress is defined as the gauge factor.

$$GF = \frac{\Delta R/R}{\varepsilon} \qquad \text{Equation 3-2}$$

where GF = gauge factor.

Tight binding theory for ideal graphene monolayers predicts a gauge factor of 2.9 for graphene nano ribbons and piezoresistance measurement via in-situ nanoindentation proves this estimation [28]. Similarly, the gauge factor about 11.4 was obtained at graphene/ epoxy composites cast in mold [29].

Previous efforts have utilized electrodes or probes applied over the graphene films and then apply stress to the solid substrate to realize strain in the graphene films [30]. Table 3-1shows the different structures for piezoresistivity gauge factor measurement in graphene and other carbon-based devices.

Table 3-1 Piezoresitivity measurement structures at different carbon-based devices.

Structure	Schematic/ Snapshot	Ref
Composite/ Polyamide membrane	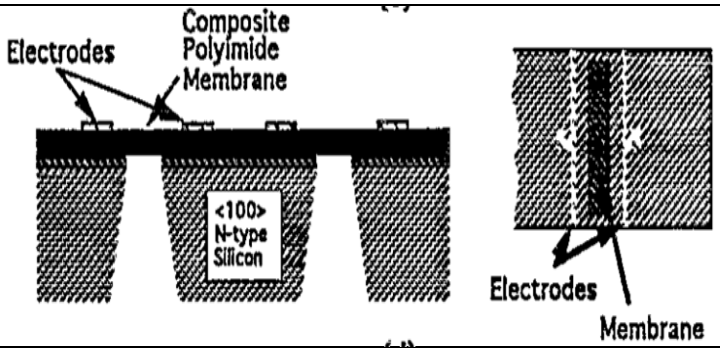	[30]
CNT bundle	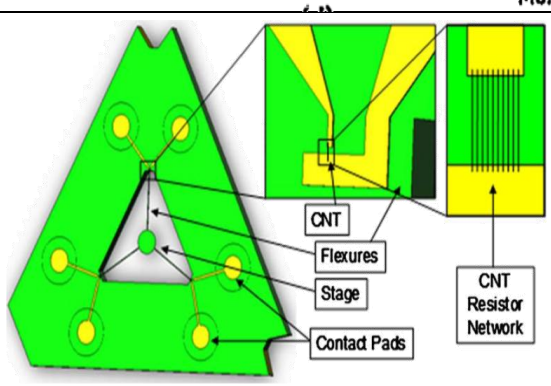	[31]
Graphene with 4-point probe structure on top	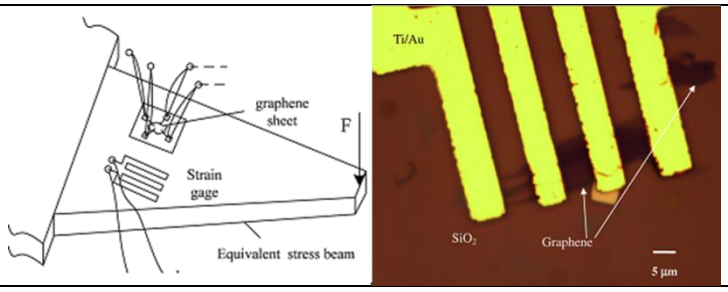	[32]

In this chapter, the device fabrication for piezoresistivity measurement is presented where we place the graphene films over the electrodes defined over lows-stress Si_xN_y membranes using a film transfer method. In this method, the graphene film is poly-crystalline with a grain sizes between 50-800 nm, and can be two or three layers thick. The Si_xN_y/electrode/graphene film stack membranes were actuated using a PZT actuator at resonance to obtain high strains, and the resulting change in resistance was used to measure the gauge factor (Figure 9). Optical interferometer was used to measure the displacement as a result of PZT actuation, and the displacement was used to determine the strain. A very large gauge factor of 17980 was obtained. The membrane was also actuated by DC pressure as demonstrated in Chapter/Section ??.

This large gauge factor is two to three orders of magnitude higher than that of most other materials which would enable piezoresistive transducer SNR to be higher by the same factor, making piezoresistive transducers much more attractive than other transduction mechanisms such as electrostatic or piezoelectric sense transducers. For example, for electrostatic transduction, the high sensitivity often occurs by decreasing gaps, but that often occurs at the cost of dynamic range and linearity. Piezoelectric films often require thicker films to obtain higher charge for a given film thickness, and do not scale well at the nanoscale.

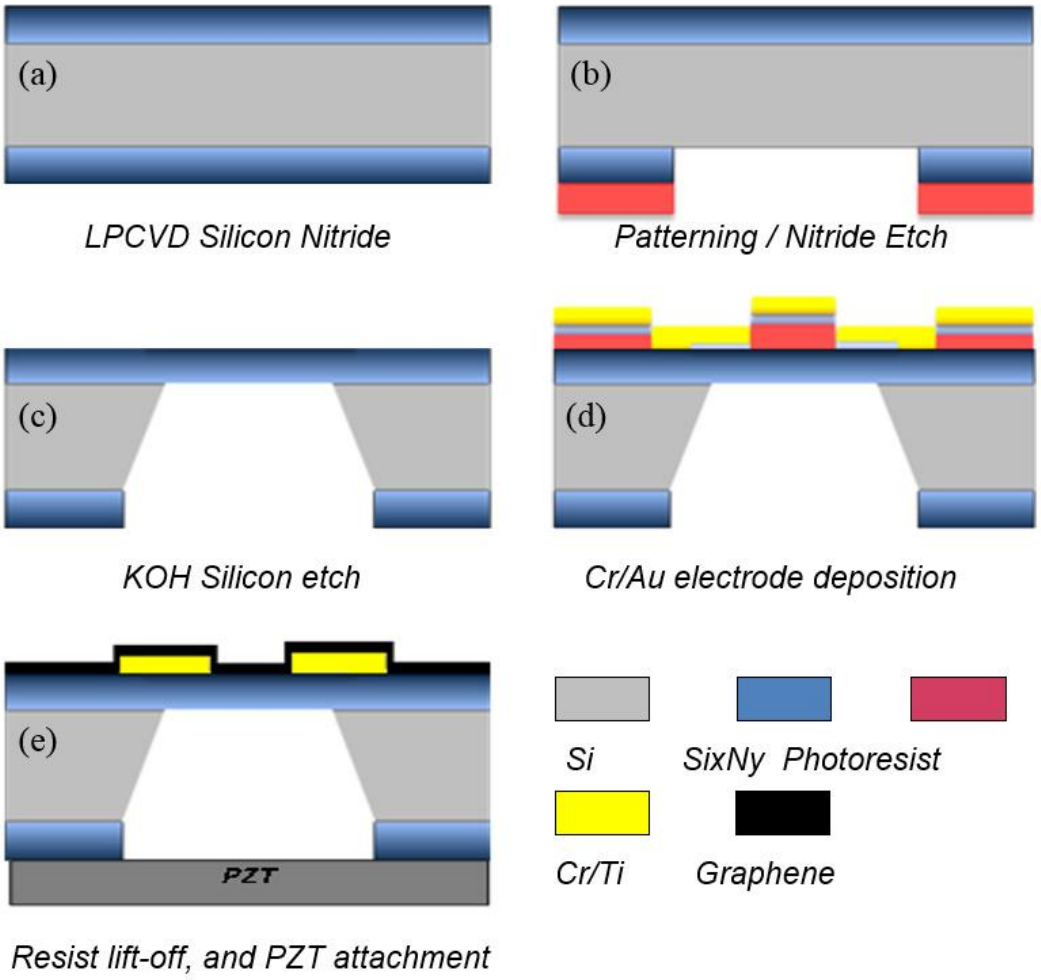

Figure 3.1 Process flow of graphene-based piezoresistive membrane type MEMS strain sensor fabrication. Low stress LPCVD Si_xN_y deposition (a), Patterning the silicon nitride film and wet etching of the silicon substrate using KOH solution (b), Patterning SPR220.3.0 photoresist (c), Cr/Au e-beam evaporation and lift-off (d), Transferring graphene on top of the structure (e), Cleaning and drying the sample (f), and PZT attachment for ac actuation (g).

3.1 Device fabrication

A low-stress silicon-nitride membrane of 430 nm thickness is fabricated over a 4-inch silicon substrate using LPCVD deposition and anisotropic etching of the silicon substrate (Figure 3.1). The Si_xN_y membrane is then coated with a stack of Cr (5nm)/Ti (20nm) using thermal evaporation. The metal layer is then etched to form a four-point-probe structure (Figure 2-a).

This structure consists of progressively thinner wires converging from gaps of 10um to 1um. A 0.5um thick film of SiO_2 is then deposited in PECVD furnace at 400C and lithographically defined over the end of the electrodes so only the end part of the electrodes are exposed. A graphene layer, prepared using CVD deposition on top of copper foil [33], is transferred on top of the electrodes. The process of graphene transfer requires spinning a thin (300nm) PMMA on top of graphene followed by wet etching of the copper foil. The silicon wafer which includes the nitride membranes is used to lift the PMMA/graphene bilayer floating on top of the Cu etch beaker. Acetone is used to dissolve the PMMA, samples are then cleaned with DI water, and let to dry in room temperature for 6 hours. A PZT plate is adhesively attached to the back-side of the silicon die, with two wires soldered to the PZT plate on the edges.

The Raman spectrum (Figure 3.4) of the graphene films indicates a good quality film owing to the large ratio of G-to-D ratio. The D map is associated with defects in graphene [33]. The G-band is the only band coming from a normal first order Raman scattering process in graphene. However, this two-phonon band is allowed in the second-order Raman spectra of graphene without any kind of disorder or defects [34].

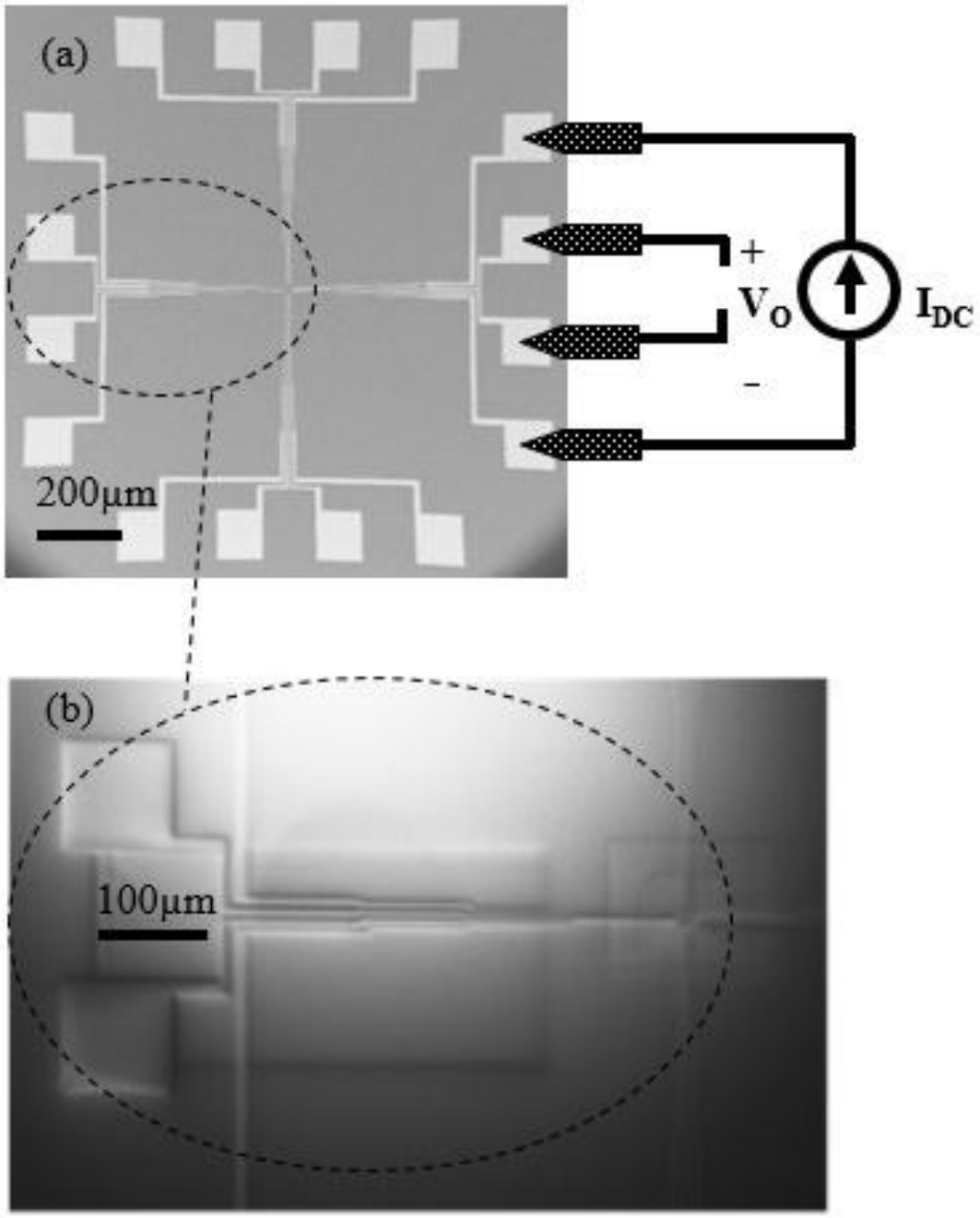

Figure 3.2 SEM image of 4-point probe electrodes on a silicon nitride membrane to measure piezoresistivity of graphene layer placed in the oxide box (a) and magnified version of this image (b)

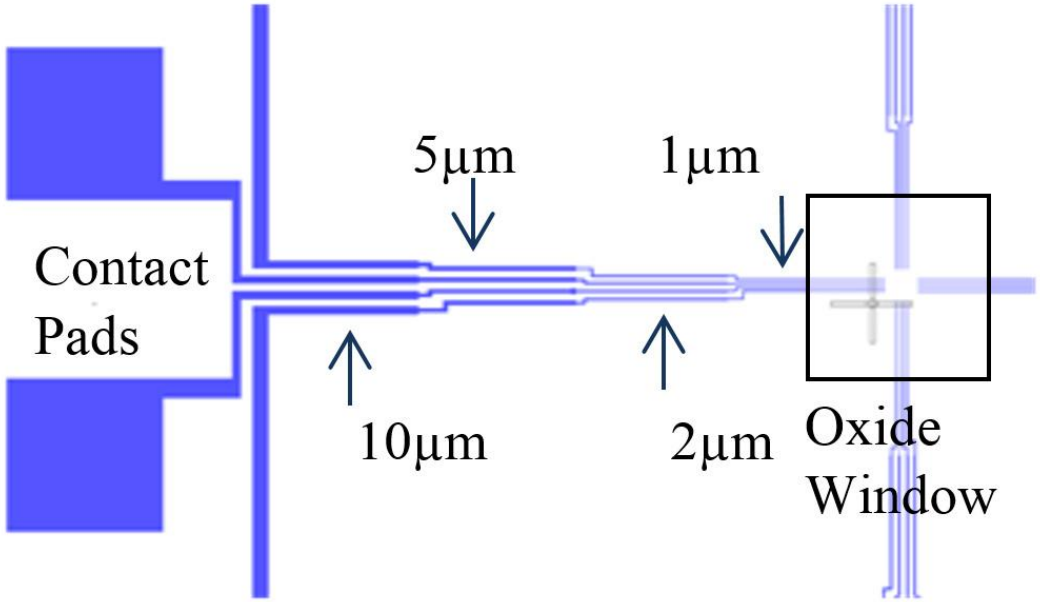

Figure 3.3 Schematic of 4-point probe electrodes on a silicon nitride membrane to measure piezoresistivity of graphene layer placed in the oxide box.

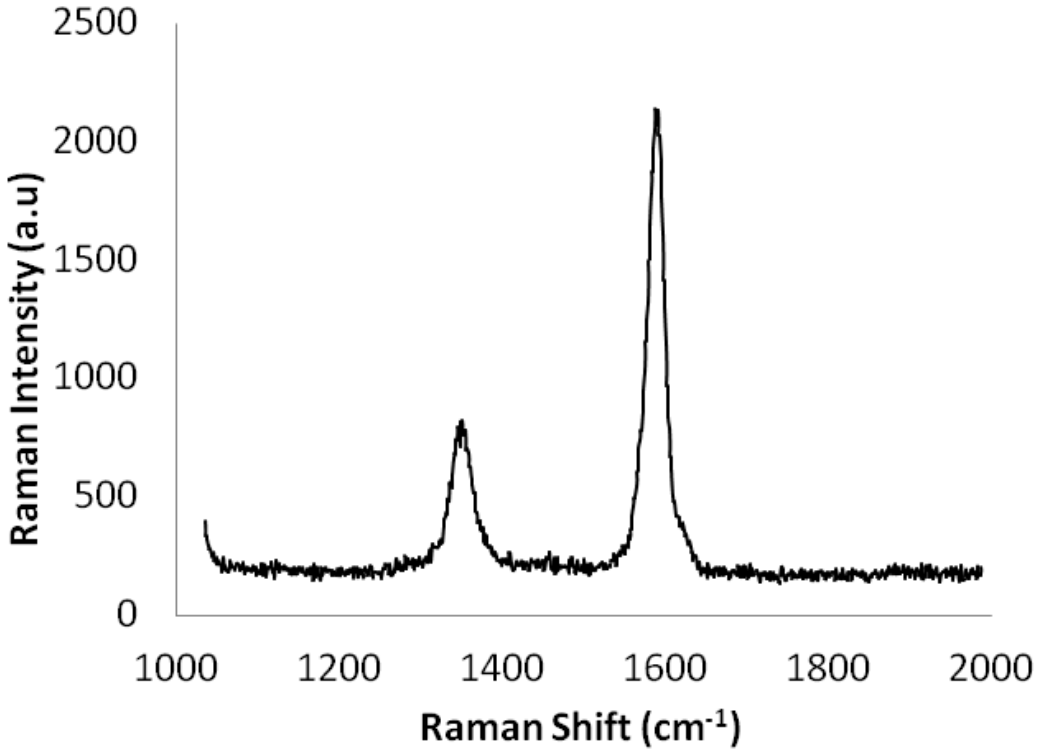

Figure 3.4 The Raman spectra of the transferred graphene film on top of the electrodes.

3.2 Piezoresistivity measurements

The Si_xN_y membrane with graphene was strained using both a constant pressure source and an AC strain using the PZT actuator.

DC strain application: Changes in the graphene resistance are monitored first under steady state strain. Constant strain in the membrane is applied by attaching a syringe vacuum pump to the backside of the cavity (Figure 4). As the syringe plunger is drawn away from the cavity, a local negative vacuum is applied in the cavity. This vacuum pulls the Si_xN_y membrane inwards inducing a compressive strain on graphene. Figure 3.6 plots the output voltage across the inner electrodes as a function of the applied DC current from the outer two electrodes, measuring the resistance of the graphene film between the two inner electrodes. The resistivity increases by 14%, a proof of piezoresistivity in the structure, with a decrease of pressure from 0 to -2.5mmHg. With the DC measurement, it was not possible to measure the strain being generated as the actual DC displacement of the membrane was not easy to measure with the equipment available in the lab. Hence, in order to quantify the gauge-factor, we measured AC strain generation.

AC strain application: We applied harmonic strain on the membrane by driving the membrane at its resonant mode using a piezoelectric PZT actuator bonded to the silicon substrate. The measurement of the vibration displacements of the membrane under PZT actuation was conducted both in vacuum and air. Quality factor of 102 was obtained in vacuum and 80.2 in air indicating that this resonance was heavily damped by anchor losses.

Figure 3.7 shows the block diagram of our measurement setup. The drive voltage on the PZT is phase-locked to displacement measured using an OFV 511 Polytec^{TM} interferometer. A Keithley-2400 is used as current source to bias the outer electrodes of the four-point probe. The voltage across the inner two electrodes, which can designated as the output voltage of the sensor, is amplified with an amplifier gain of 5. The amplifier was a SRS560 pre-amplifier with the bandwidth of 1MHz and input noise level of 4nV/√Hz.

Due to the resistivity effect in graphene/silicon-nitride hybrid stack, the output voltage, shown in Figure 2.1 is as following:

$$V_{PZT} = V_{PP1}\cos(\omega t) \rightarrow V_{O1} = V_0 + v_1\cos(\omega t) \qquad \text{Equation 3-3}$$

A second lock-in amplifier mixes this resistivity output with the actuation signal to make a narrow-band measurement of the output voltages. So, the output voltage of lock-in amplifier before feeding into the low-pass filter is:

$$\xrightarrow{\times V_S\cos(\omega t)} V_{O1}\,V_S\cos(\omega t) \qquad \text{Equation 3-4}$$

$$= \frac{1}{2}V_S v_1 + V_0 V_S\cos(\omega t) + \frac{1}{2}v_1 V_S\cos(2\omega t) \qquad \text{Equation 3-5}$$

where V_S is the amplitude of the built-in voltage source in lock-in amplifier. By passing the signal through the low-pass filter, the narrow-band voltage output becomes:

$$\xrightarrow{LPF} V_{amp1} = \frac{1}{2}V_S v_1 \qquad \text{Equation 3-6}$$

V_{amp} is in fact proportional to the change in graphene resistivity as following:

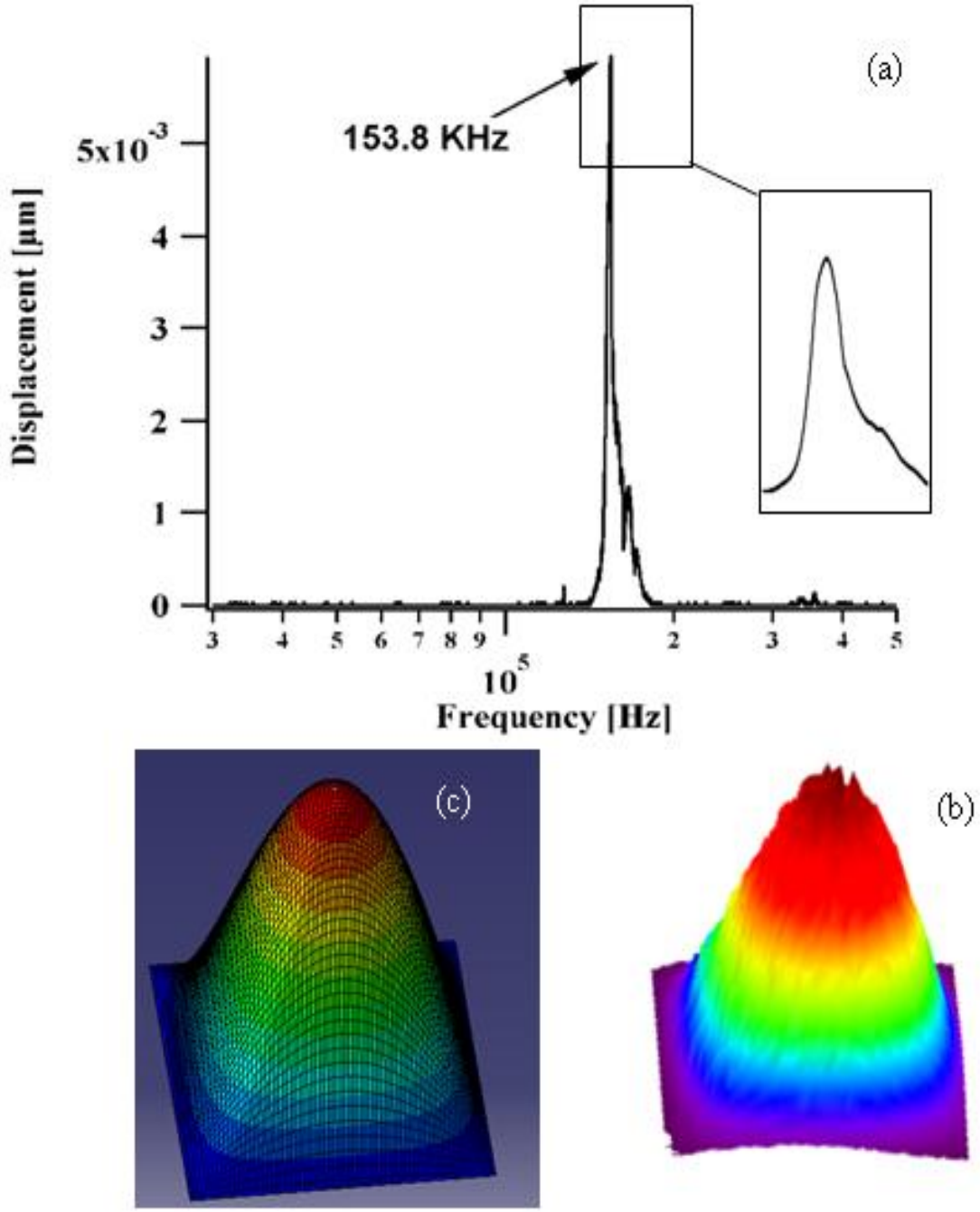

Figure 3.5 Displacement as a function of frequency at the center of the membrane where the piezoresistivity piezoresistivity measuring 4-point probe is placed (a). The first resonant frequency is at 153.8KHz with a quality factor of 80.2 in air. Peak-to-peak voltage for the PZT actuation is 100mV. The measured (b) and simulated (c) mode shape of this membrane.

$$V_{O1} = V_0 + v_1 \cos(\omega t) \xrightarrow{\div I_0} R_{O1} = R_0 + r_1 \cos(\omega t) \quad \text{Equation 3-7}$$

$$\rightarrow \frac{\Delta R}{R} = \frac{r}{R_0} = \frac{v_1}{V_0} = \frac{2}{V_S . V_0} V_{amp1} \quad \text{Equation 3-8}$$

In order to quantify the strain, the vibrational modes of the silicon/PZT composite plate structure were excited by the bonded PZT plate. The silicon-dioxide window, (Figure 2-c) where the resistivity measurement is made, is placed at the center of the membrane, which has the highest value of applied strain at the first breathing resonant mode of the square membrane.

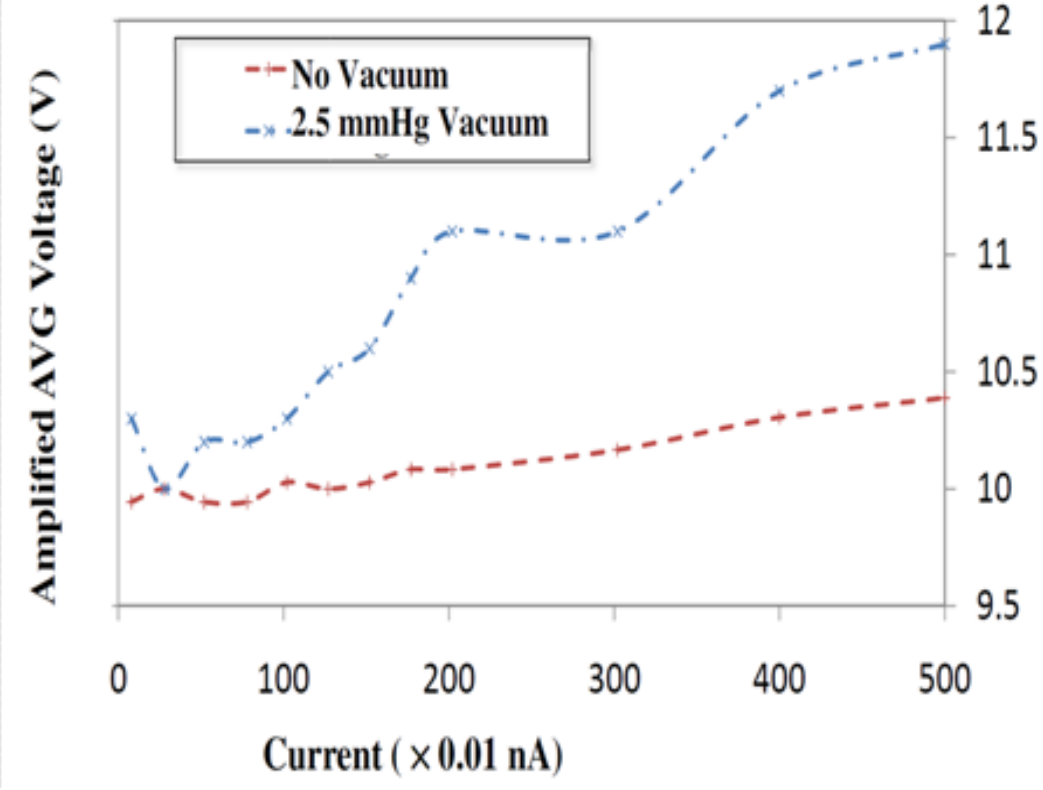

Figure 3.6 Resistivity changes with applied strain through a vacuum suction at different bias currents.

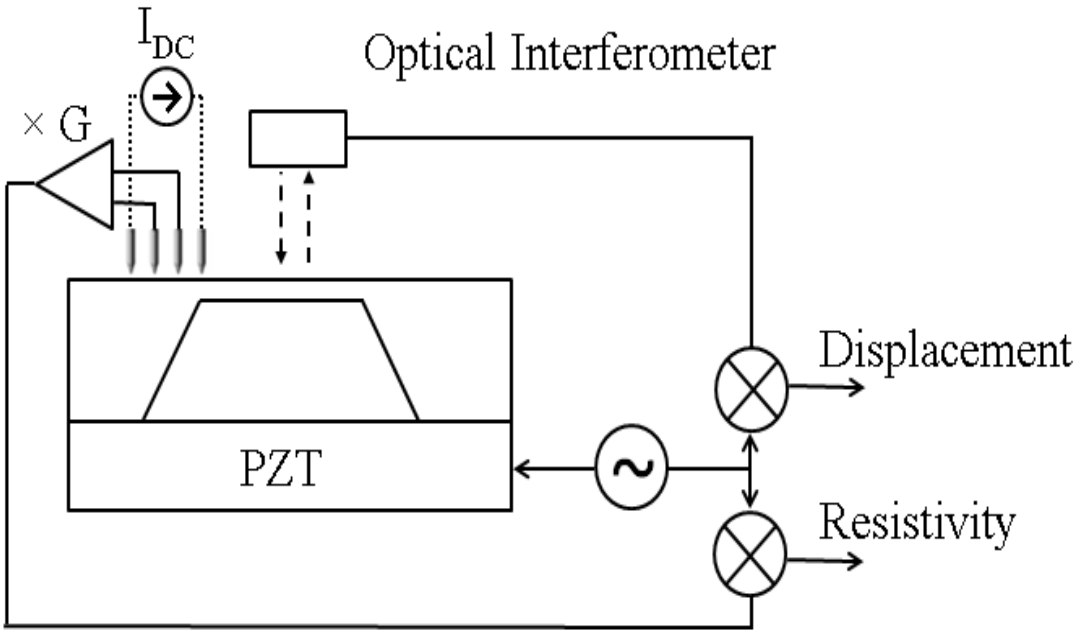

Figure 3.7 The block diagram of the setup in order to measure displacement at the nitride membrane and the resistivity of the graphene film.

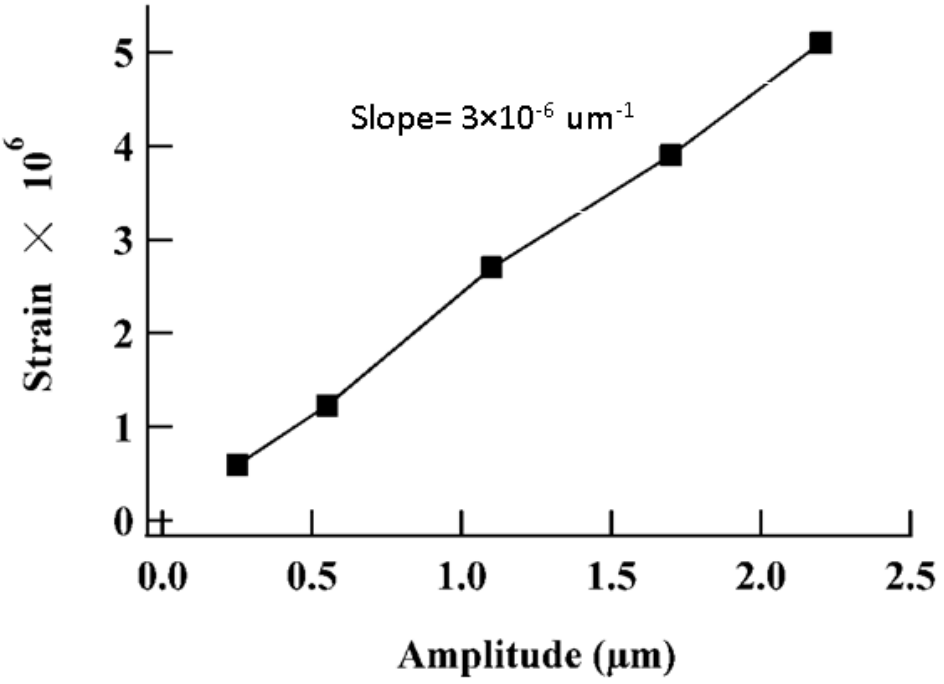

Figure 3.8 Simulated strain values at different amplitudes shows expected linear relationship.

The frequency behavior of the displacement at the center of the membrane is shown in Figure 3.5. Figure 3.5b shows the measured displacement profile of the membrane. As one can see in this picture, the first resonant frequency for the 0.75mm×0.75mm size membrane is at 153.8 KHz, close to the simulation prediction. Simulations are performed using finite element package ABAQUS for the entire PZT/silicon/Si_xN_y membrane structure. Plane strain analysis is used here due to relatively large depth of the structure, compared to its thickness, which gives good agreement with preliminary 3D simulations of the same. The mode shape was obtained with assumed in-plane stress in the nitride membrane. A stress of 220MPa gives good agreement with the experiments and is within the expected range of stress obtained during fabrication.

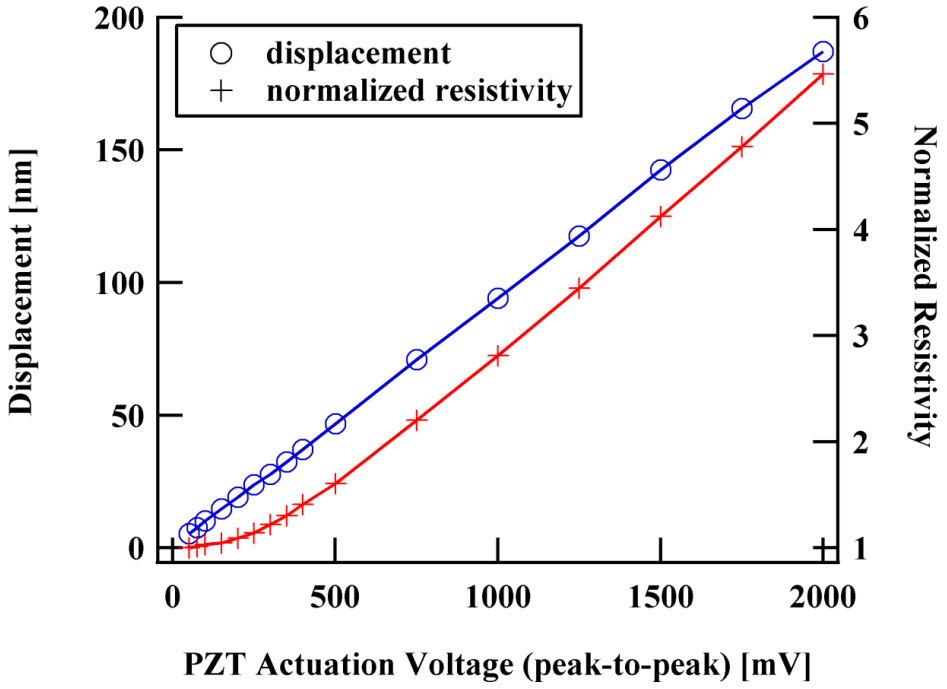

Figure 3.9 Blue curve is normalized resistivity (resistivity divided by maximum resistivity) as a function of drive amplitude. Red shows displacement at electrode location as a function of drive voltage, from which strain can be calculated.

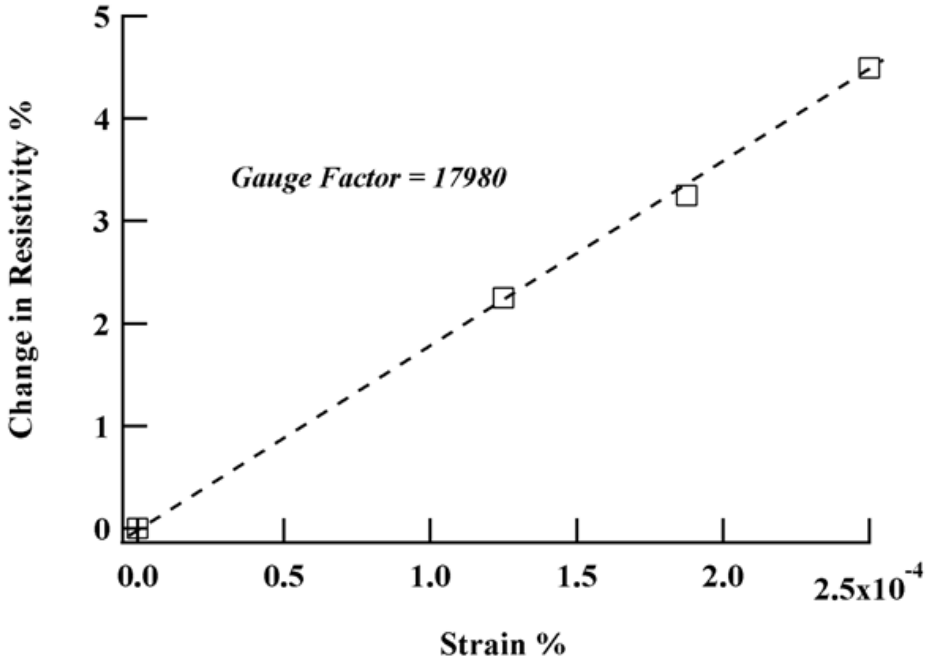

Figure 3.10 Normalized resistivity change versus applied AC strain at 153.8 kHz membrane resonance.

Steady state dynamic simulations were used to obtain resonance response of the structure. While nonlinear geometric effects are considered in the simulations, the PZT is modeled with a ABAQUS built-in linear model . The experimentally measured value of the quality factor is 80.2 (Figure 3.5a), and is used in the simulations. The ABAQUS calculated displacement is in the order of 10nm at resonance for a harmonic excitation of 1V across PZT at the first resonance frequency. Corresponding strain values along the axis are in the order of 10^{-6}. An expected linear dependence is obtained between the peak strain and amplitude of vibration (Figure 3.8). At the same time, the resistivity of the film can be measured as a function of applied PZT voltage (Figure 3.9). The PZT drive voltage was increased from $100mV_{pp}$ to $10V_{pp}$. The minimum limit of $50mV_{pp}$ was imposed by the function generator HP-33120A. With this minimum drive voltage, the smallest AC strain that

could be applied was1.25×10^{-6} %. Hence, our method is limited to measuring the gauge factors for strain range from1.25×10^{-6} % to 2.5×10^{-4} %. The RF coupling from the PZT drive to the four point probe was not responsible for the measurement of voltage across the 4-point probe, as the voltage across the inner electrodes also went to zero if the drive current was reduced to zero. In order to calculate the gauge factor, the voltage between two inner electrodes is measured while actuating the PZT at resonant mode of the membrane with different amplitudes. Corresponding strain at each point is estimated using the linear relationship we came up using ABAQUS simulations (Figure 3.8). If the measured relative resistance is plotted against the estimated strain, the slope of the line is the gauge-factor (Figure 3.10). The measured graphene gauge factor is orders of magnitude higher than that of most piezoresistive materials used in MEMS such as doped polysilicon and metals. Doped polysilicon can have gauge factors on the order of 30-40, while metals have a gauge factor of 55 [35, 36].

3.3 Conclusions

We have developed a process flow to place graphene on-top-of a 4-point resistivity measuring probes, and demonstrated high quality graphene. The piezoresistivity is measured both with DC and AC applied strain, with cyclic strain being measured by exciting the first breathing mode of the membrane. A very high value of the piezoresistive gauge factor for graphene has been measured, in a device suitable for MEMS sensors. The high value of the piezoresistive gauge factor paves way for nanoscale sensitive transducers.

CHAPTER 4

GRAPHENE-BASED PRESSURE TRANSDUCERS

Piezoresistive pressure sensors are very common devices used in biomedical to industrial monitoring applications. The gauge-factor of the piezoresistive resistors, which usually are placed in a Wheatstone bridge configuration, limits the sensitivity of a given sensor. The gauge-factor, the membrane thickness, and the required sensitivity for a given application determine the pressure sensor membrane length and width. A much higher gauge-factor and transducer sensitivity would enable a much smaller sensor for constant sensitivity, or would enable a much more sensitive sensor for constant membrane area (Figure 4.1). Calculations in this figure are based on the equation (1) [37].

$$\frac{\Delta V/V}{q} = G\frac{3}{8}\frac{(1-\nu^2)}{\varepsilon}\left(\frac{a}{h}\right)^2 \qquad \text{Equation 4-1}$$

Given the 0.335 nm thickness of single or multi-layer graphene films, the overall reduction of the sensor is possible by reducing the membrane sizes to 100s of nm. Hence, graphene films may enable nano-scale pressure sensors that are more sensitive than existing polysilicon and silicon piezoresistor technologies, opening the pathways for using pressure sensors within biological cells, or forming high density pressure sensor arrays. Tight binding theory for ideal graphene monolayers predicts a gauge factor of 2.4 for graphene nano ribbons and piezoresistance measurement via in-situ nanoindentation proves this estimation [28].

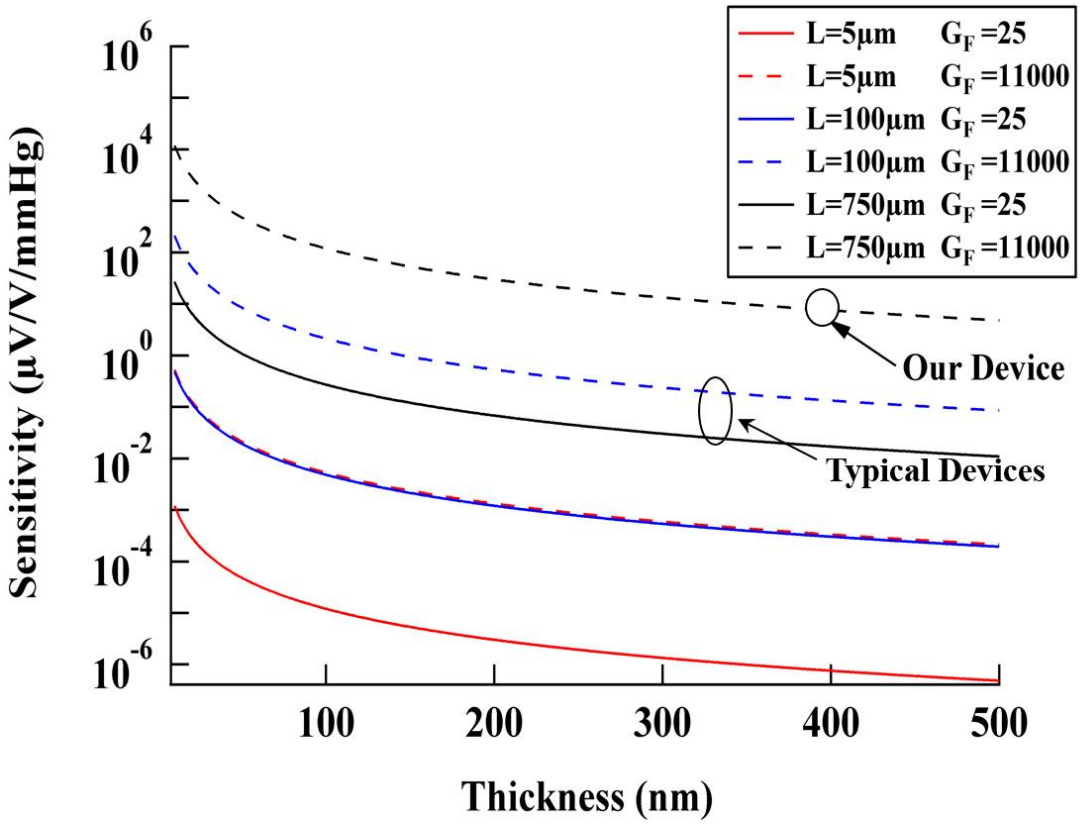

Figure 4.1 Relative sensitivity of strain transducers versus membrane thickness, for different lateral dimensions and gauge factor.

Similarly, the gauge factor about 11 was obtained at graphene/ epoxy composites cast in mold [38]. In Chapter 3, the measurement and report of ultrahigh piezo-resistivity coefficients [39] in graphene/silicon-nitride hybrid composite is studied. In contrast to other reported value for graphene our samples are on silicon nitride films, which may result in charge modulation due to stresses. Another reason for the high value of piezoresistivity could be the grain boundary stretching in graphene films. Practical graphene film often consists of multiple layers of graphene sections with various crystalline grain sizes ranging from a few nm to 100s of microns [24]. As a graphene film is stressed, the grain boundaries are likely to stretch modulating electron conduction along the boundaries.

Previous efforts have utilized electrodes or probes applied over the graphene films and then apply stress to the solid substrate to realize strain in the graphene films [30]. In this chapter, pressure sensor fabrication based on piezoresistive graphene films, transferred over the lows-stress Si_xN_y membranes will be described.

In this method, the graphene film is poly-crystalline with a grain sizes between 50-800 nm, and can be two or three layers thick. The Si_xN_y/electrode/graphene film stack membranes are actuated using a PZT actuator at resonance to obtain high strains, and the resulting change in resistance was used to measure the gauge factor [39]. Optical interferometer is used to measure the displacement as a result of PZT actuation, and the displacement is used to determine the strain. The very large gauge factor of 11289 is measured on this device. This gauge factor is two to three orders of magnitude higher than that of most other materials which would enable piezoresistive transducer SNR to be higher by the same factor, making piezoresistive transducers much more attractive than other transduction mechanisms such as electrostatic or piezoelectric sense transducers. For example, for electrostatic transduction, the high sensitivity often occurs by decreasing gaps, but that often occurs at the cost of dynamic range and linearity. Piezoelectric films often require thicker films to obtain higher charge for a given film thickness, and do not scale well at the nanoscale.

4.1 Device fabrication

The device fabrication is similar to what is described in section 3.1. As shown in Figure 3.1, the device fabrication starts with formation of a 300 nm low-stress LPCVD

silicon-nitride on a 4-inch <100> p-type silicon substrate followed by anisotropic etching of the silicon substrate. A stack of Cr (10nm)/ Ti (20nm) is then evaporated and patterned using thermal evaporation to form a four-point probe structure. This structure consists of four wires on each side of the membrane converging from gaps of 10µm to 1µm. A 0.5µm thick SiO_2 film is sputtered and patterned over the electrodes so only the end section of electrodes are exposed. Graphene layer is transferred, as described in Chapter 3. The sheet resistance of the graphene film is 765- 1500 Ω/□, measured over 10 samples. Finally, a PZT plate is adhesively attached to the back-side of the silicon die, with two wires soldered to the PZT plate.

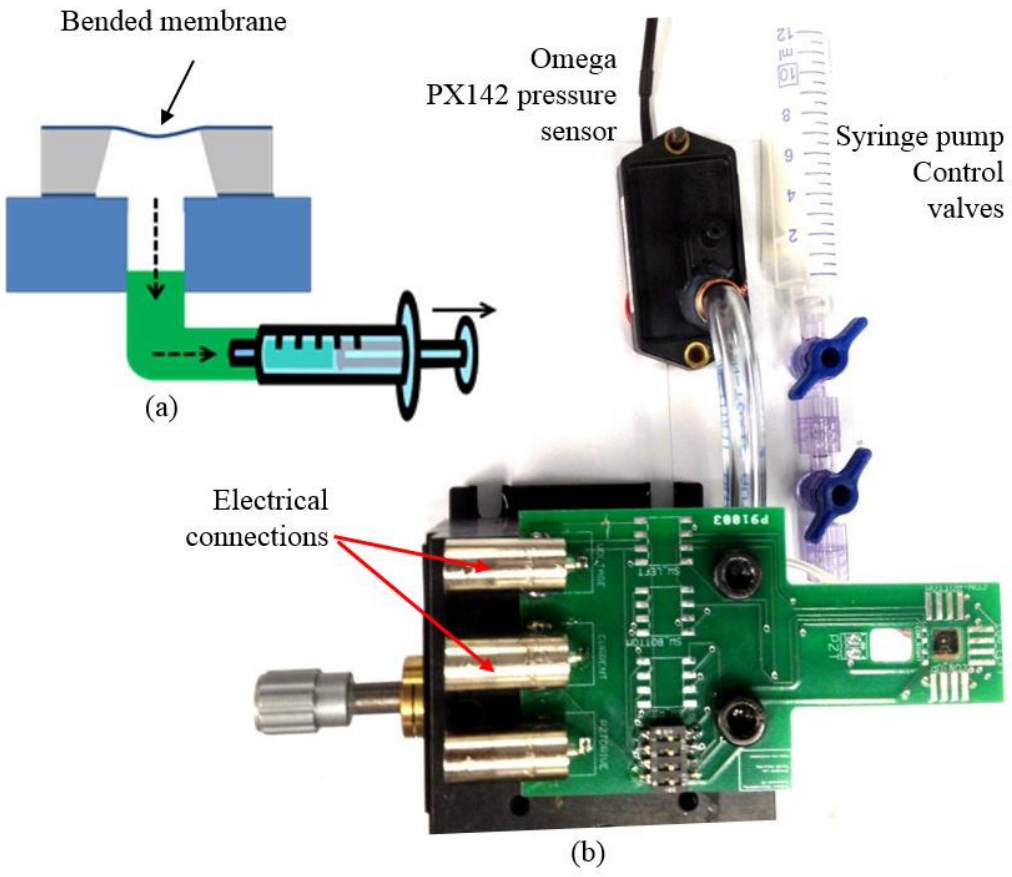

Figure 4.2 Schematic (a) and image (b) of measurement system including syringe pump, strain gauge, and leveling stage, and commercial pressure for calibration.

4.2 Pressure sensitivity Measurements

Measurement system consists of a syringe pump in series with two controlling valves, attached to the backside of the cavity and used to induce constant strain on graphene/SixNy composite plate (Figure 4.2). Pushing and pulling the pump induces tensile and compressive strains on the graphene/nitride film respectively. A printed circuit board (PCB) is designed to hold our device and carry electrical signals for PZT actuation and resistivity measurements. Entire PCB is mounted on a leveling stage with 0.1 degrees precision in order to make the membrane parallel to the Zygo 7300 optical displacement measurement system. Changes in graphene film resistance are monitored under this steady state strain by measuring the output voltage across the inner electrodes as a function of the applied DC current from the outer two electrodes (Figure 4.3).

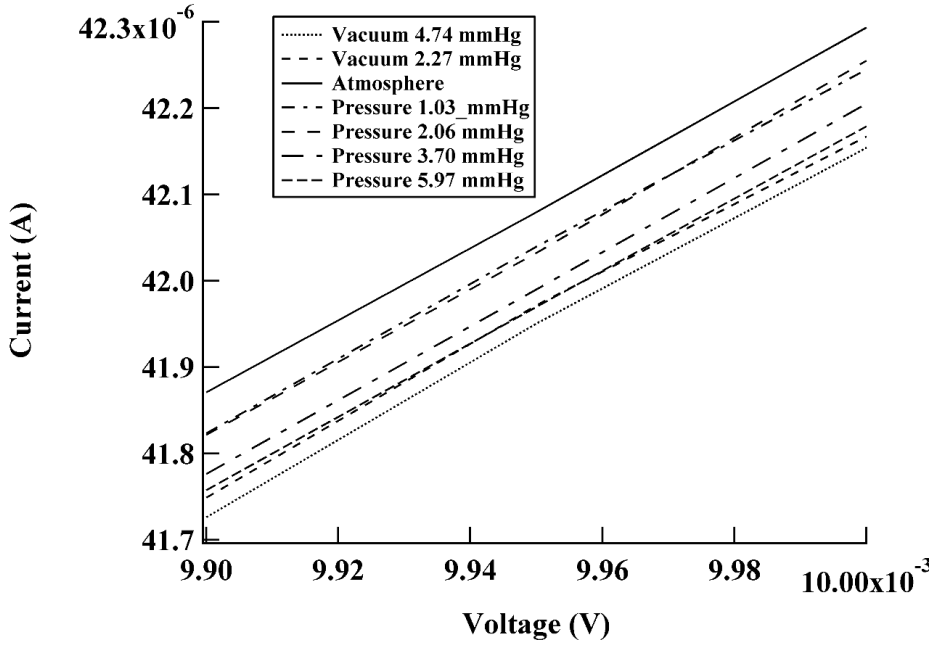

Figure 4.3 I-V curve at different strains around 9.9mA

4.3 Noise measurement at graphene/Si_xN_y strain gauge

In this section, our aim is to study the electrical 1/*f* noise (flicker noise) performance of the pressure induced graphene/silicon-nitride membrane. The flicker noise is called the 1/*f* noise because of its power spectral density, $S(f) \alpha 1/f^{\nu}$ where *f* is frequency, and ν is noise number, often between 1 and 2. Flicker noise has been studied for graphene devices, and two mechanisms have been identified as 1/*f* noise sources:

(1) exchange of charge through trapping-detrapping process and (2)random migration of trapped charges within the substrate or surface adsorbents [40].

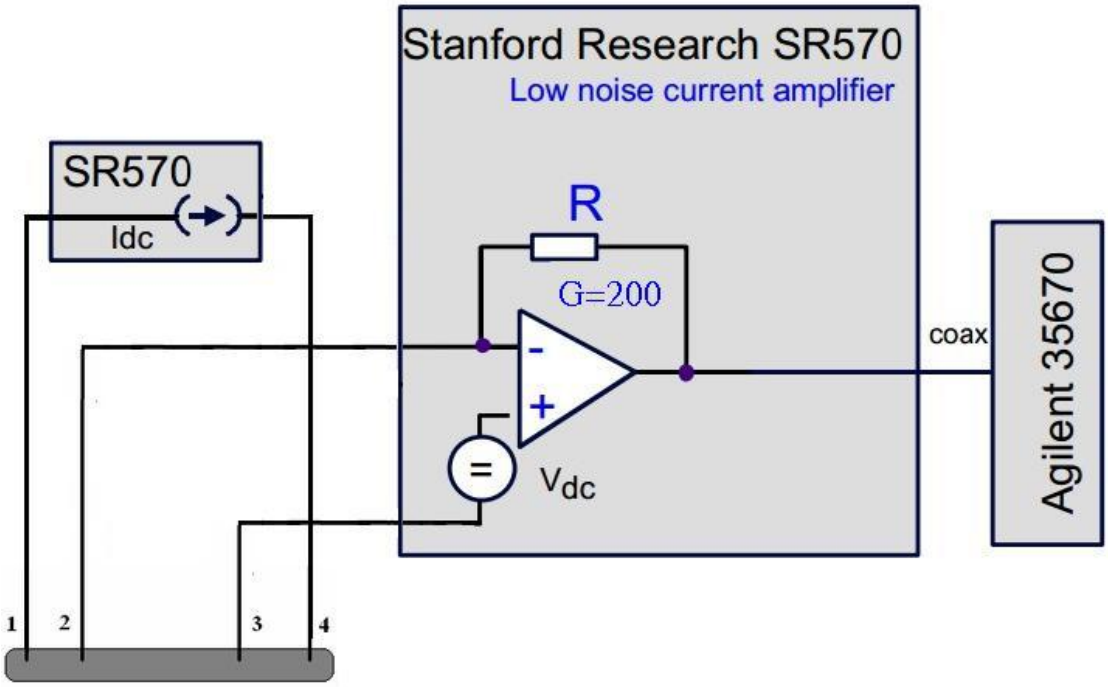

Figure 4.4 1/*f* noise measurement setup for graphene using 4-point brobe structure.

The conductance $1/f$ noise of a graphene resistor can be measured as voltage fluctuations if a constant current is passed through the graphene. The voltage spectral density at this condition is:

$$\frac{S_V}{V^2} = \frac{S_R}{R^2} \qquad \text{Equation 4-2}$$

We use the four-point probe structure (Figure 3.2) to investigate the resistivity and the noise in our graphene/silicon-nitride hybrid membrane. The outer contacts are used as constant current driver contacts and the inner contacts measure the $1/f$ voltage noise spectrum and sheet resistance [41].

From the ratio between the voltage drop over the inner contacts 2,3 and the current at the outer contacts 1,4 (Figure 3.2), the sheet resistance is calculated such as $R_{sh} = (\pi/\ln 2)V_{23}/I_{14}$ [42]. The measured values for different samples vary between 1.5kΩ/□ to 4.0kΩ/□. The$1/f$ voltage noise over the inner contacts S_{V23} is normalized for the current I_{14}, the frequency and area such as

$$C_{us} = (f S_{V_{23}}/V_{23}^2)(\frac{S^2}{1.45}) \qquad \text{Equation 4-3}$$

where *s* is 1μm (the spacing between the probe lines).

The schematic of measurement setup for noise measurement is shown in Figure 4.4. A low noise SR570 is connected to the outer electrodes as constant current drive and differential output is sensed across electrodes 2 and 3 and preamplified with gain of 200 using the second SR570. The output of low noise current pre-amplifier is then feed into Agilent 35670A dynamic signal analyzer.

The normalized $1/f$ noise for our device is shown in Figure 4.7. This curve is useful reference to compare the noise behavior of our graphene-based device with other

devices. The bottom line in Figure 4.5 (I=0uA) shows the background noise and the value 1×10^{-15} V^2/Hz after the knee frequency (~34Hz) matches the expected thermal noise ($4K_BTB$) for graphene resistor where K_B is Boltzmann constant, T is the temperature, and B is the bandwidth (20KHz at our measurement setup).Table 4-1shows the comparison of normalized voltage noise spectra (V^2/Hz) at 100Hz for our device and other graphene devices.

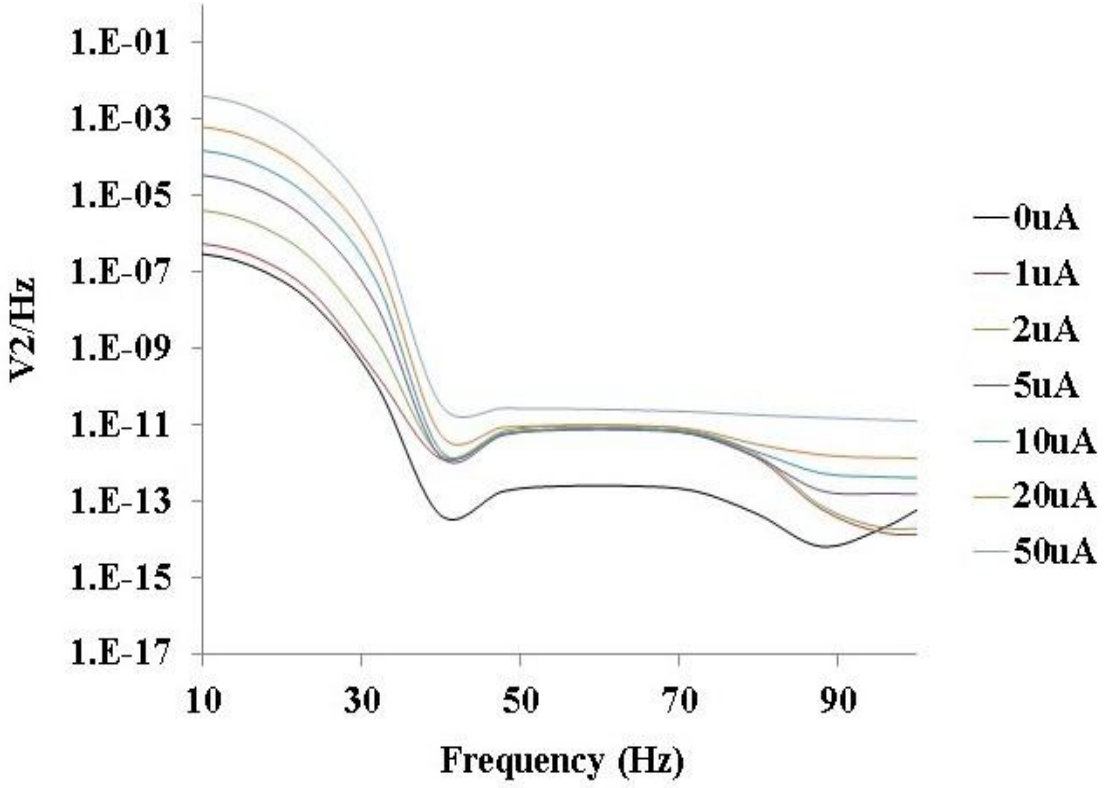

Figure 4.5 1/*f* spectra measured across the inner contacts of the four-point probe, by applying different currents from 1uA to 50uA through the outer electrodes.

Table 4-1 Comparison of normalized 1/*f* spectra at 100Hz for our grahpene/silicon-nitride hybrid membrane and other graphene-based and carbon-based devices.

Device Structure	**S_V/R^2 (1/Hz) at 100Hz**	**V applied**	**Ref.**
Suspended graphene	6×10^{-9}	50-60 mVolts	[43]
Graphene FET	2×10^{-10}		[44]
Single layer graphene	8×10^{-11}		[45]
Graphene FET	6×10^{-13}	5-100V	[46]
Our Device	**10^{-19} - 10^{-15}**	**0.6 – 32 mV**	**This work**
polyaniline/polyurethane	5×10^{-18}		[47]

4.4 Pressure Induced Stress Simulation

Simulations are performed using finite element package ABAQUS for the entire PZT/Silicon/Membrane structure. Plane strain analysis is used here due to the relatively large lateral dimensions of the structure, compared to its thickness, which gives good agreement with preliminary 3D simulations. The mode shape was obtained with assumed in-plane stress in the nitride membrane.

The minimum limit of 50mVpp was imposed by the function generator HP-33120A. With this minimum drive voltage, the smallest AC strain that could be applied was1.25×10^{-6}%. Hence, our method is limited to measuring the gauge factors for strain range from1.25×10^{-6}% to 2.5×10^{-4}%. The RF coupling from the PZT drive to the four point probe was not responsible for the measurement of voltage across the 4-

point probe, as the voltage across the inner electrodes also went to zero if the drive current was reduced to zero.

In order to calculate the gauge factor, the voltage between two inner electrodes is measured while actuating the PZT at resonant mode of the membrane with different amplitudes. Corresponding strain at each point is estimated using the linear relationship we came up using ABAQUS simulations (Figure 3.8).

4.5 Experimental Results

The resistivity increases at both compressive and tensile strains. Optical interferometer measurement of membrane displacements (Figure 4.6) indicates that the center part of the membrane moves similarly at positive and negative pressures due to pre-stress layer. The measured graphene gauge factor is orders of magnitude higher than that of most piezoresistive materials used in MEMS such as doped polysilicon and metals. Doped polysilicon can have gauge factors on the order of 30-40, while metals have a gauge factor of 55 [35, 36]. Resistivity changes of the graphene film as a function of vacuum up to 5mmHg and positive pressures up to 6mmHg are plotted in Figure 4.7.

The highly nonlinear behavior may be due to the fact that for either compressive or tensile stress the graphene membrane is stretched in the same direction. Another mechanism could be the generation of SiN polarization charge is of the same variety whether the stress is compressive or tensile, affecting the charges in graphene in the same way.

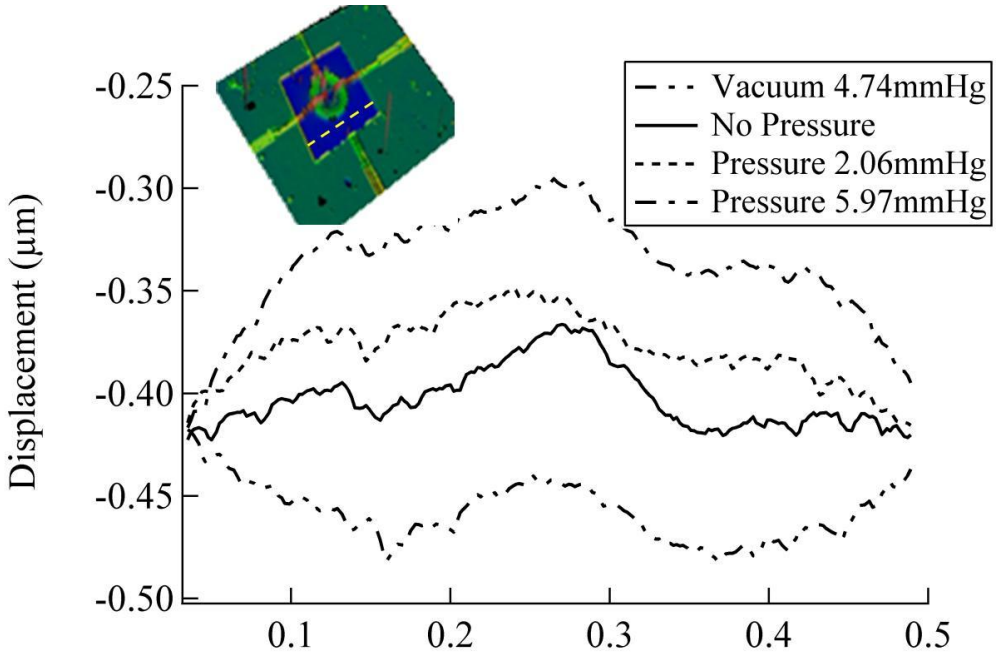

Figure 4.6 Zygo 7300 displacement profile along the shown the hatched line across the membrane. The dips show a pre-stressed nitride membrane due to the oxide film.

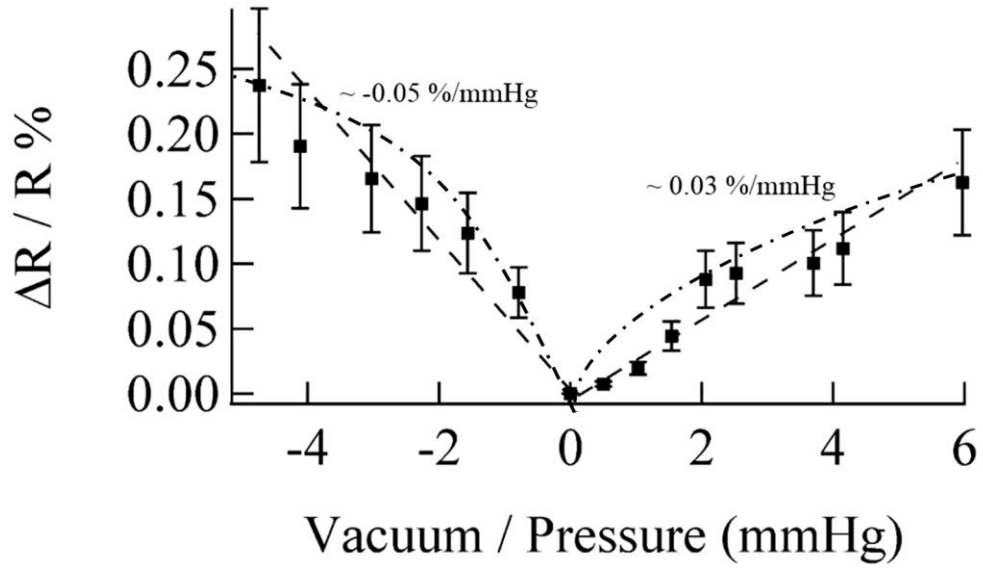

Figure 4.7 Resistivity change of graphene strain transducer as a function of pressure.

4.6 Conclusions

In summary, we present a pressure sensor process flow and results that pave the way for ultra-high sensitivity pressure sensors. Our estimated gauge-factor for this sensor is 11,300 matching that recently measured with AC resonance measurement of the graphene film [39]. However, we are exploring the exact reason for the nonlinearity -which maybe tunable for linear devices by adjusting the fabrication process- and ultra-high gauge factor we see in our on graphene/silicon-nitride hybrid stack based devices. Here, we are going to discuss two possible reasons: mobility modulation in graphene surface due to the surface charge effects in silicon nitride interface and stronger bonds between graphene and silicon-nitride surface than graphene and silicon-oxide.

4.6.1 Surface charges at graphene/Si_xN_y interface

The normalized change in resistivity in Figure 4.7 is asymmetric and relative resistivity increases no matter if the applied strain is tensile or compressive, proposing the decrease in mobility of carriers in graphene. In this section, we will describe some possible reasons for asymmetric nonlinearity at gauge factor curve in our graphene/silicon-nitride strain gauge and decrease in its carrier mobility at different applied strains.

The asymmetry around the zero point in Figure 4.7 is an indication of the presence of residual strain in the graphene at rest. This could be the result of the graphene transfer process and the induced changes in graphene topology on the silicon-nitride

membrane. Under these conditions, a compressive force (applying vacuum through the syringe at the setup shown in Figure 4.2) would gradually detach the flake from the substrate, as manifested by the higher initial slope in compression and the subsequent plateau at high strains. Similar effect is reported in previous studies -where mechanical behavior of graphene under both tension and compression has been studied- shows that when a rippled graphene is stretched, there will be a point in the deformation history whereby a greater portion of the mechanical energy will contribute to bond stretching rather than unfolding of the graphene [48].

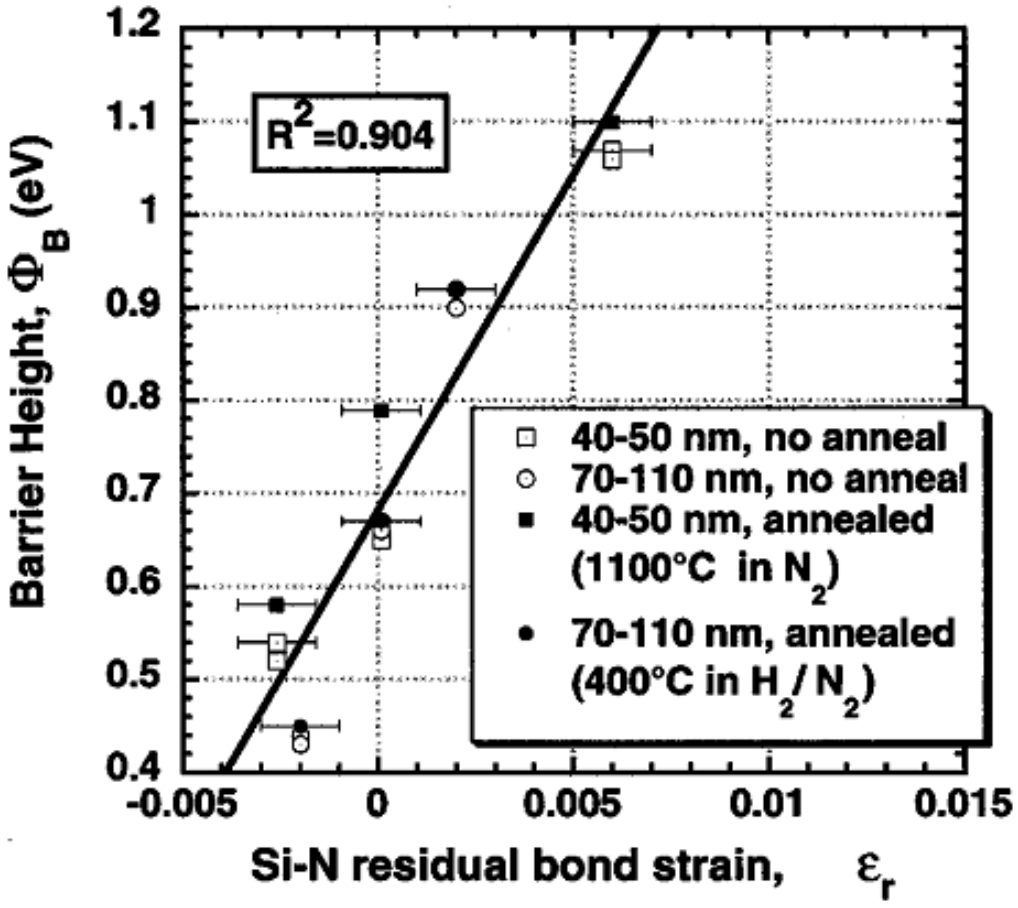

Figure 4.8 Energy barrier height as a function of the Si–N residual bond strain films for different thicknesses [49].

Relationship between silicon-nitride conductivity as a function of external applied mechanical strain has not been reported yet, but correlation of charge transport to local atomic strain in Si-rich silicon nitride thin films has been studied [49]. Figure 4.8 shows the linear dependency of the energy barrier height to the bond strain which is equivalent to the current density change by as much as seven orders of magnitude.

Also, recent studies show that the current–voltage and capacitance–voltage measurements exhibit an asymmetric electrical characteristic under different polarity of stress voltage [50]. Figure 4.9 shows the nonlinear assymtric behviour of current density at enriched silicon-nitride as a function of applied stress electric field.

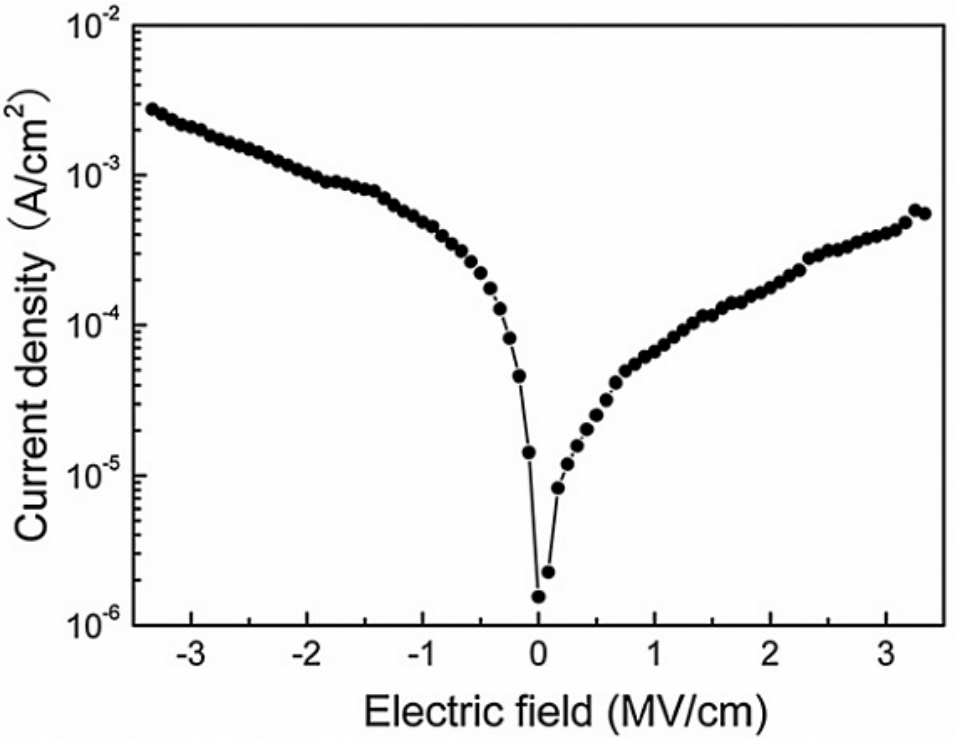

Figure 4.9 Current density at silicon-nitride as a function of applied electric-field stress at room temperature [50].

Dangling bonds form states that can trap either holes or electrons. Nitrogen dangling bonds have been observed in both LPCVD (low pressure chemical vapor deposition) and N-rich PECVD (plasma enhanced chemical vapor deposition) Silicon-nitride surfaces [51]. Figure 4.10 shows the silicon and nitrogen dangling bond densities calculation for CVD deposited Si_3N_4 using the tight-binding and recursion methods [52]. We propose that the presence of these dangling bonds might affect the mobility of graphene differently at different applied strains. It has been shown that current stressing in silicon-nitride introduces a range of defect concentrations and results in a change in conductivity as carriers move between charged states in a defect band [53].

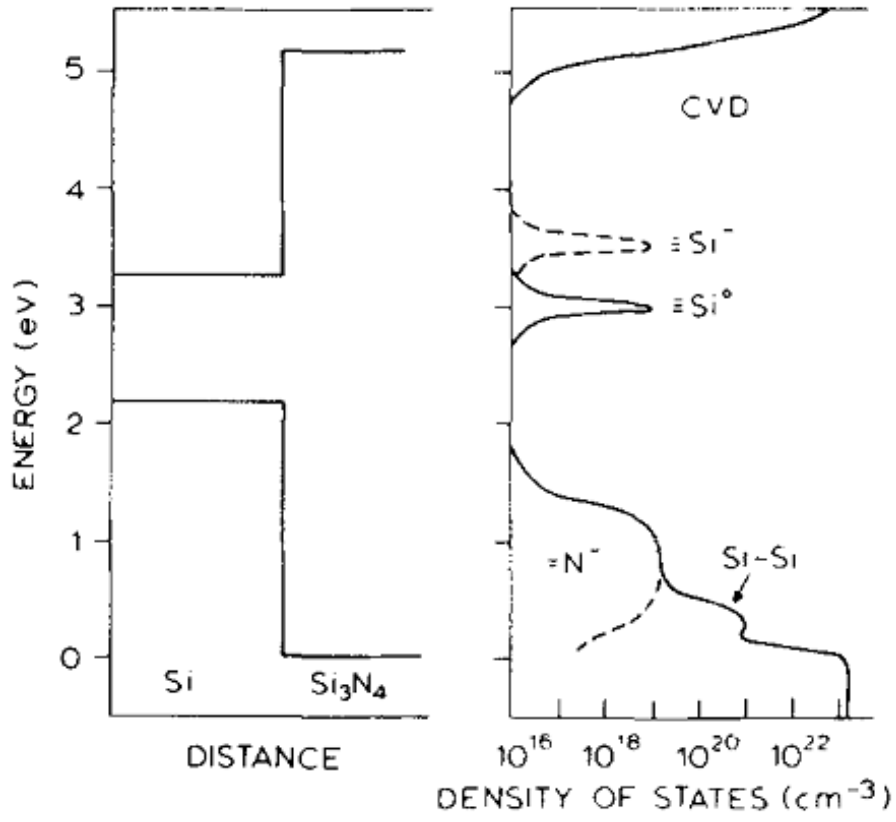

Figure 4.10 Densities of states for a CVD silicon nitride [52].

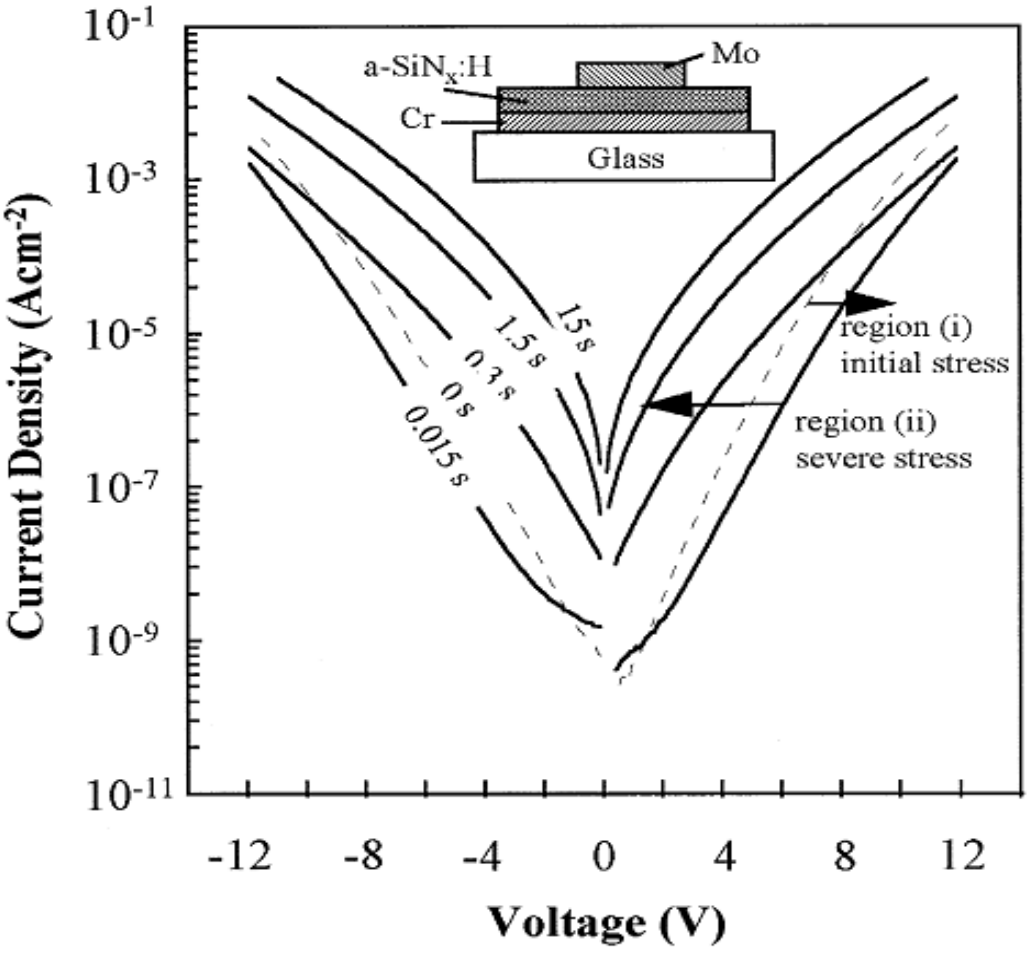

Figure 4.11 I-V characteristics of a-SiN:H MSM structure shows changes in conductivity at different current stress [53].

This change in conductivity has been studied in MSM (Metal Semiconductor Metal) structure of amorphous silicon-nitride as shown in Figure 4.11. The nonlinear behaviour of change in conductivity seen in this figure, may also effect the mobility of graphene surface and casue the nonlinear change in normalized resistivity measured in silicon-nitride hybrid stack (Figure 4.7).

4.6.2 Surface bonding between graphene and Si_xN_y surface

One of the restrictions for graphene-based devices is the great reduction of electron mobility, by orders of magnitude, when supported on a substrate [54]. Possible mechanisms that limit the mobility of graphene are charged impurity scattering [55] and surface roughness [56]. Recently, higher electron mobility was reported in graphene with Si_3N_4 thin films, deposited as the top gate dielectric [57]. Theoretical calculations for atomic and electronic structures of graphene on top of bulk β-Si_3N_4 substrate shows that the supported graphene (either single or bi- layer) is ultra flat [58]. As shown in Figure 4.12, the surface lattice constant of β-Si_3N_4 (0001) matches well with that of 3×3 graphene primitive cell. This ultra-flat surface may result in stronger covalence bond between graphene and Si_xN_y surface and transduce the applied strain on silicon-nitride membrane into the graphene surface more effectively.

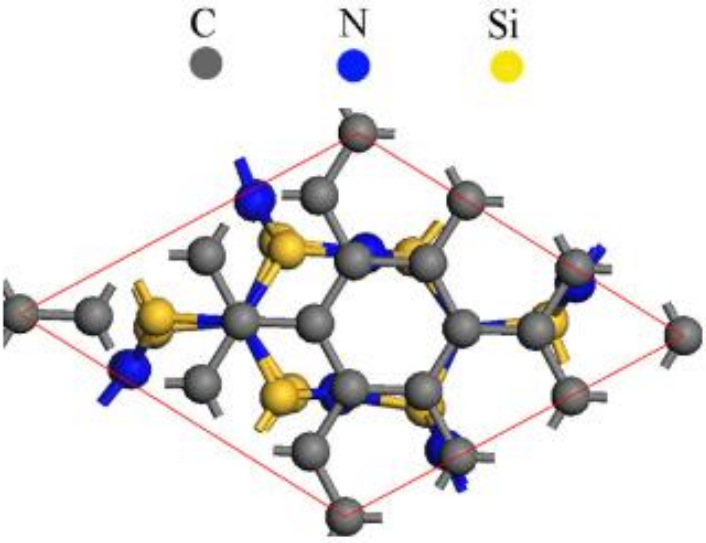

Figure 4.12 Top view of of the most stable interface structure for graphene on β–Si_3N_4 (0001) which shows it matches the irreducible triangle, formed by three high symmetric sites (top, bridge, and hollow site) in graphene [58].

CHAPTER 5

TIP-BASED GRAPHENE ETCHING FOR MEMS RESONATOR FREQUENCY TRIMMING

Many MEMS devices rely on resonant motion of microstructures such as beams or plates, employed in accelerometers, gyroscopes, RF-resonators, filters, biosensors, and AFM tips [59, 60, 61]. While some applications require the resonance frequencies of the structures to be within certain limits in order to conform to the specifications of readout electronics, measurement conditions, or to provide improved sensitivity, others require a precise match between resonance frequencies of two (identical) devices or two different modes of the same device. Common to all of the above cases is a need to adjust the resonance frequency of a given mode for a device since fabrication errors and variations make it difficult to get within ppm to ppb of the frequency targeted at the design phase.

Certain MEMS applications, such as inertial measurement using mode -matched gyroscopes, can have very demanding resolution requirements as mode matching needs to occur to 0.001 Hz for resonance frequencies of 10-20 kHz [62], corresponding to ppm to ppb fractional frequency shifts. To address the above need of frequency tuning, electrostatic forces, temperature control, and piezoelectrically induced stresses can be used [63, 64, 65]. In case of electrostatic tuning, the spring softening effect due to increasing DC bias across an electrostatic gap causes a decrease in the measured resonance frequency of the device. Although increasing the frequency above the base (no DC bias) value is not possible through this approach, its simplicity

makes it by far the most common frequency tuning mechanism in RF-MEMS filters and resonators [66]. Temperature controlled resonance frequency tuning is most easily realized by ovenizing the structure of interest with a heater in a feedback loop [63]. Although, this method provides an accurate and stable method of frequency tuning, power consumption makes it unattractive for many low-power, portable applications. Use of piezoelectricity induced stresses provides a solution to the power consumption issue. In addition, polarity of the frequency shift can easily be reversed by reversing the potential applied across the piezoelectric material [67]. However, these methods are only applicable when deposition of piezoelectric films, which is not standard in many MEMS foundries, is part of the process-flow.

Different from methods mentioned so far that caused reversible (temporary) changes in the device properties and the resonance frequencies, irreversible (permanent) frequency shifts can be generated by selective material deposition and removal from the device of interest. Some examples to this approach include scanning tunneling microscope (STM) aided resonator length adjustment [62], use of Focused Ion Beam for active layer deposition and removal [68], resistive heating to change and/or remove material from the mechanical structure of the resonator, or pulsed laser deposition on packaged chips of resonators [69]. Laser tuning can be used to remove material, but is generally coarse.

Two crucial metrics for frequency tuning of resonators are its resolution and dynamic range, i.e. maximum and minimum achievable frequencies. On the other hand, resolution of frequency tuning by selective material removal is directly related to the smallest mass that can be removed with the technique at hand.

Our insight to achieving high resolution is to add a “very thin” material and use well-controlled removal from this material. Graphene, which has ideally single atom thickness, is a great candidate in this approach, and it is used in this chapter to achieve atomic-scale mass and elasticity control and ppm level resolution by selective removal using an SPM tip through electrochemical etching or adhesion to contacting tip surface.

5.1 Device Fabrication

The resonator we investigate consists of a silicon-nitride membrane driven by attached PZT plate (Figure 5.1). A low-stress silicon nitride membrane of 100 nm thickness realized over a 4-inch silicon substrate using LPCVD deposition and anisotropic etching of the silicon substrate. The Si_xN_y membrane is then coated with stack of Cr (5nm)/Ti (20nm) using thermal evaporation. Next, the metal layer is etched to form a four point probe structure (Figure 5.2). This structure consists of progressively thinner wires converging from gaps of 10um to 1um. A graphene layer, prepared using CVD deposition [70] is transferred on top of the electrodes. The back electrodes are necessary to form the electrochemical circuit for etching graphene. The graphene-nitride bond is reliable as we have shown before [39]. The process of graphene transfer involves spinning a thin (300nm) PMMA on top of graphene followed by wet etching of the copper foil. The silicon wafer which includes the nitride membranes is used to lift the PMMA/ Graphene bilayer floating on top of the Cu etch beaker. Acetone is used to remove the PMMA and samples are cleaned within

DI water and let to dry for 6 hours. A PZT plate is adhesively attached to the back-side of the silicon die, with two wires soldered to the PZT plate.

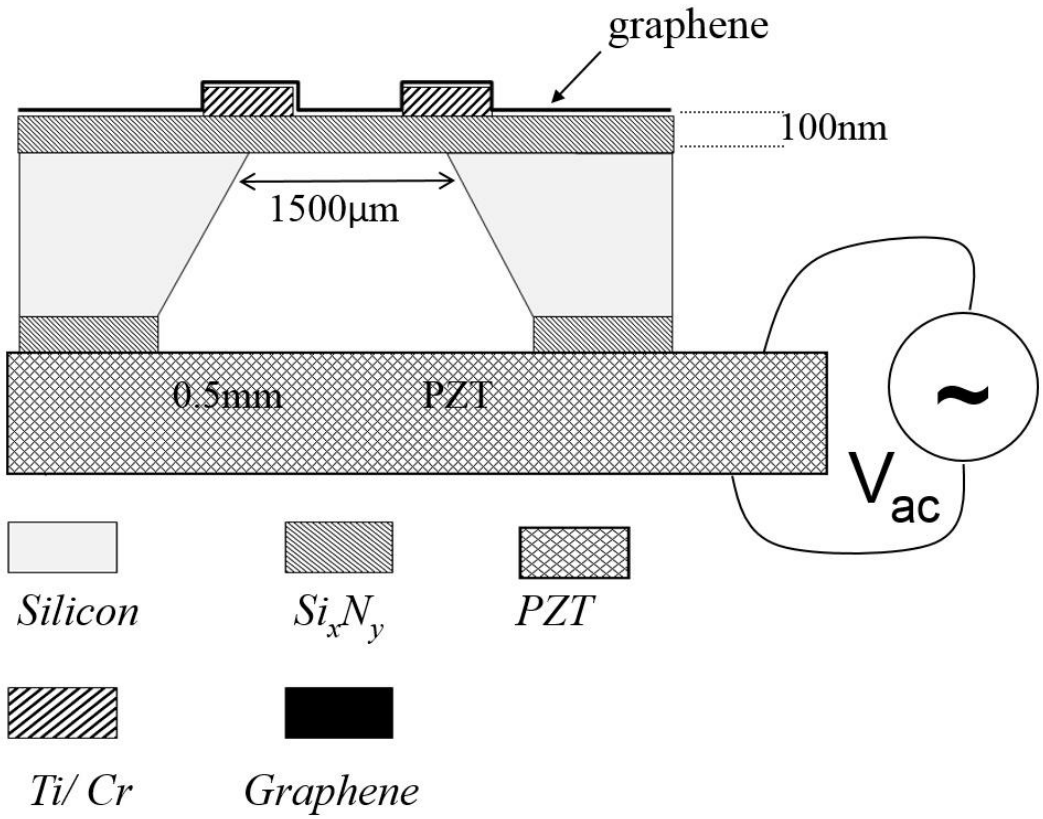

Figure 5.1 Schematic of resonator with graphene layer, transferred on to and PZT, attached to the bottom.

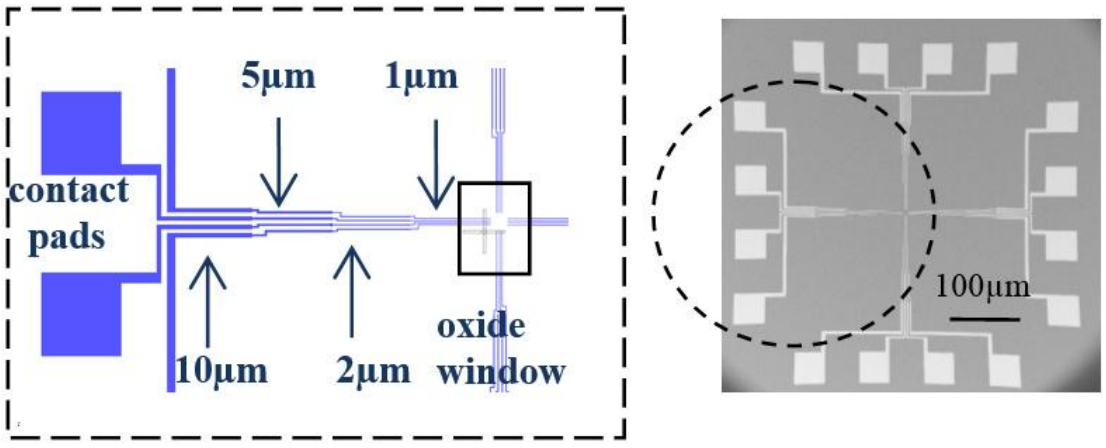

Figure 5.2 Image of 4-point probe electrodes on a silicon nitride membrane to measure the resistivity of graphene layer (right) and schematic of this structure(left)

5.2 Graphene Etching

Here we have developed a graphene cutting process using an STM tip [71]. The process of graphene etching is due to an aqueous electrochemical oxidation and removal of the surface carbon atoms (Figure 5.3a). The water is supplied by the meniscus that forms between the carbon surface and the scanning probe tip from the ambient moisture. The main graphene etching reaction is the generation of carbon dioxide [72] is shown in Equation 5-1.

$$C+2H_2O \leftrightarrow 4H^+ + 4e^- + CO_2 \qquad \text{Equation 5-1}$$

At low bias voltages the carbon can be oxidized and is removed. Another mechanism is the physical stripping of carbon atoms at sufficient voltages. To reach the electrochemical potential, sufficient voltage needs to be applied to the tip to provide voltage potential on the surface for reactions. After several hundred hole-punches in the graphene film, part of the removed carbon atoms are deposited on the tip. The increased tip diameter results in poor imaging and lithographic resolution.

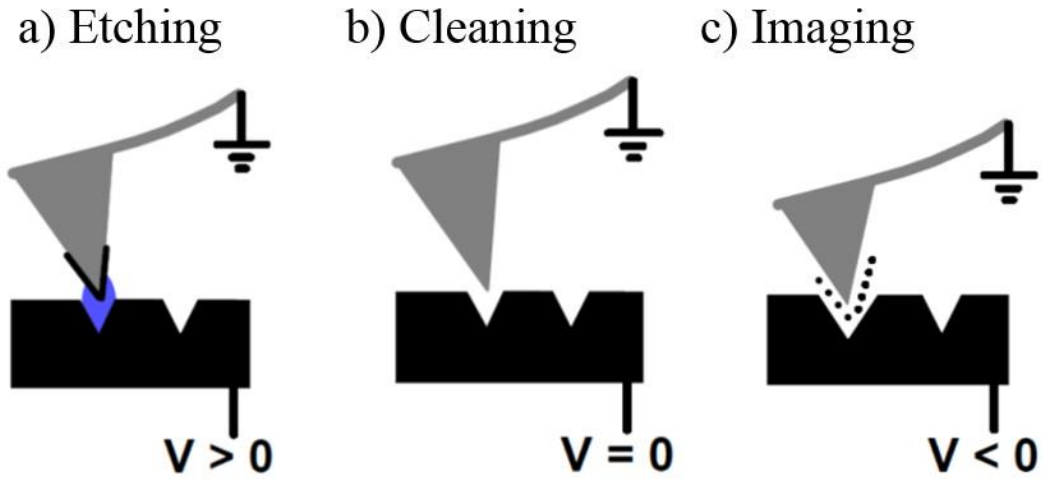

Figure 5.3 Schematic summary of modes of operation for STM graphene etching: (a) etching at positive sample bias voltages with a meniscus formed between the tip and the sample (b)tip

cleaning of carbon deposits at negative sample bias voltages (c) image scans at zero bias voltage.

It is found that this can be simply remedied by applying a large negative sample bias (-10V), opposite in polarity from the voltages used in graphene etching (Figure 5.3b). Platinum STM tips were used: platinum has been found to catalyze the electrochemical corrosion of carbon [72]. The presence of the water is surprising, as graphene is hydrophobic. This may be a combined effect from surface modifications to the carbon and a change in pH of the water due to the etching process. The etching process in addition to removing carbon can also oxidize the carbon, which will decrease its hydrophobicity. The lithographic feature size is determined by the size of the meniscus that forms between the scanning probe tip and the graphene surface. The meniscus size is mainly determined by the environment, probe parameters, and tip height. The temperature dependence can be exploited to control the feature size. As the temperature of the graphene surface increases, the evaporation rate at the edges of the meniscus increases, resulting in a narrower meniscus and smaller feature size.

Figure 5.4 shows the before and after STM pictures of the graphene etching process. The thermally-reduced meniscus yields smaller feature sizes but increased etch times. It is estimated that the average etch rate decreases from a maximum 2×10^6 atoms/second to a minimum 2×10^5 atoms/second.

5.3 Results

The measurement of the vibration displacements of the membrane under PZT actuation was conducted both in vacuum and air.

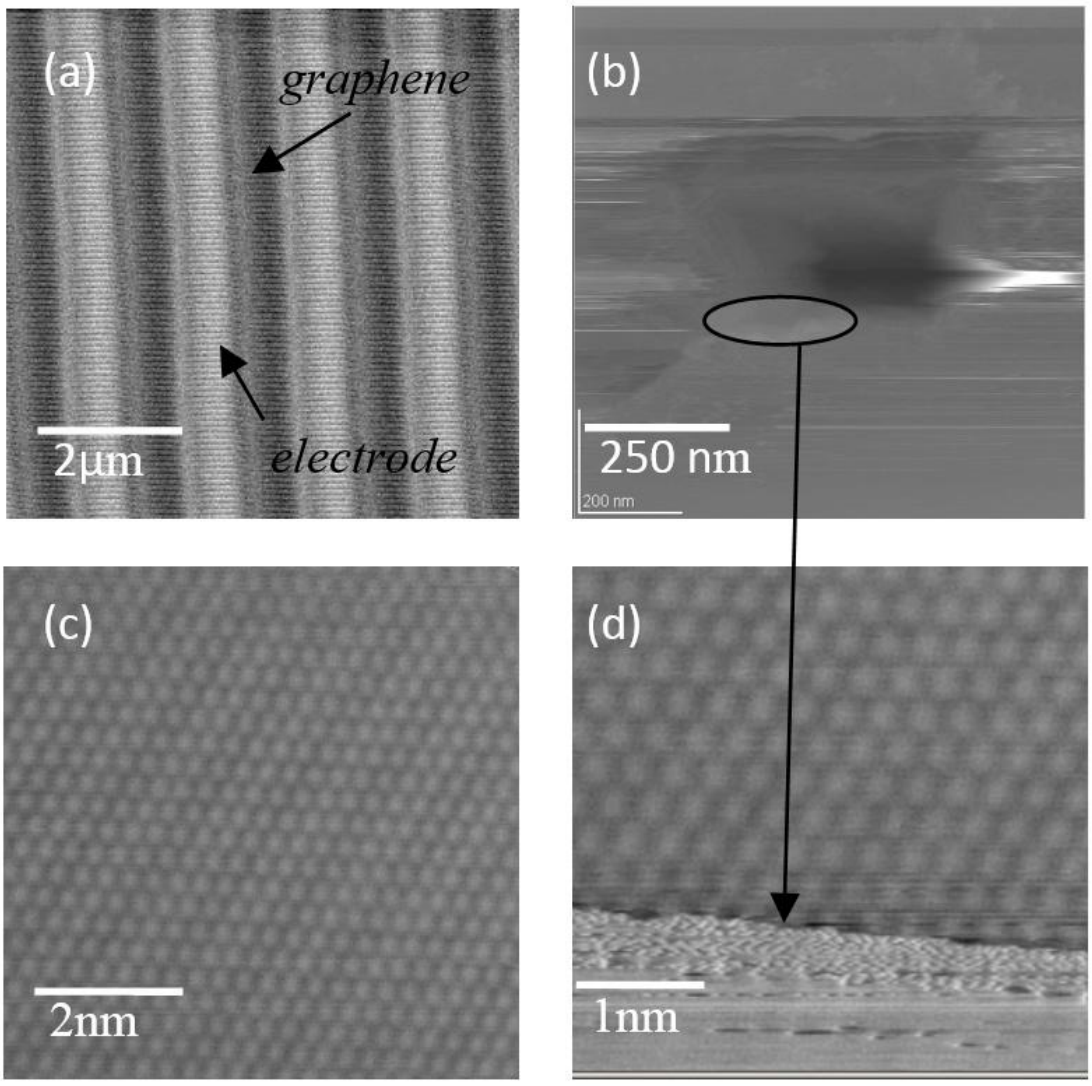

Figure 5.4 STM images of electrodes with graphene on top(a), a 100nm ×250nm etched area on graphene (b), graphene atoms before cut (c), and graphene/nitride interface after cut (d).

In order to perform static analysis, we modeled our device with a supported rectangular plat with thickness *h*, and edge dimensions *a* and *b*. The plane is made of an isotropic material having density ρ, Poisson's ratio v (taken as 0.3 in calculations), and elastic modulus *E*. Fundamental natural frequency of the unstressed flat plate is given by [73]:

$$\Omega_1 = \pi^2 \left((1/a^2) + (1/b^2)\right) \sqrt{(D/(\rho h))} \Omega_1 = \quad \text{Equation 5-2}$$

$$\pi^2((1/a^2) + (1/b^2))\sqrt{(D/(\rho h))}$$

where D is the plate flexural rigidity given by

$$D = Eh^3 / (12\,(1\text{-}\nu^2)) \qquad \text{Equation 5-3}$$

In order to include the effect of in-plane strain in SixNy membrane, simulations are performed using finite element package ABAQUS for the entire PZT/Silicon/Membrane structure. Plane strain analysis is used here due to relatively large depth of the structure, compared to its thickness, which gives good agreement with preliminary 3D simulations of the same. We have shown that a stress of 220MPa gives good agreement with the experiments and is within the expected range of stress obtained during fabrication [39].

Natural frequencies of rectangular membrane with in-plane stress are estimated using the numerical solutions to the equations (4) and (5) [73]:

$$D\pi^4\left(\left(\frac{p}{a}\right)^2 + \left(\frac{q}{b}\right)^2\right)^2 (Z_{p,q} - Z_{0p.q})\left(\frac{ab}{4}\right) - \int_{x=0}^{a}\int_{y=0}^{b}\left(F_{,yy}z_{,xx} + F_{,xx}z_{,yy} - 2F_{,xy}z_{,xy}\right)\sin\left(\frac{p\pi x}{a}\right)\sin\left(\frac{q\pi y}{b}\right)dxdy = 0 \qquad \text{Equation 5-4}$$

$$[K]\{H\} = \omega^2[M]\{H\} \qquad \text{Equation 5-5}$$

with $z(x,y)$ out of plane static displacement, $F(x,y)$ static Airy stress function, $z_0(x,y)$ small imperfection, N_x and N_y biaxial normal in-plane loadings and [K] and [M] stiffness and mass matrices, respectively. Total $n_x \times n_y$ can be calculated by obtaining one nonlinear cubic equation for each choice of p and q. Several resonant modes (Figure 5.5) were observed (using a POLYTEC interferometer) which fits well into the

calculated *n*th natural frequency of the membrane, $\omega_{n,}$ where $\omega_n = \lambda_n \times \Omega_n$ and λn is the *n*th natural frequency parameter calculated numerically.

We picked the mode at 420 kHz to track the ability to etch graphene and track the frequency, because of its highest quality factor. In analyzing the mass response of the membrane, we assume that graphene mass does not change the mechanics of the device. The frequency shift [17] is then simply:

$$\frac{\Delta f}{f} \approx -\frac{1}{2}\frac{\Delta m}{m} \qquad \text{Equation 5-6}$$

To start the frequency shift measurement, graphene is transferred on top of the membrane.

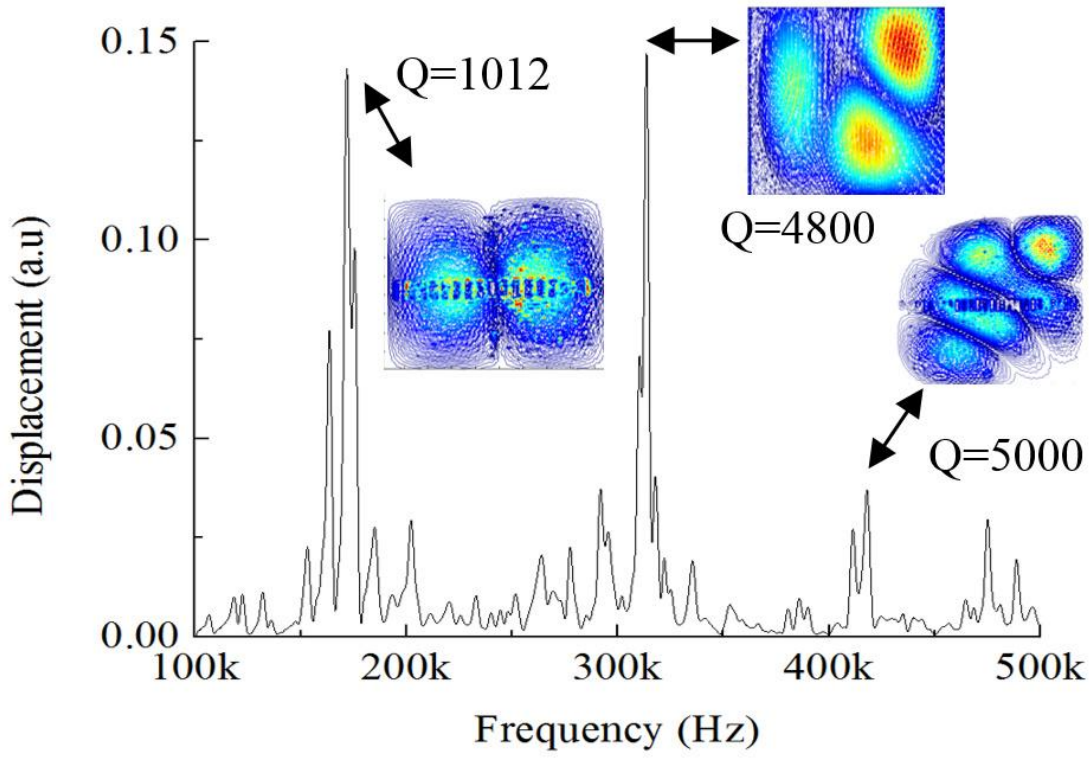

Figure 5.5 Frequency response of resonator at frequencies from 100KHz to 500KHz. Corresponding mode mapping is shown at three major peaks.

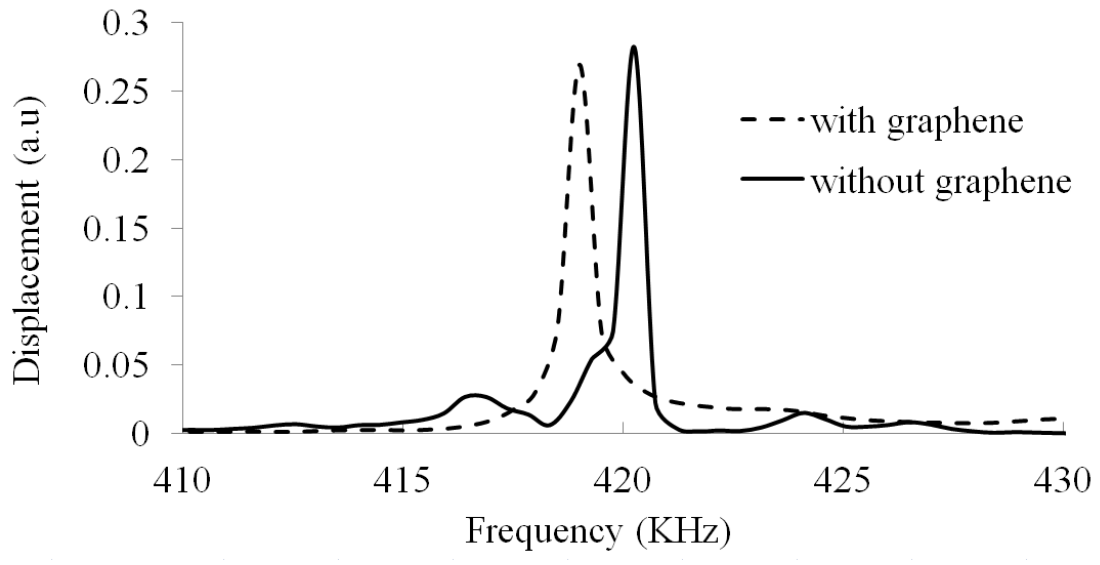

Figure 5.6 Resonator frequency response shifts left after graphene transfer due to added mass.

Figure 5.6 shows the frequency shift associated with adding the graphene on top of the membrane, and as expected the frequency was reduced due to the added mass corresponding to 300ppm. The Q of the resonance also dropped by 15 percent, probably due to the higher loss in graphene. Then tip cutting was used to cut the graphene between two electrodes. The cutting was monitored by measuring the current between two electrodes, electrical resistance increased as atoms were removed (Figure 5.7).

The resonance frequency shifts were measured before and after cutting. As seen in Figure 5.8, we could achieve 7-3×10^3 ppm shifts.

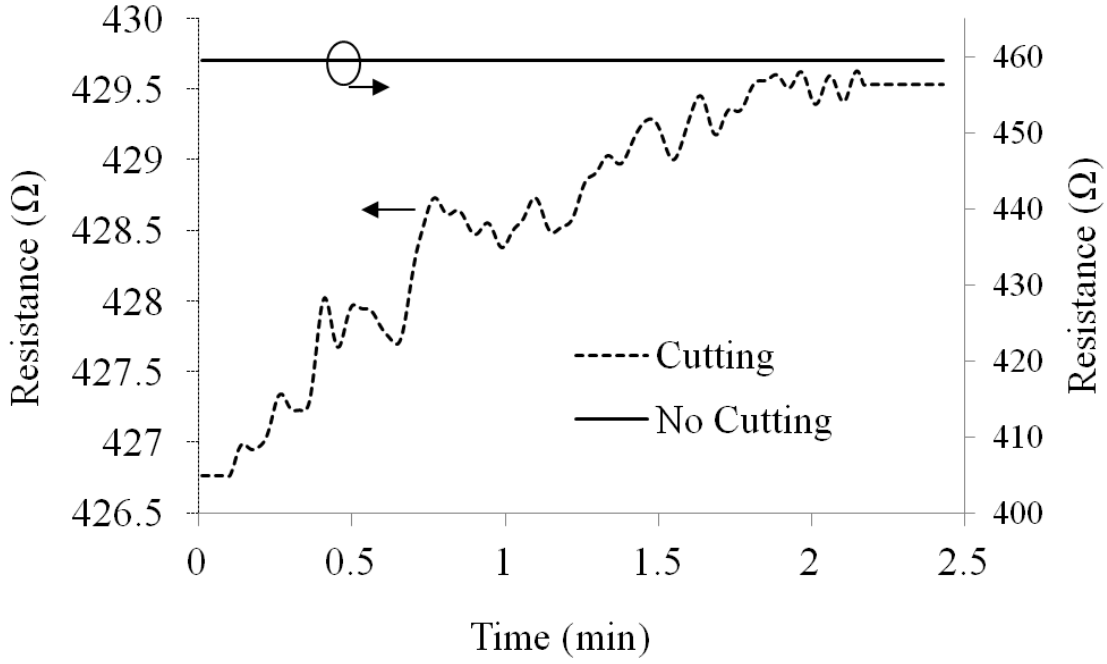

Figure 5.7 Graphene resistance during cut between two electrodes where graphene is not cut in that area and the other two electrodes where graphene is cut .

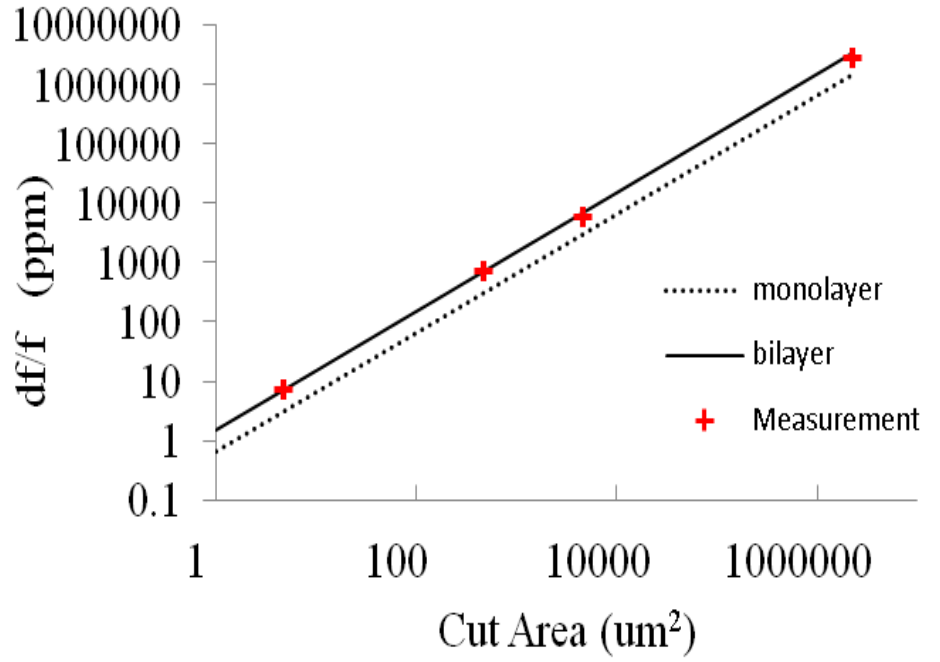

Figure 5.8 ppm change in frequency as a function of etched area on graphene – Cut area is in μm^2.

5.4 Conclusions

The minimum resolvable mass is given as [74]:

$$\delta m = \frac{\partial M}{\partial f}\delta f \times 10^{\frac{-DR}{20}} \approx -\frac{2M_{eff}}{Q} \times 10^{\frac{-DR}{20}} \qquad \text{Equation 5-7}$$

where M=7.4×10^{-16}g graphene mass per μm^2, Q=5000 is the quality factor and *DR* is the dynamic range (function of temperature). Previously, the minimum sensitivity for a monolayer graphene nanomechanical resonators at T=5K is calculated as 7.6×10^{-22}g/√Hz [74]. Table 5-1 shows the precision of different methods in order to tune the frequency of given structure. Using the graphene removal method, we report 7.6 ppm shifts in frequency by removing attached graphene films. Two approaches are under investigation in order to reach ppb resolutions in frequency tuning. First, the etching resolution can be increased at higher temperatures due to the evaporation of water meniscus and second, the graphene/Si_xN_y membrane mass ratio will decrease when the thickness of the Si_xN_y film increases. There is a drop in Q that is still unexplained, and experiments are in progress to explain the results.

Table 5-1 Comparison of frequency tuning resolution, achieved by different methods on different structures.

Device Structure	**Method**	**Frequency Tuning (ppm)**	**Ref**
Micro-resonator	Laser Tuning	5000	[69]
On-chip silica microdisk resonators	HF etching	200	[75]
Monolayer Graphene Nanomechanical Resonators	Mass removal	15	[74]
Our Device	**Mass removal**	**7.6**	**This work**

APPENDIX

A1. WAVELENGTH-LOCKED LASER (THEORY)

Assume the wavelength of the laser and the laser current has the following relationship where Γ is an arbitrary constant.

$$\lambda = \Gamma * I \qquad \text{Equation 5-8}$$

If laser current is modulated by sinusoidal signal V_{mod} the equation above can be re-written as,

$$\lambda = \Gamma(\, I_0 + I_{ac} \cos(wt)\,) \qquad \text{Equation 5-9}$$

Let's make another assumption that change in wavelength and V_{PD}have quadratic relationship. Note that K and C are arbitrary constants.

$$V_{PD} = K(\lambda - \lambda_0)^2 + C \qquad \text{Equation 5-10}$$

By plugging equation (2) into equation (3) will give,

$$V_{PD} = K[\Gamma(\, I_0 + I_{ac} \cos(wt)) - \lambda_0]^2 + C \qquad \text{Equation 5-11}$$

By letting $A= \Gamma I_0 - \lambda$ and $B= \Gamma I_{ac}$ equation (4) can be re-written as,

$$\begin{aligned} V_{PD} &= K(A - B\cos(wt))^2 + C \\ &= KA^2 + 2KAB\cos(wt) \\ &\quad + KB^2\cos^2(wt) + C \end{aligned} \qquad \text{Equation 5-12}$$

V_{PD} and $V_{ref}=V_0\cos(wt)$ is multiplied by the lock-in amplifier

$$V_{PD} \times V_0 \cos(wt) = (KA^2 + C)V_0 \cos(wt) + KV_0 2AB \cos^2(wt) + KB^2 V_0 \cos^3(wt) \quad \text{Equation 5-13}$$

and this multiplied signal goes into a low-pass filter which is essentially an integrator. This newly created signal is the output of lock-in amplifier or V_{LIA}.

Since $\int \cos(wt)\, dt = 0$, $\int \cos^2(wt)\, dt = \pi$, and $\int \cos^3(wt)\, dt = 0$

$$\therefore V_{LIA} = 2KV_0AB\pi = 2KV_0B\pi(\Gamma I_0 - \lambda) = 2KV_0B\pi(\lambda_0 - \lambda) = 2KV_0B\pi(\Delta\lambda) \quad \text{Equation 5-14}$$

Equation 5-14 shows that the output of the lock-in amplifier will react to the deviation of the wavelength from $\lambda_0$which means that in ideal case the laser current can settle to a point where the absorption is maximized.

A2. WAVELENGTH-LOCKED LASER (EXPERIMENTAL DATA)

In this section input and output signal along with quantitative data acquired during the course of experiment are discussed. Note that, due to drift in frequency of the laser the numeric values of input signals required to lock the laser will be different time to time. This is a guideline to repeat the experiment.

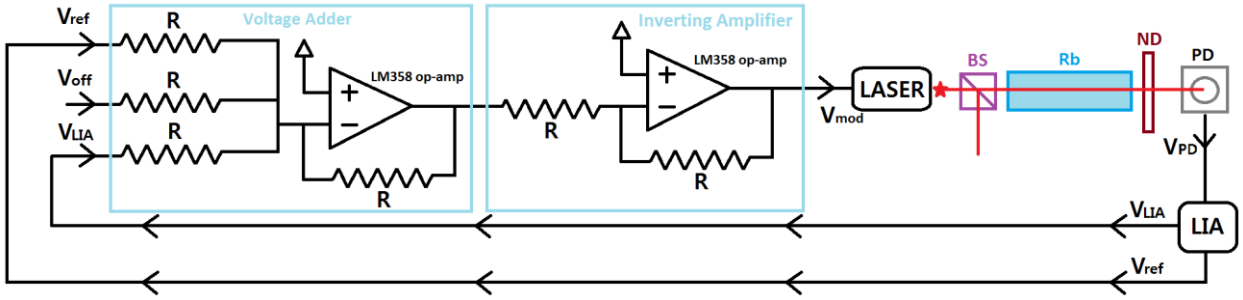

Figure A1: Circuit diagram for experimental setup

1.Wide range sweep (Figure 4)

$$\mathbf{I_0} = 75\ \text{mA} \qquad \text{Equation 5-15}$$

I_0 is initial laser current. This value should be fixed for the rest of the experiment.

$$f = 100\ \text{Hz} \qquad \text{Equation 5-16}$$

f is the frequency of V_{ref} which is essentially the sweeping frequency of the laser. This value should be fixed for the rest of the experiment.

$$\mathbf{V_{ref}} = V_{0,ref}\sin(2\pi ft) \quad \text{where } V_{0,ref}=245\text{mV} \qquad \text{Equation 5-17}$$

V_{ref} is reference signal generated by the lock-in amplifier.

$$\mathbf{V_{off}} = 2.26\ \text{V} \qquad \text{Equation 5-18}$$

$V_{off}$is offset voltage which is used as a fine adjustment control for laser current.

$$\mathbf{V_{PD}} = V_{dc,PD} + A_m\sin(2\pi ft) + \sum A_i(t) \qquad \text{Equation 5-19}$$

where $V_{dc,PD}$= 220 mV and A_m=10 mV

V_{PD} is the output from the photodetector. Its DC component, $V_{dc,PD}$,is related to I_0 and V_{off} which determine the output power of the laser. Its AC component, $A_m\sin(2\pi ft)$, is related to V_{ref} which is the reference signal that dominates the sinusoidal component of the laser modulation signal. $\sum A_i(t)$ represents the multiple

absorptions caused by rubidium's atomic transitions shown in Figure 4. Note that $A_i(t)$ is an arbitrary periodic function.

$$\mathbf{V_{LIA}} = V_{dc,LIA} + p(t) \qquad \text{Equation 5-20}$$

where$V_{dc,LIA}$=55 mV and p(t) <4mV

V_{LIA} is the output of the lock-in amplifier. In ideal case, V_{LIA} should have dc component only as shown in A.1 (7) however in wide range sweep case VPD contains frequency component other than f (as shown by multiple absorption signals in Figure 4) that phase sensitive term p(t) will remain. This is not important until $V_{0,ref}$ becomes small that lock-in is feasible. V_{LIA} should not be connected to the adder at this point because it is a meaningless signal and could alter the wavelength of the laser to an undesired direction.

$$\mathbf{V_{mod}} = V_{ref} + V_{off} + V_{LIA} + E(t) \qquad \text{Equation 5-21}$$

where $E(t) << V_{mod}$

V_{mod} is the modulation signal for the laser. As shown in Figure A1, V_{mod} is the sum of V_{ref} ,V_{off} , and V_{LIA}. E(t) is a small error which is caused by non-linearity of the op-amps used in the adder and the inverting amplifier.

$$\mathbf{I_{tot}} = I_0 + V_{mod}\cdot(10\ \text{mA/V}) \approx 97 + 2.2\cdot\sin(2\pi f t)\ \text{mA} \qquad \text{Equation 5-22}$$

I_{tot} is the total laser current. The modulationinput sensitivity of TopticaDCC110 current controller is 10 mA/V.

2. Narrow range sweep (Figure 6)

$$\mathbf{I_0} = 75\ \text{mA},\ \boldsymbol{f} = 100\ \text{Hz} \qquad \text{Equation 5-23}$$

$$\mathbf{V_{ref}} = V_{0,ref}\sin(2\pi f t) \qquad \text{Equation 5-24}$$

where $V_{0,ref}$=66mV.

$$\mathbf{V_{off}} = 2.28\ \text{V} \qquad \text{Equation 5-25}$$

V_{off} has been adjusted slightly in order to make the peak of the absorption to occur at the middle of the V_{PD}'s peak-to-peak signal as shown in Figure 6.

$$\mathbf{V_{PD}} = V_{dc,PD} + A_m\sin(2\pi ft) + A_1(t) \qquad \text{Equation 5-26}$$

where $V_{dc,PD}$= 220 mV and A_m=2 mV

Because there is only one atomic transition occurs $\sum A_i(t)$ term is removed and replaced with $A_1(t)$ which represents D2 transition of rubidium. Note that $A_1(t)$ is an arbitrary periodic function.

$$\mathbf{V_{LIA}} = V_{dc,LIA} + p(t) \qquad \text{Equation 5-27}$$

where $V_{dc,LIA}$=28 mV and p(t) < 4mV.

Phase sensitive term p(t) still remains because of absorption shown in Figure 6. This is not important until $V_{0,ref}$ becomes really small that lock-in is feasible. V_{LIA} should not be connected to the adder at this point because it is a meaningless signal and could alter the wavelength of the laser to an undesired direction.

$$\mathbf{V_{mod}} = V_{ref} + V_{off} + V_{LIA} + E(t) \qquad \text{Equation 5-28}$$

where $E(t) << V_{mod}$

$$\mathbf{I_{tot}} = I_0 + V_{mod}\cdot(10\ \text{mA/V}) \approx 97 + 0.6\cdot\sin(2\pi ft)\ \text{mA} \qquad \text{Equation 5-29}$$

3. Lock-in sweep (Figure 10a, 10d)

$$\mathbf{I_0} = 75\ \text{mA and}\ \boldsymbol{f} = 100\ \text{Hz} \qquad \text{Equation 5-30}$$

$$\mathbf{V_{ref}} = V_{0,ref}\sin(2\pi ft) \qquad \text{Equation 5-31}$$

where $V_{0,ref}$=8 mV

$\mathbf{V_{off}}$ = 2.28 V

$$\mathbf{V_{PD}} = V_{dc,PD} + A_{lock\text{-}in}\sin(2\pi ft) \qquad \text{Equation 5-32}$$

where $V_{dc,PD}$= 220 mV and $A_{lock\text{-}in}$=0.25 mV.

If the V_{ref} is so small that it only sweeps the absorption regionV_{PD} essentially becomes a sinusoidal wave which is in-phase with V_{ref}.

$$\mathbf{V_{LIA}} = V_{dc,LIA} + p(t) \qquad \text{Equation 5-33}$$

Where $V_{dc,LIA}$=6 mV and $p(t) \approx 0$ mV.

Because V_{ref}isin-phase with V_{PD}, p(t) will be eliminated from V_{LIA} and only DC component will remain.At this point V_{LIA} should not be connected to the adder.

$$\mathbf{V_{mod}} = V_{ref} + V_{off} + V_{LIA} + E(t) \qquad \text{Equation 5-34}$$

where $E(t) << V_{mod}$.

$$\mathbf{I_{tot}} = I_0 + V_{mod} \cdot (10 \text{ mA/V}) \approx 97 \text{ mA} \qquad \text{Equation 5-35}$$

A3. SUBPIXEL IMAGE REGISTRATION

Image registration algorithm is used in NORIS to calculate the displacement between two positions. This is done by finding the offset of two images (reference image and sample image which is acquired in each actuation step) in pixels and multiplies it with the size of the imager's photocell. Such pixel offset can be calculated through cross correlation. Let $I_R(x,y)$ and $I_S(x,y)$ are same sized, grey scale images to compare. Then the offset is (x_0, y_0) that maximizes the cross correlation of the images.

$$\mathrm{CC}(x_0, y_0) = \sum\sum I_R(x, y) \times I_S(x - x_0\,, y - y_0) \quad \text{Equation 5-36}$$

This method however is not so reliable when a pixel has considerably higher intensity than other pixels. Errors due to such outliers can be reduced by normalizing the cross correlation.

$$\mathrm{CCN}(x_0, y_0) = \sum\sum \frac{[\, I_R(x, y) - \bar{I_R}] \times [I_S(x - x_0\,, y - y_0) - \bar{I_S}]}{\sigma_{I_R}\sigma_{I_S}} \quad \text{Equation 5-37}$$

To achieve nanometer accuracy the images has to be upsampled because typical size of photocell is micron scale. Upsampling can be done by zero padding the images.[4]

A4. EQUIPMENTS AND PARTS, USED FOR NORIS MINIATURIZATION

Name	Manufacturer	Part No.	Purpose
Diode Laser Head	Toptica photonics	DL 100	Part of laser system
Supply Rack	Toptica photonics	DC 110	Part of laser system
Current Control	Toptica photonics	DCC 110	Part of laser system
Temperature Control	Toptica photonics	DTC 110	Part of laser system
Scan Control	Toptica photonics	SC 110	Part of laser system
Lock-in regulator	Toptica photonics	LIR 110	Part of laser system
Temperature Controller	Thorlabs	TC 200	Temperature controller for Rb cell heater
Heater for reference cells	Thorlabs	GCH25-75	Heater for reference cells
Photo detector	Thorlabs	DET36A/M	Measures laser intensity
3-axis piezo controller	Thorlabs	MDT693A	3-axis piezo controller
Microblock 3-axis positioner	Thorlabs	MBT602	Grating holder
Laser diode mount	Thorlabs	HLD001	Grating holder with temperature control
T-Cube TEC controller	Thorlabs	TTC001	Temperature controller for HLD001
Beam splitter	Thorlabs	BS023	Beam splitter
DAQ	National Instruments	USB-6259	Applies voltage signal to piezo controller
Neutral Density filter	Unknown	Unknown	Reduces beam intensity
Operational amplifier	Unknown	LM358	Voltage adder, inverting ampifier
Power supply	Agilent	E3630A	Power supply for voltage adder and inverting amplifier
Oscilloscope	Agilent	54624A	Oscilloscope
Lock-in amplifier (Phase Sensitive Detector)	Stanford Research System	SR810	Wavelength lock-in
Spectrum analyzer	Hewlett Packard	70951A	Spectrum Analyzer
Webcam	Microsoft	VX-3000	CMOS imager
AFM	Veeco	3100D	Piezo actuator
Signal access module	Veeco	SAM III	Control module for Veeco AFM

A5. LABVIEW CODES

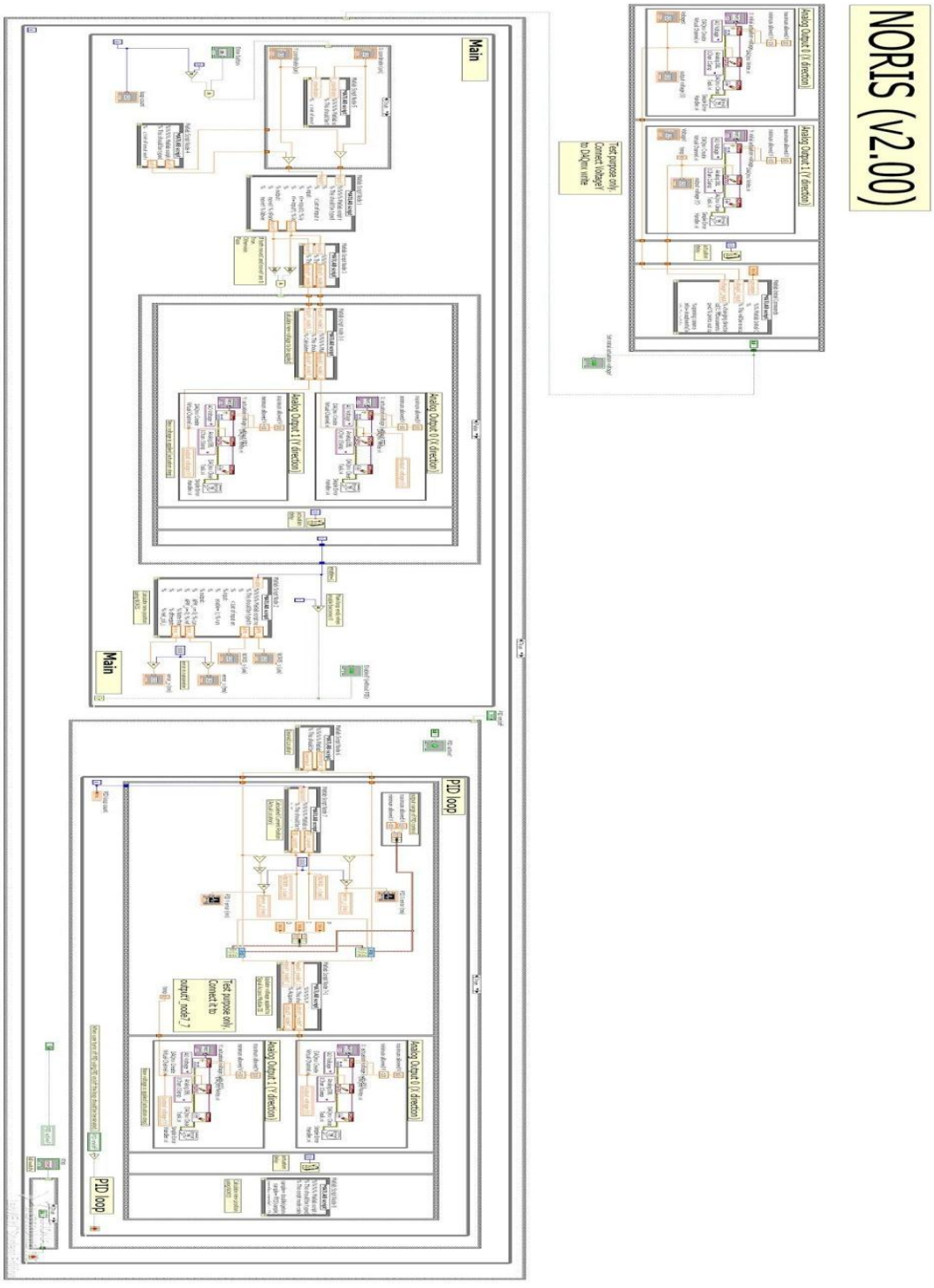

Labview codes for etching graphene are modified and are based on codes written by Bryan Hicks, Cornell ECE masters student [76].

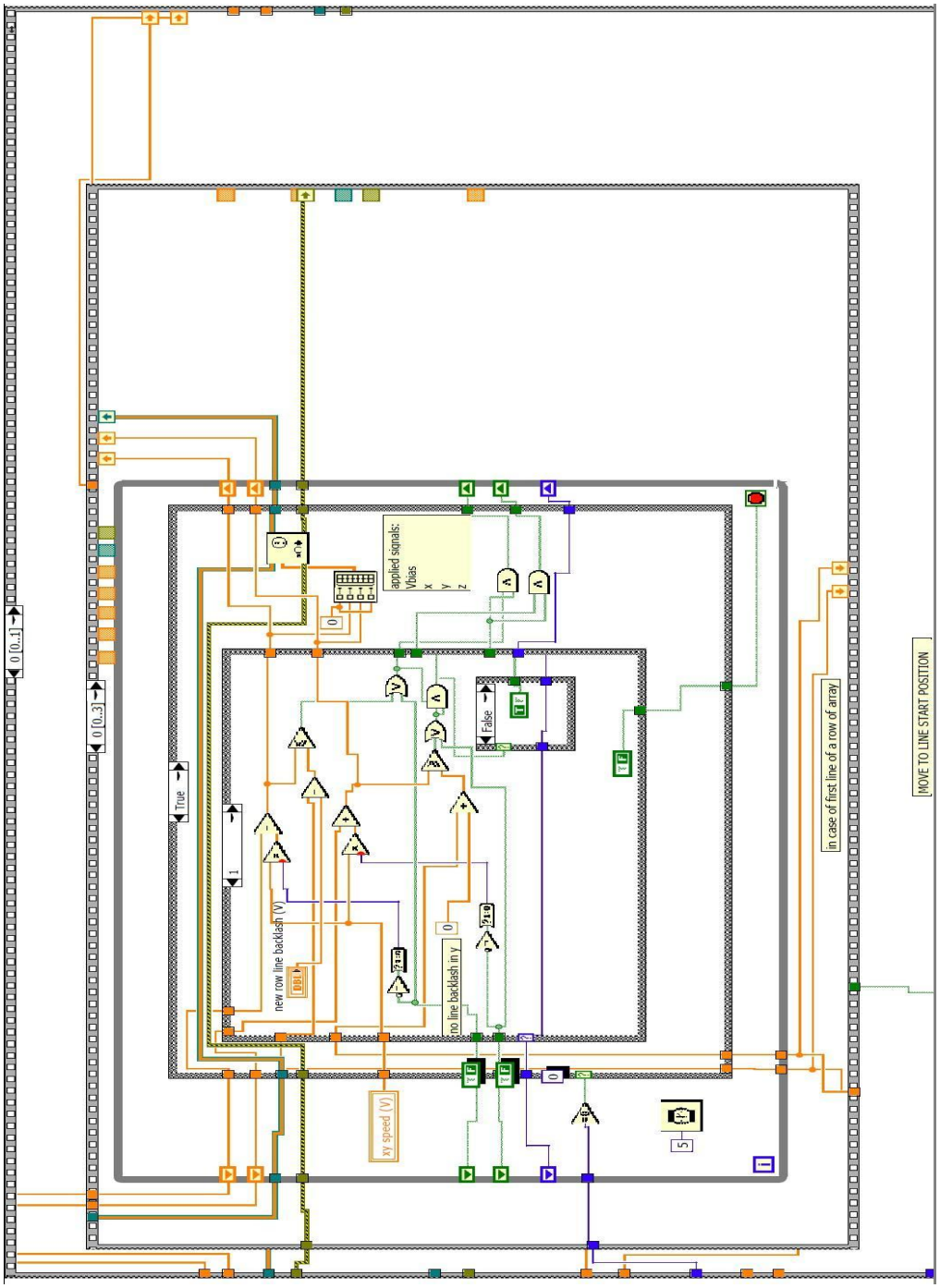

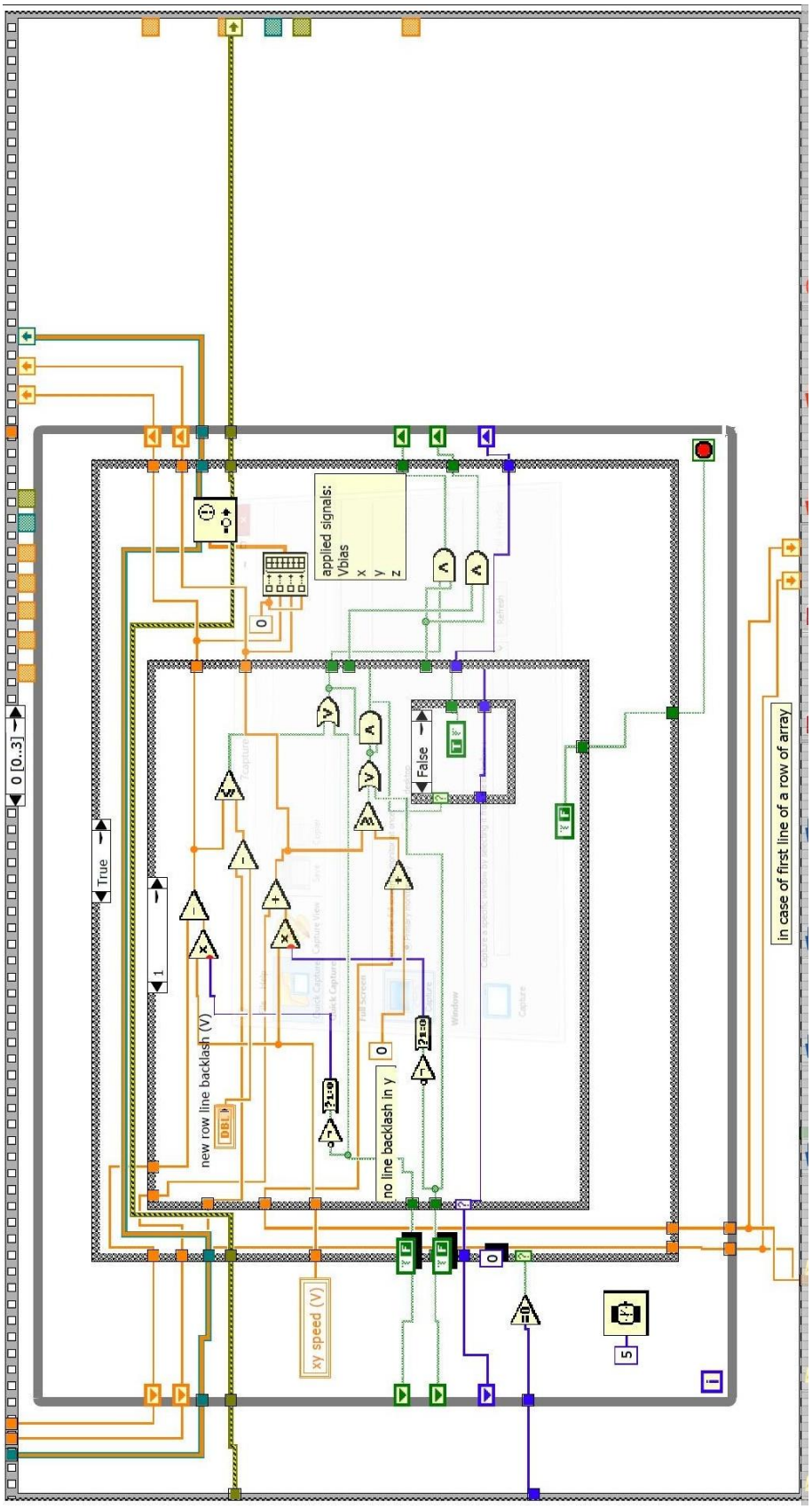
applied signals:
Vbias
x
y
z
0 [0..3]
True
False
1
new row line backlash (V)
no line backlash in y
xy speed (V)
in case of first line of a row of array
5

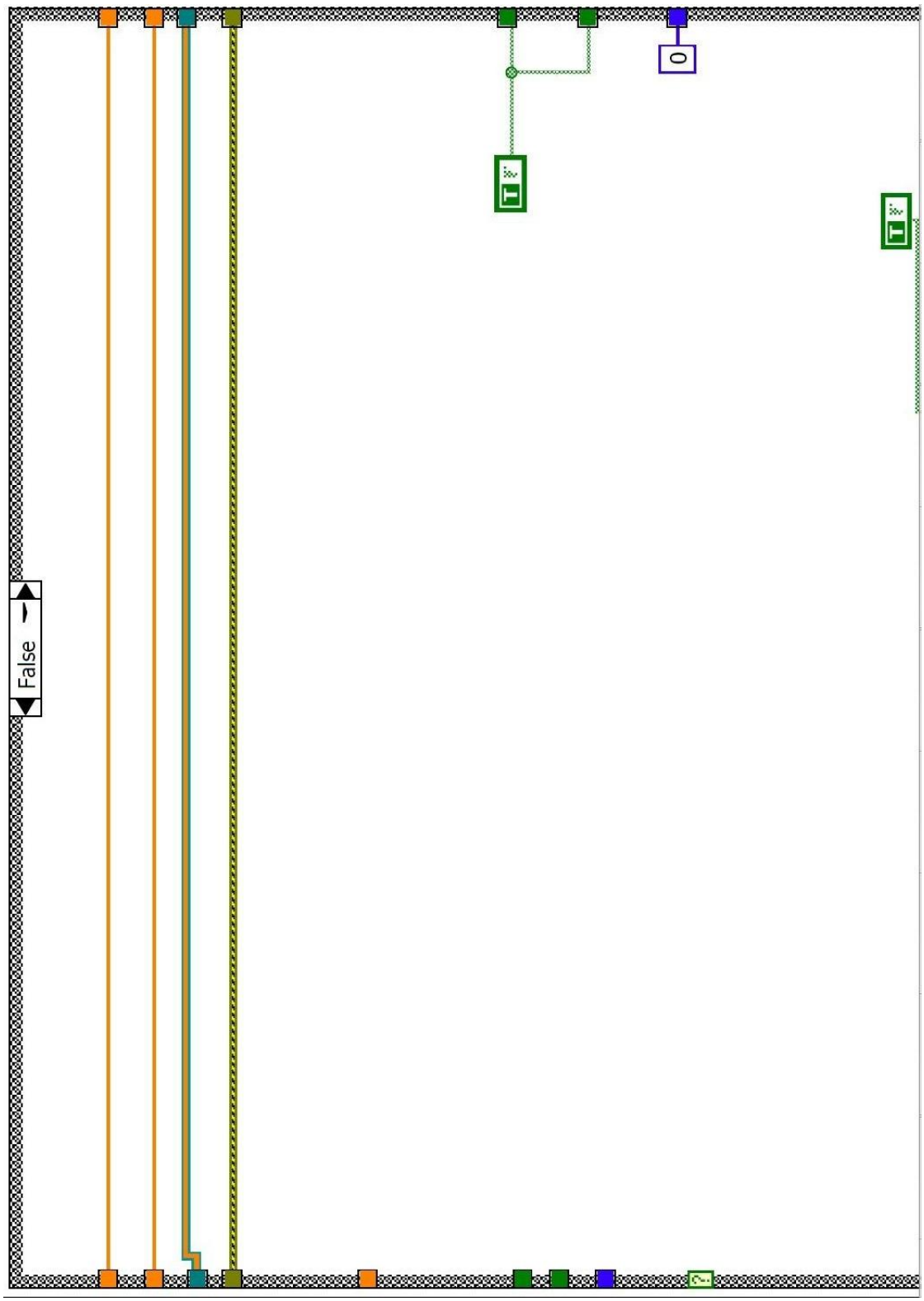
0
False

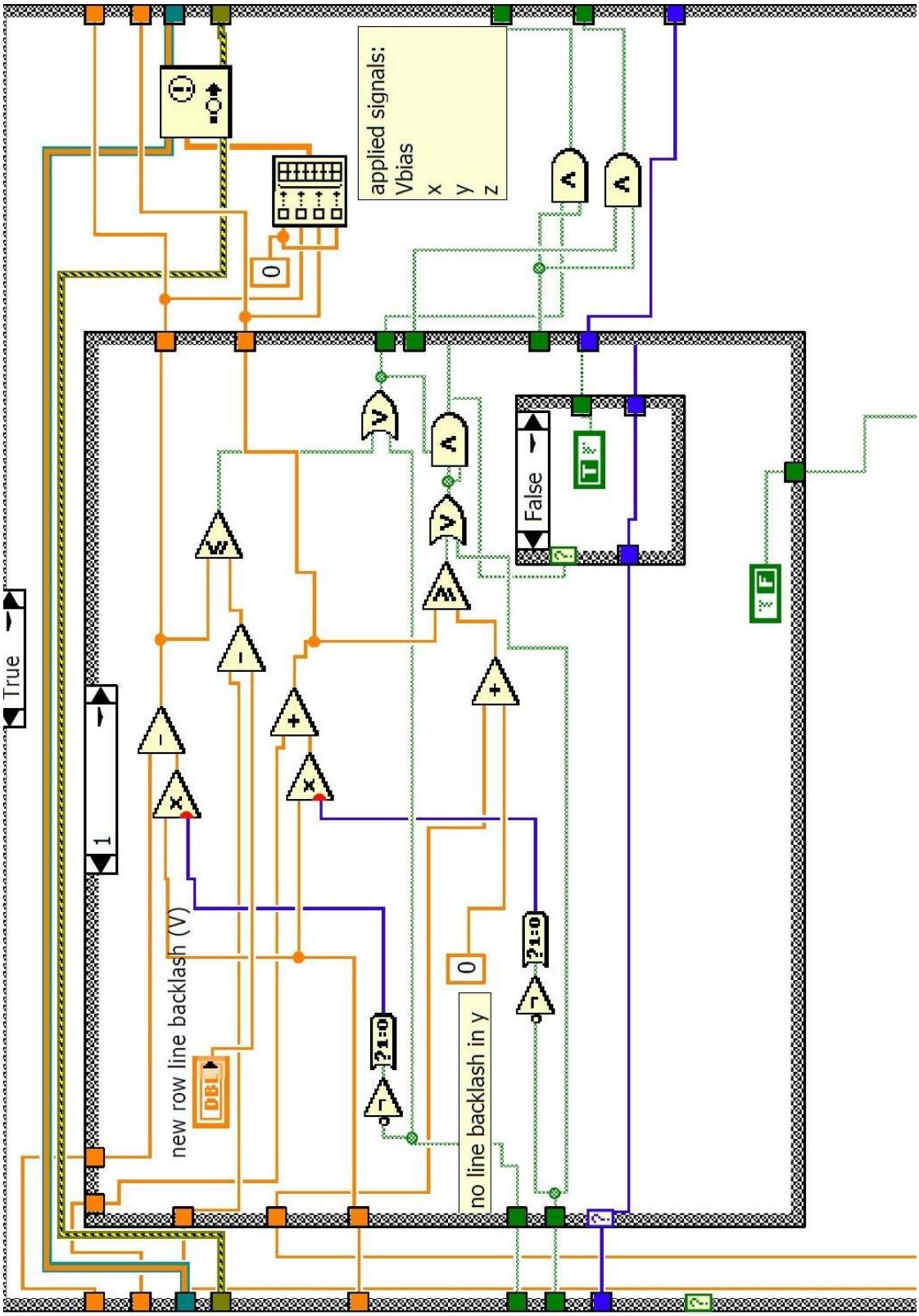
applied signals:
Vbias
x
y
z
True
False
new row line backlash (V)
no line backlash in y
DBL
0
1
?1:0

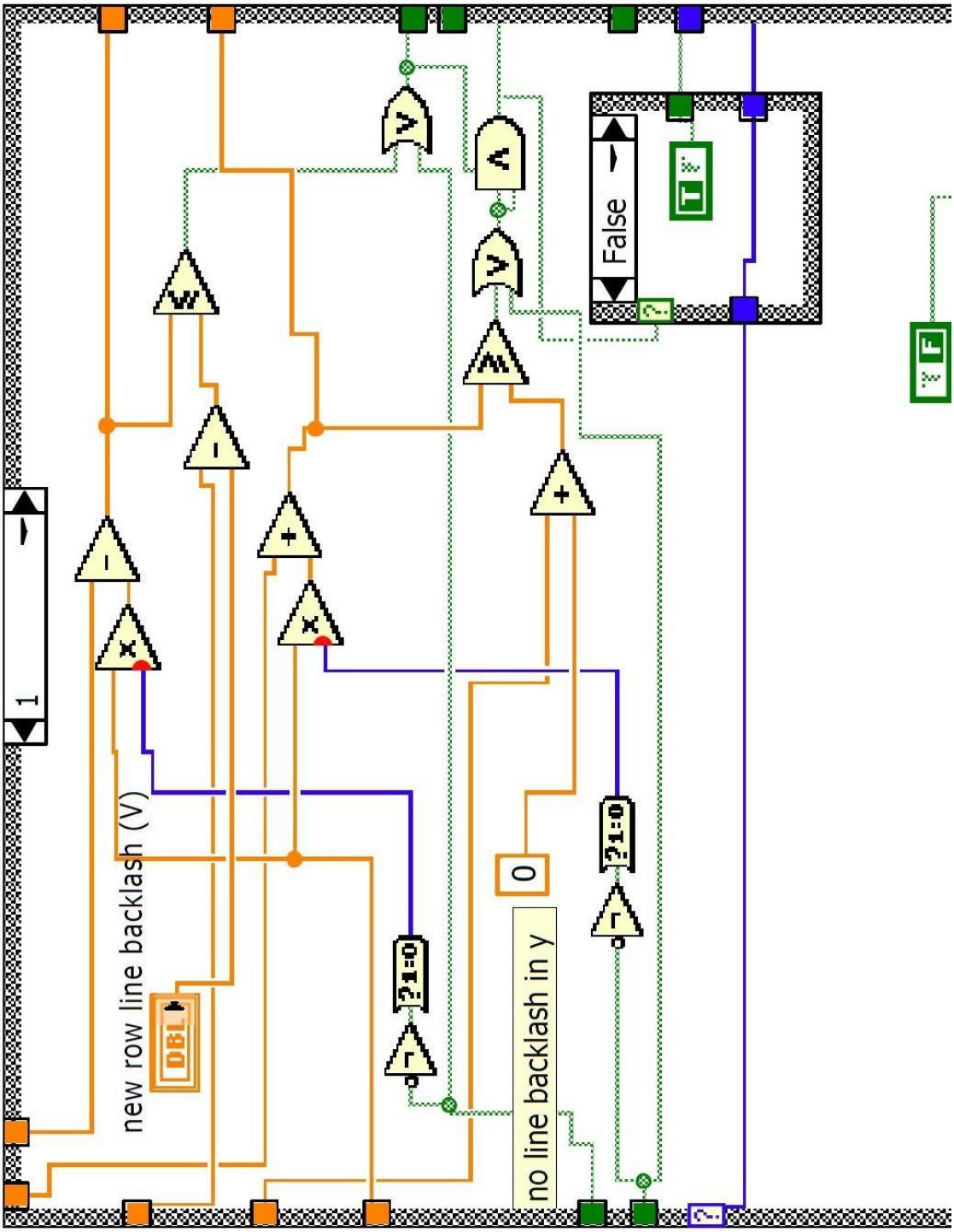
new row line backlash (V)
DBL
no line backlash in y
0
21:0
False
T
F

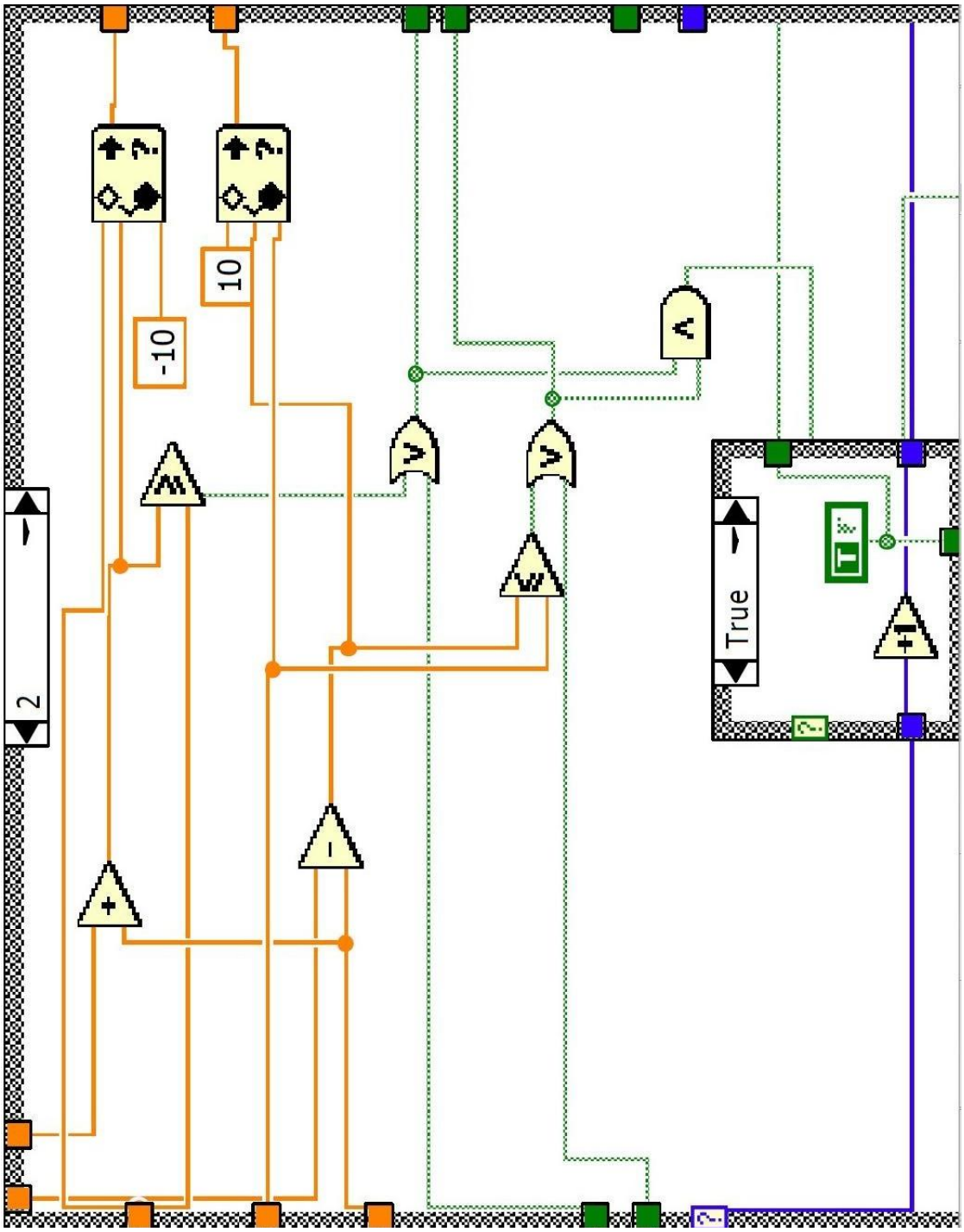
10
-10
2
True

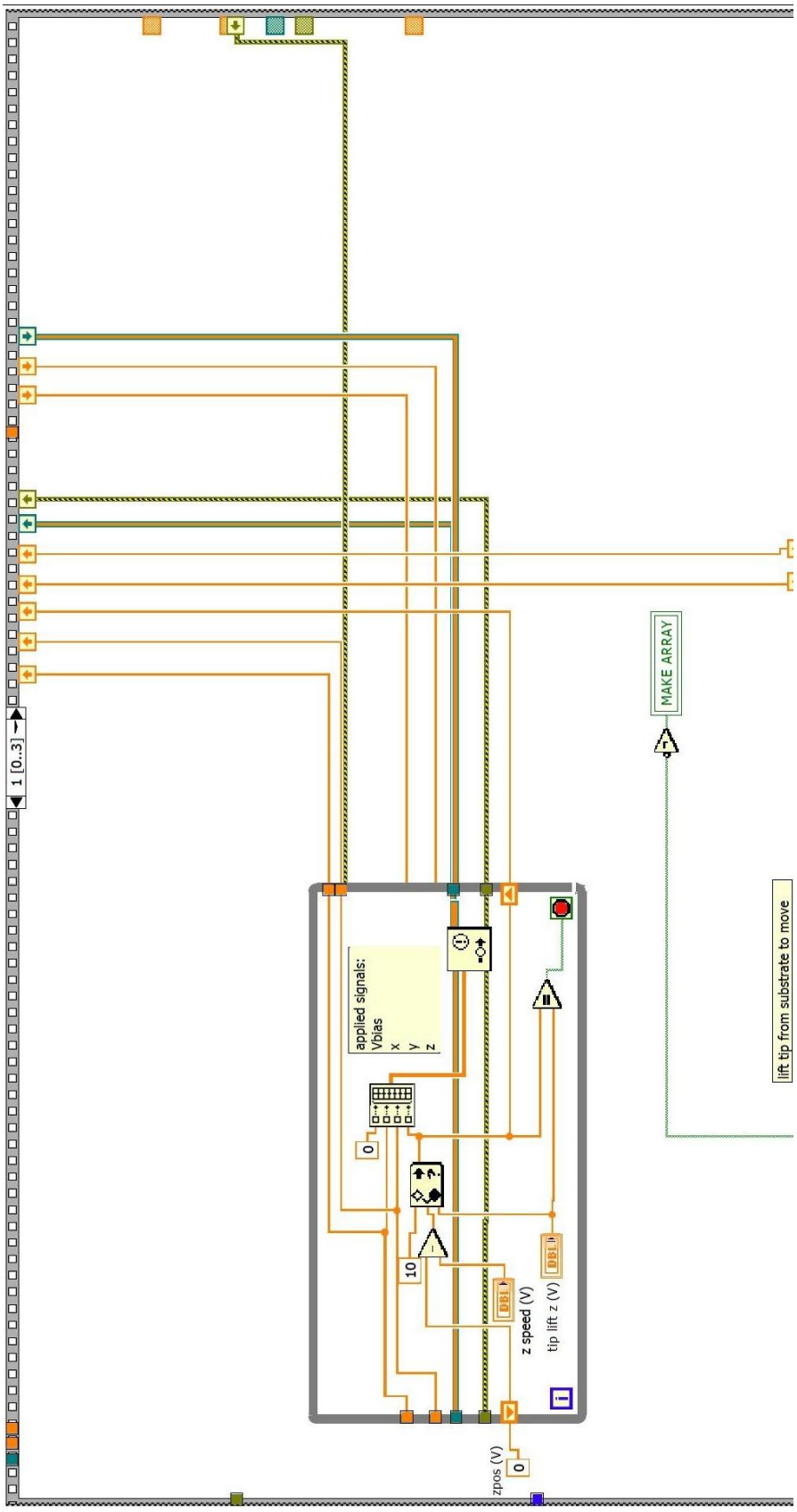
1 [0..3]
MAKE ARRAY
lift tip from substrate to move
applied signals:
Vbias
x
y
z
0
10
z speed (V)
tip lift z (V)
zpos (V)
0

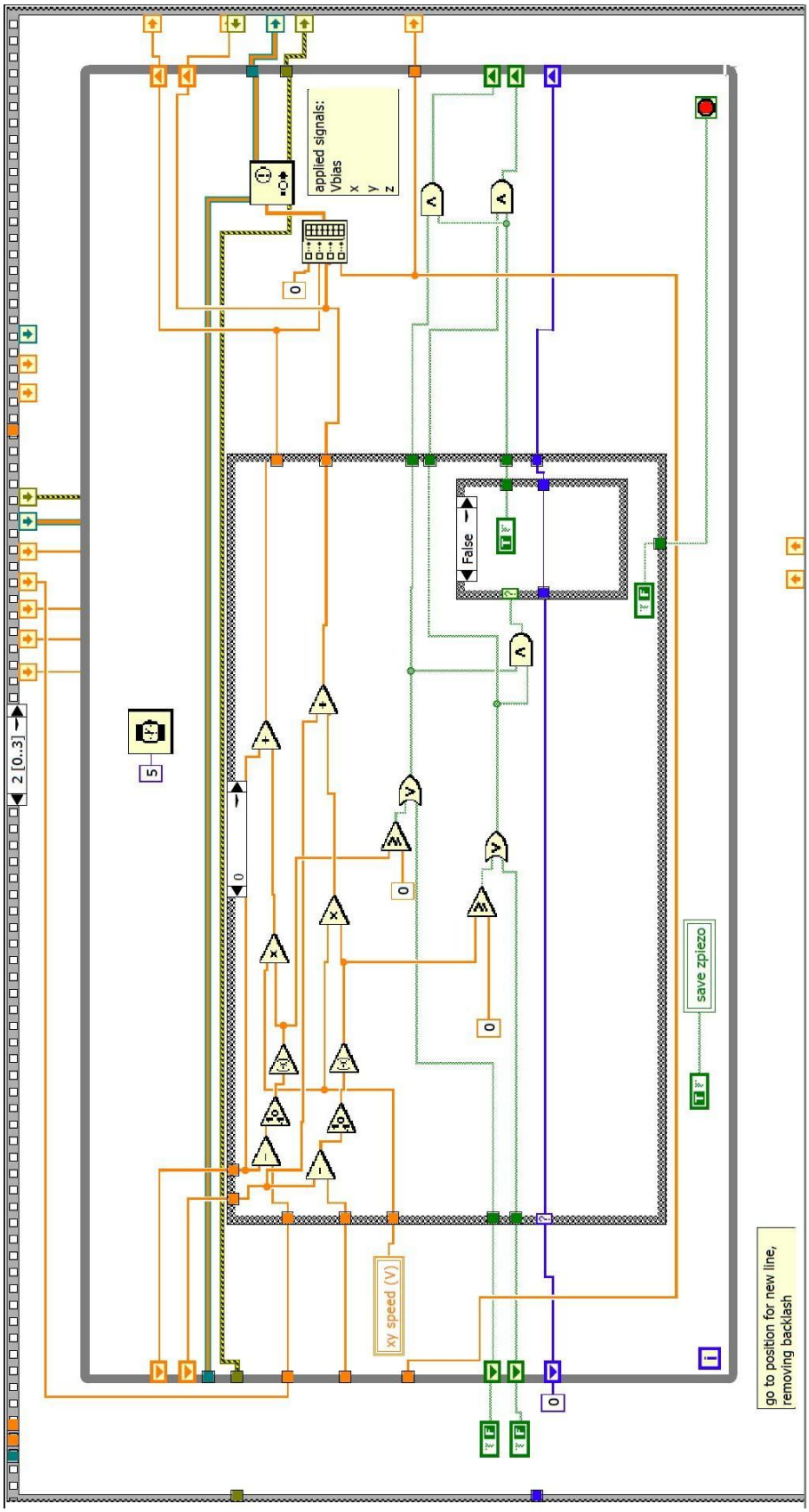
applied signals:
Vbias
x
y
z
False
save zpiezo
xy speed (V)
go to position for new line,
removing backlash

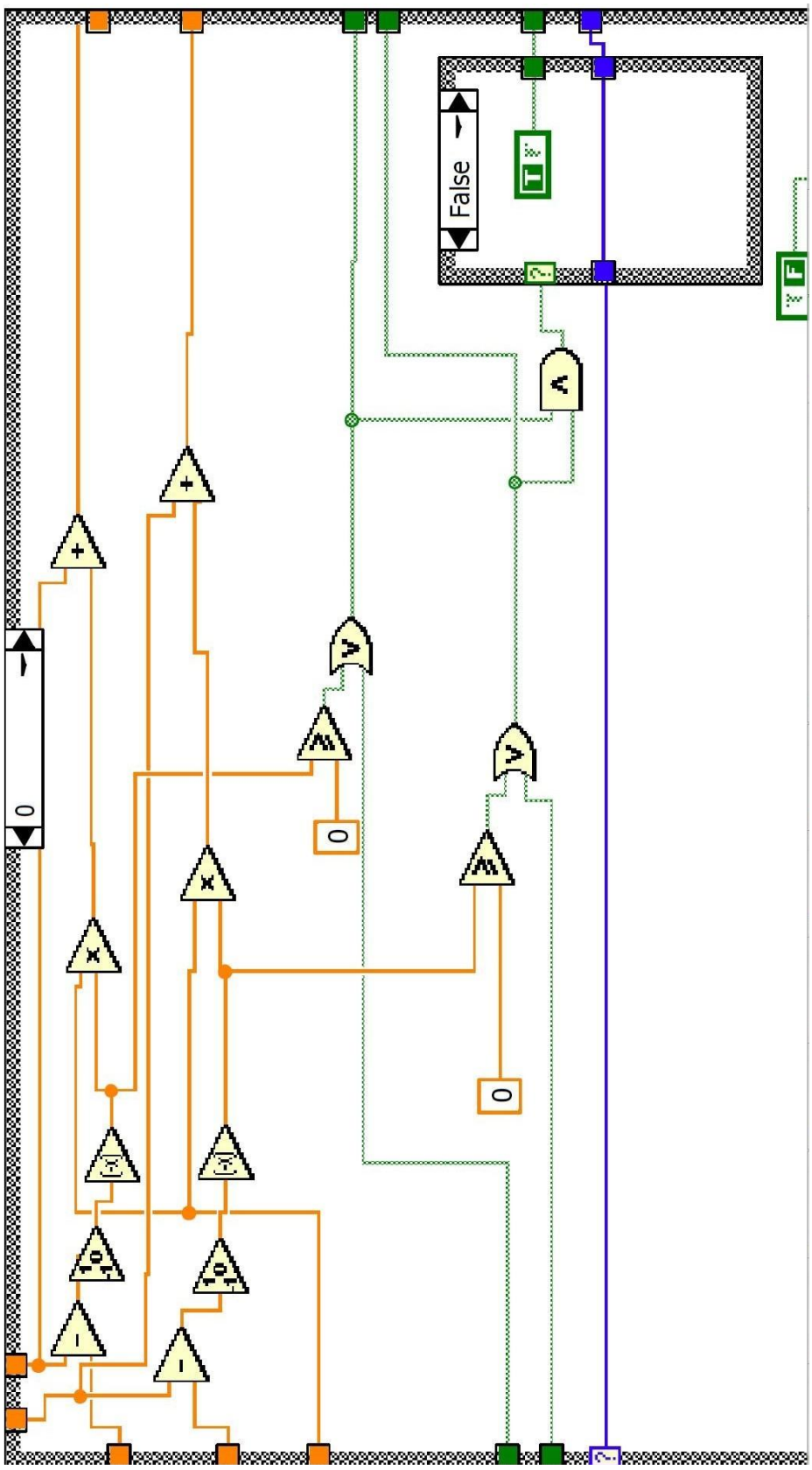
False
T
F
i
0
+
+
<
<
<
x
x
0
0
-1
0
1
1

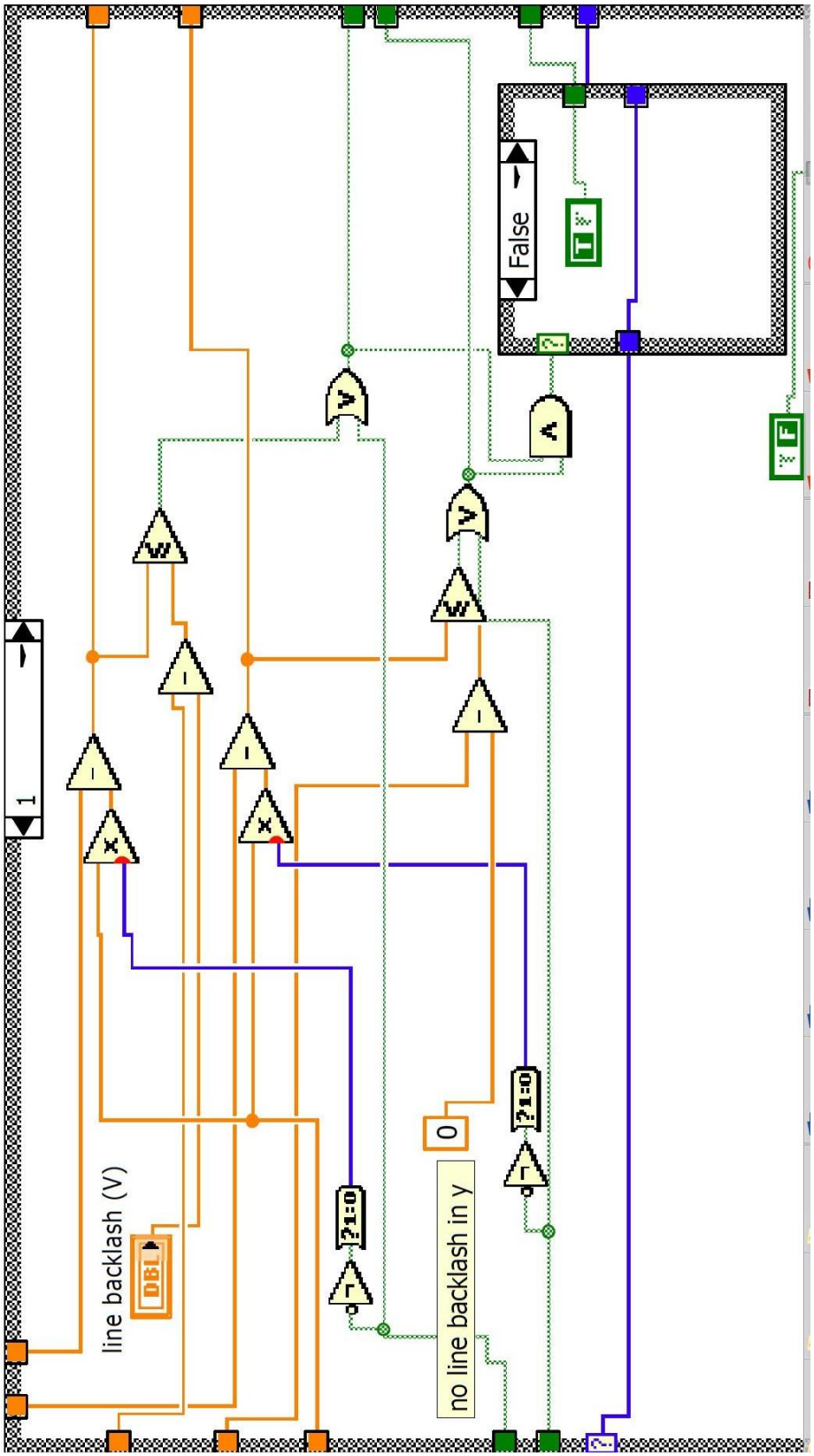
False
line backlash (V)
DBL
no line backlash in y
0
?1:0
?1:0
1

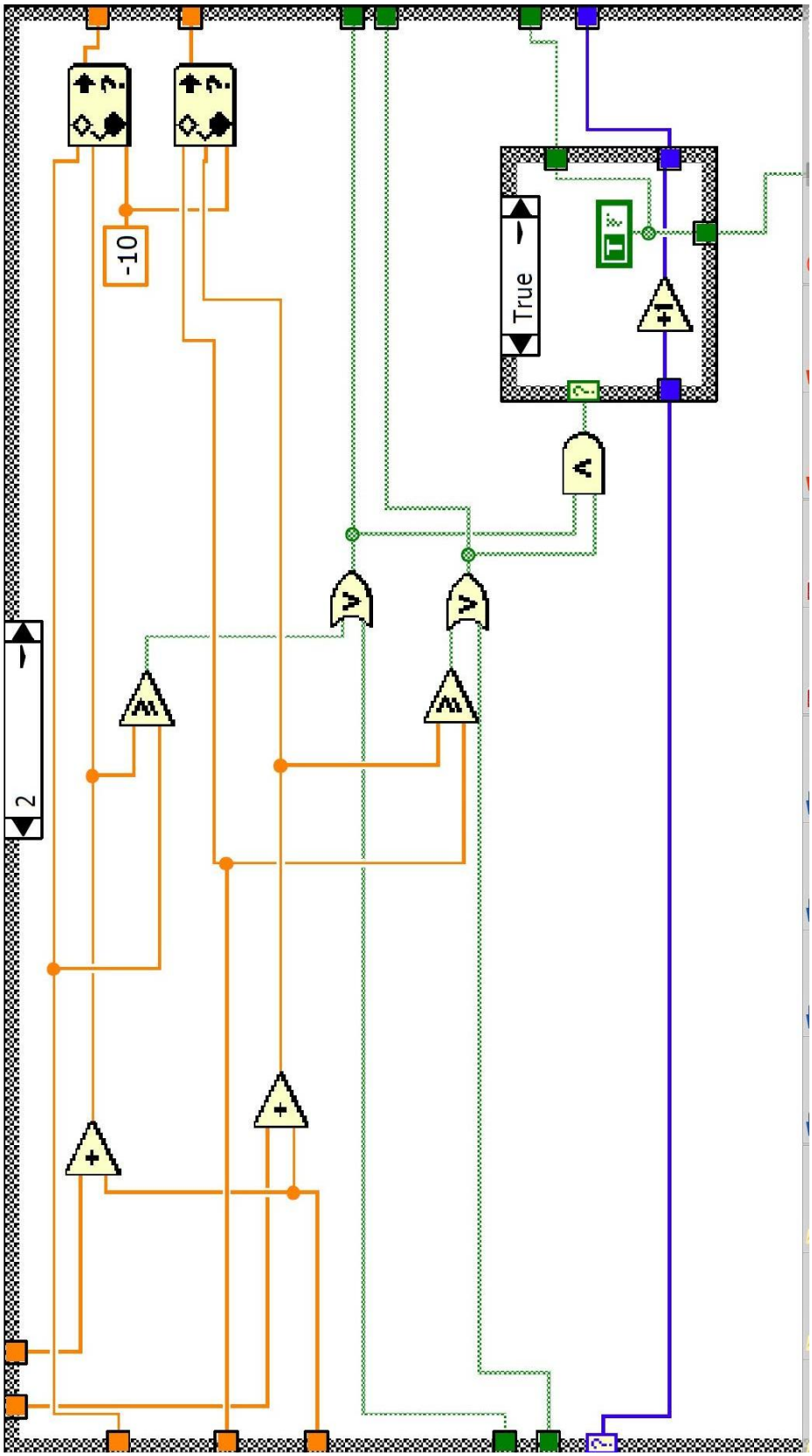
-10
True
2

3 [0..3]
applied signals:
Vbias
x
y
z
0
0
0
-10
z speed (V)
[return tip to substrate

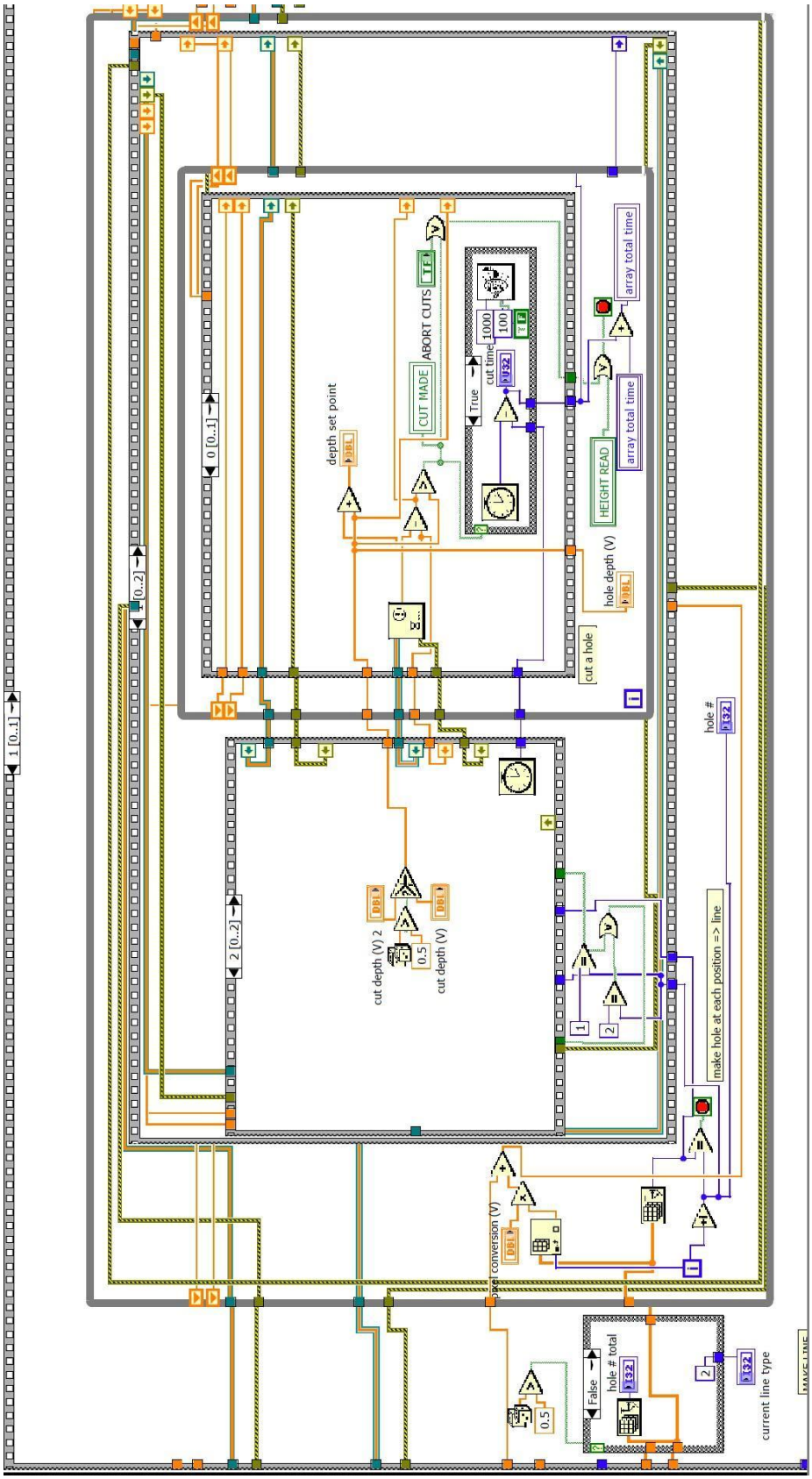
1 [0..1]
0 [0..1]
1 [0..2]
2 [0..2]
depth set point
CUT MADE
ABORT CUTS
TF
cut time
1000
100
True
HEIGHT READ
array total time
hole depth (V)
cut a hole
hole #
cut depth (V) 2
0.5
cut depth (V)
make hole at each position => line
depth conversion (V)
False
hole # total
current line type

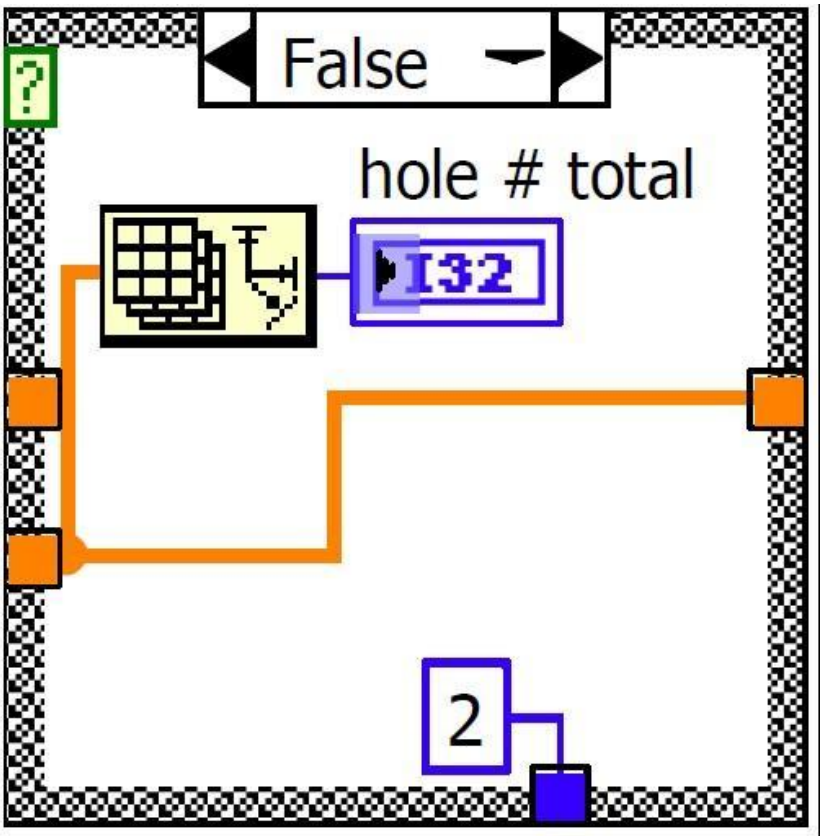
False
hole # total
I32
2

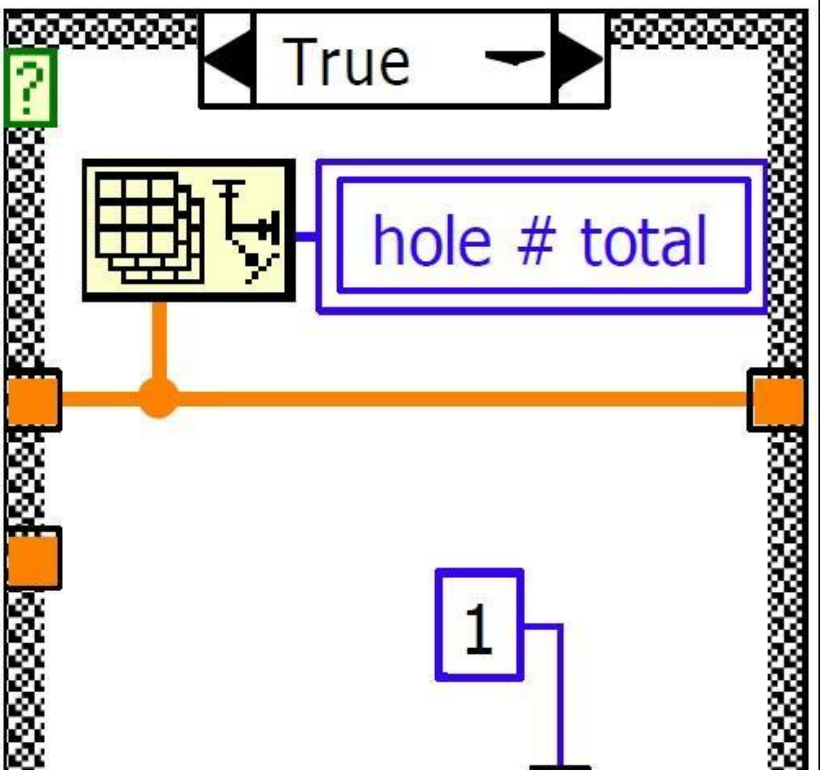
True
hole # total
1

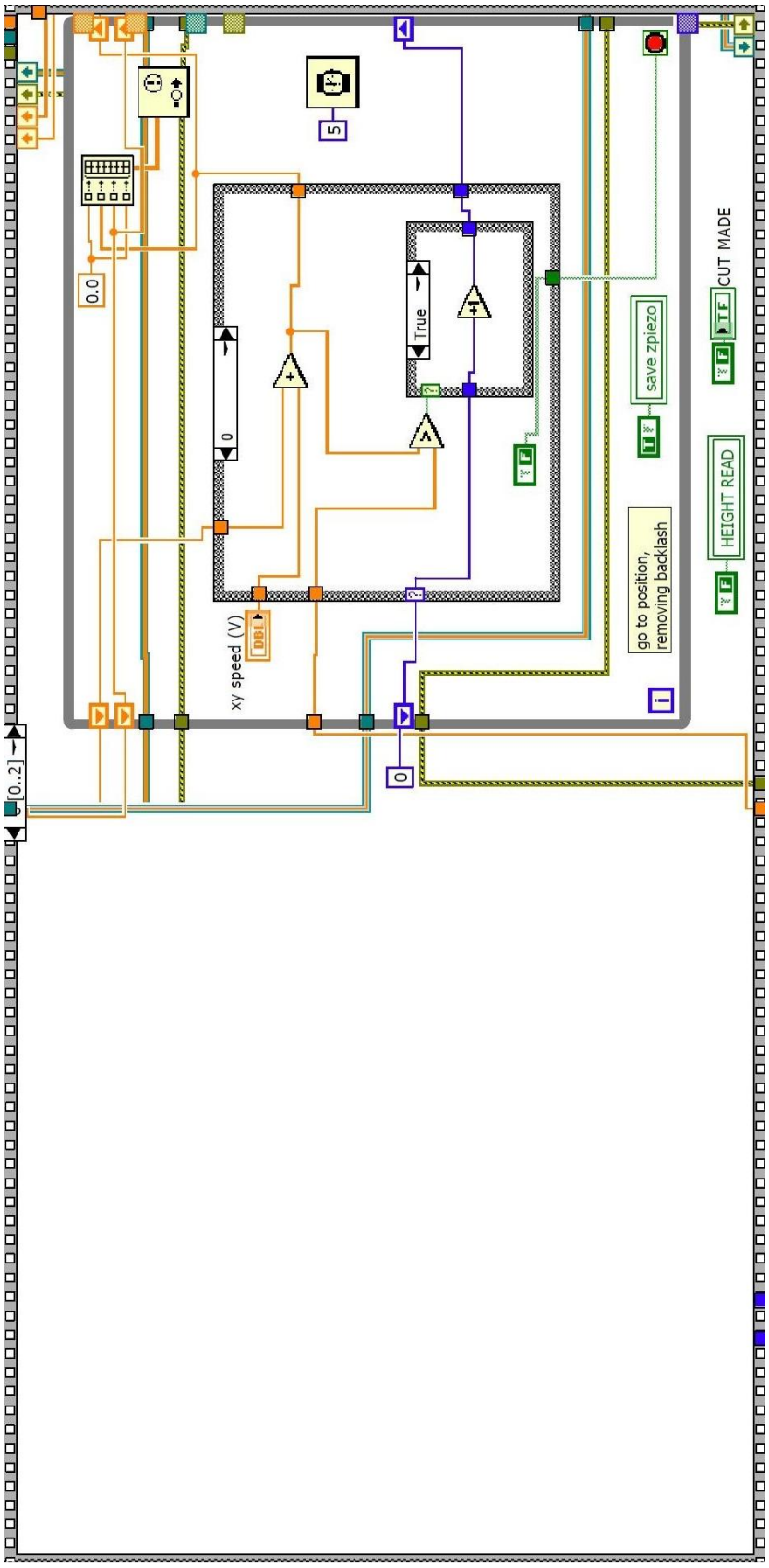
5
0.0
True
0
xy speed (V)
DBL
go to position, removing backlash
save zpiezo
CUT MADE
HEIGHT READ
[0..2]
0

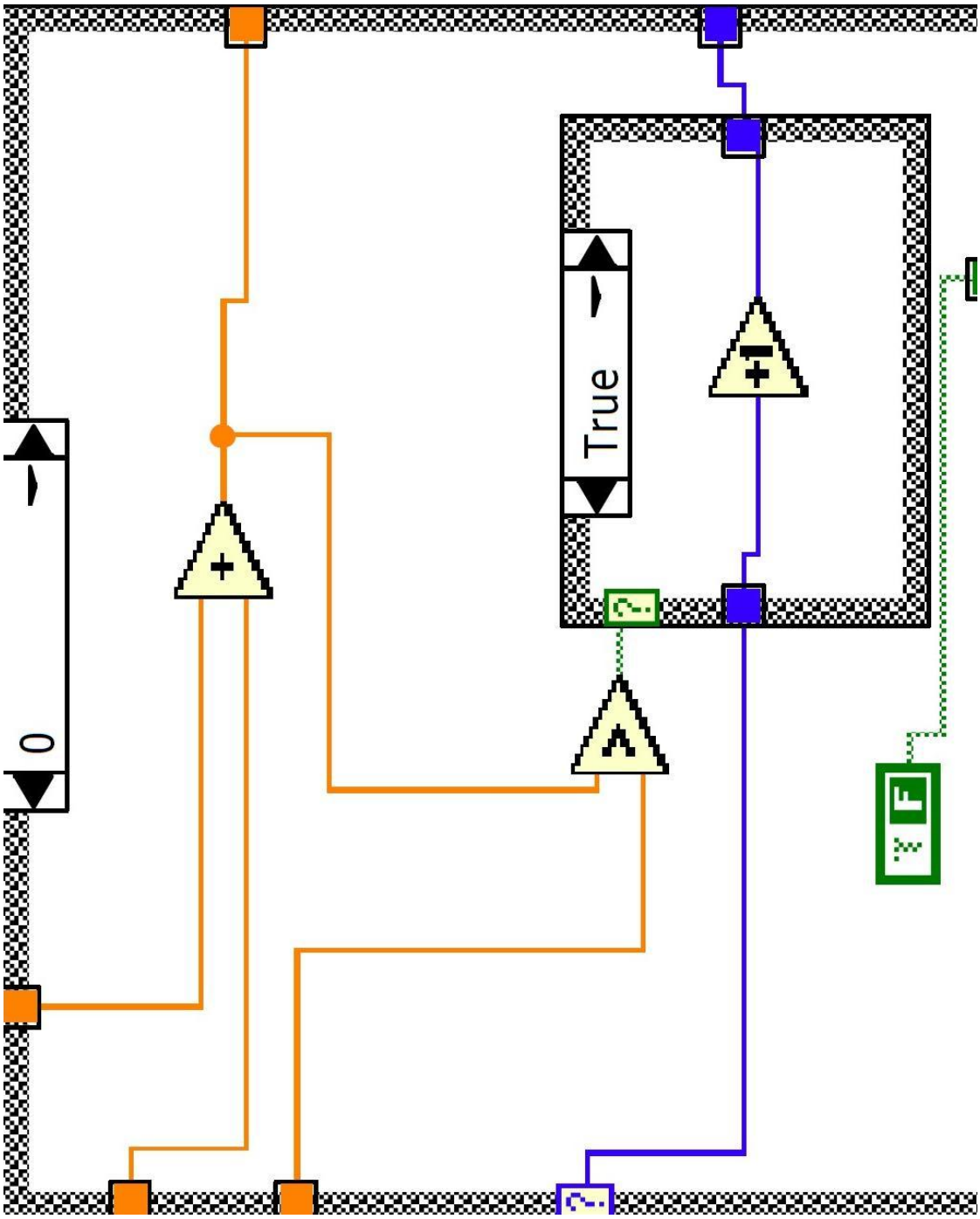
True
0
F

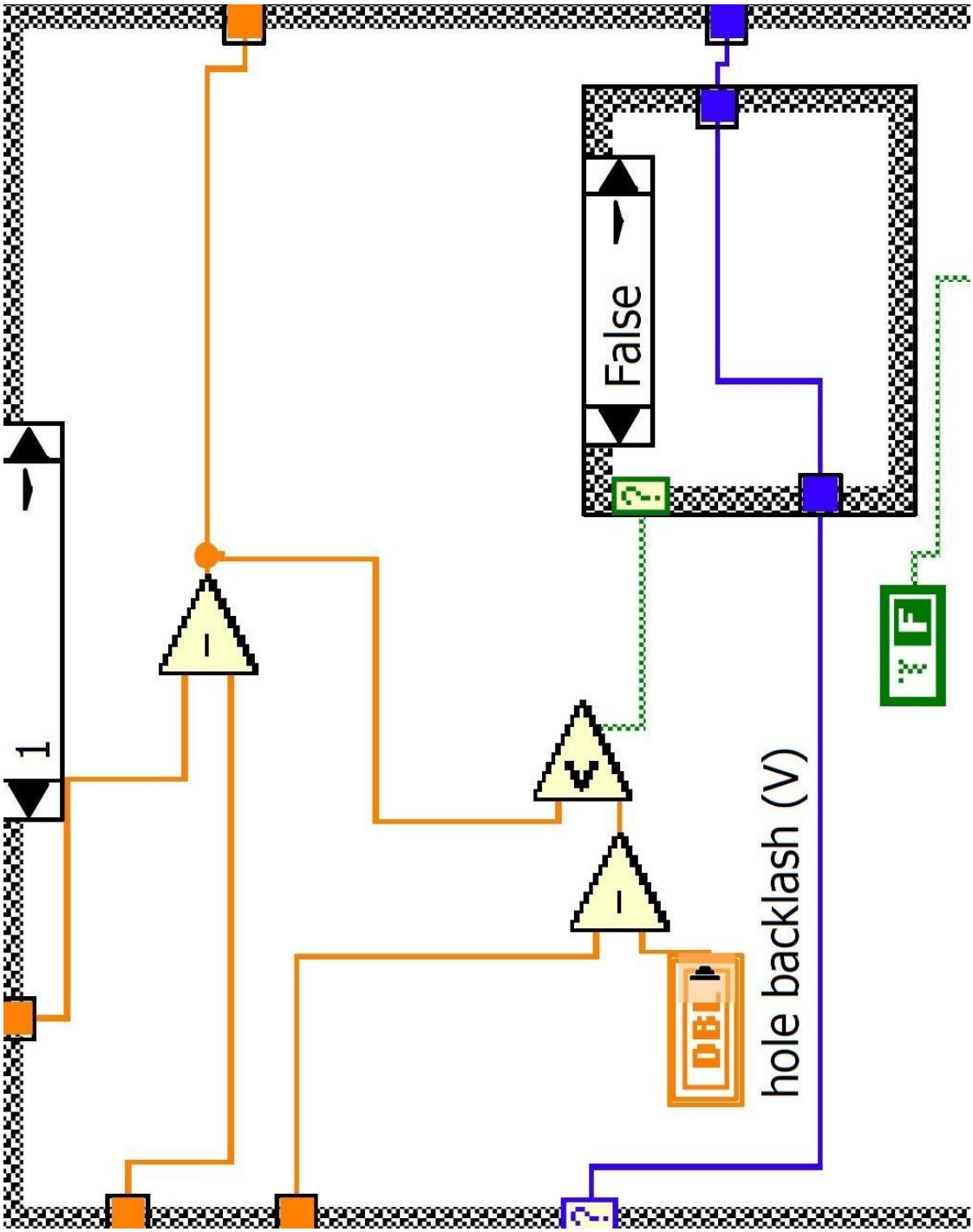
False
1
hole backlash (V)
DBL

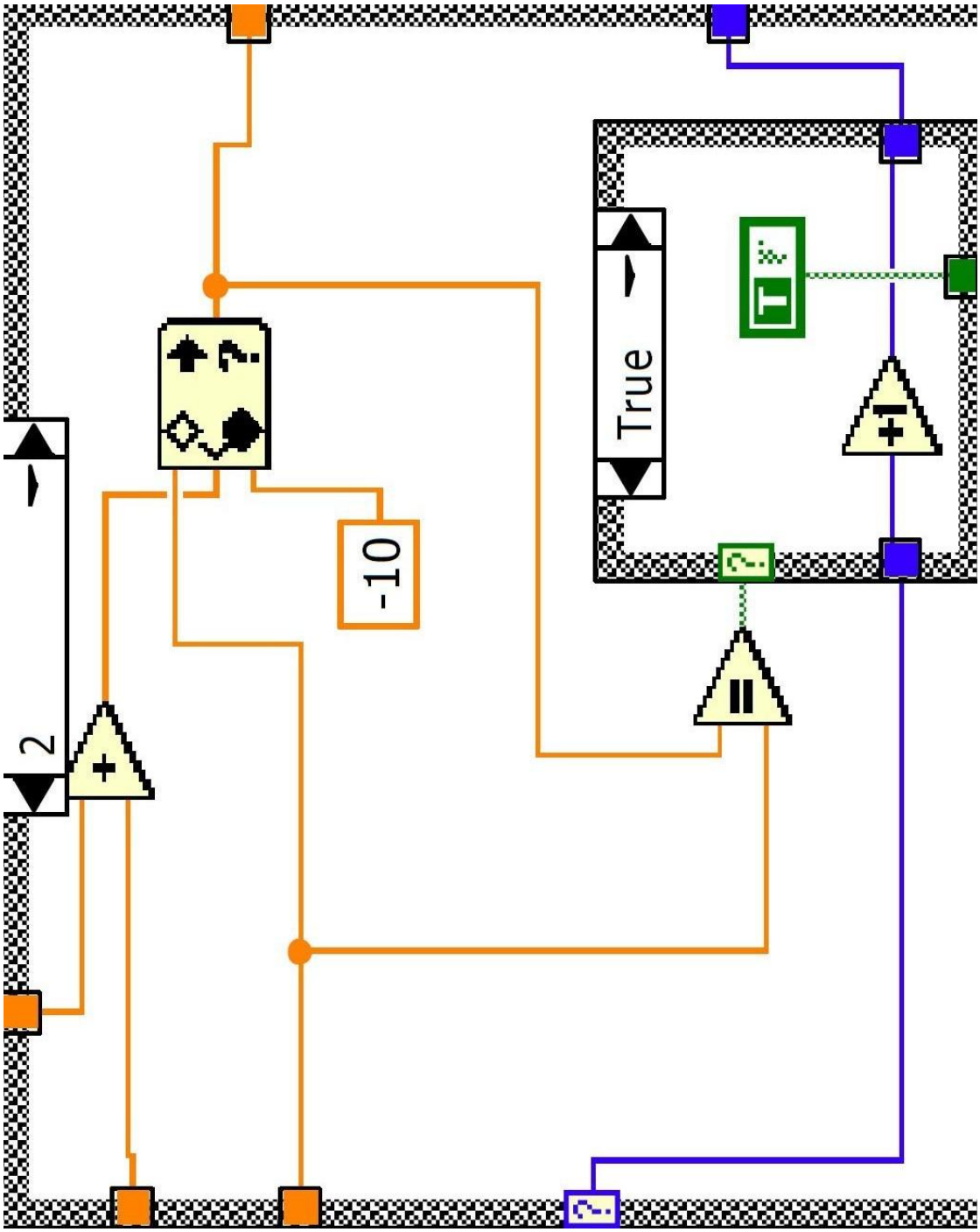
True
-10
2

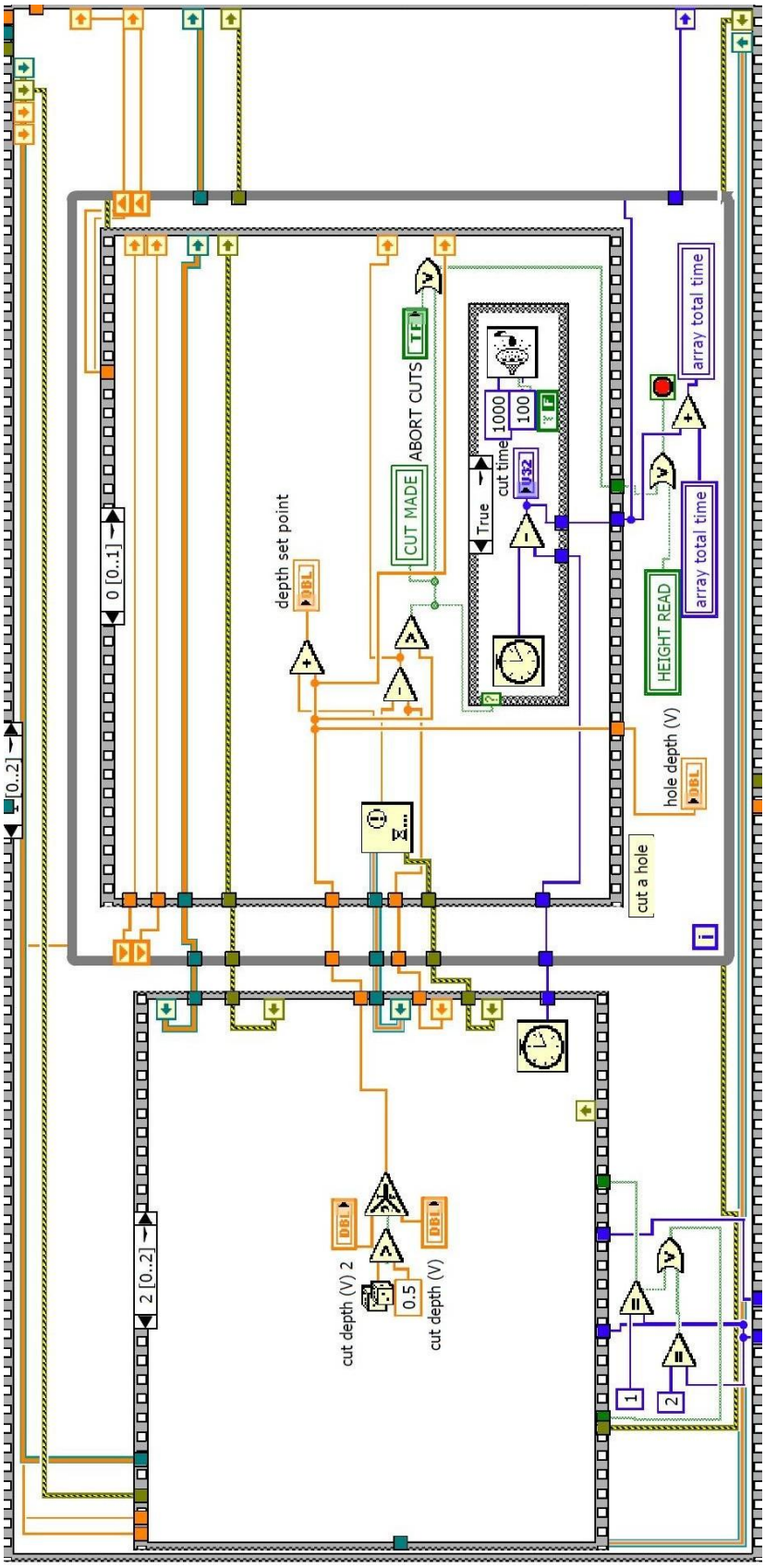
0 [0..1]
depth set point
CUT MADE
ABORT CUTS
TF
True
cut time
1000
100
I32
array total time
array total time
HEIGHT READ
hole depth (V)
cut a hole
i
1 [0..2]
2 [0..2]
cut depth (V) 2
0.5
cut depth (V)
1
2

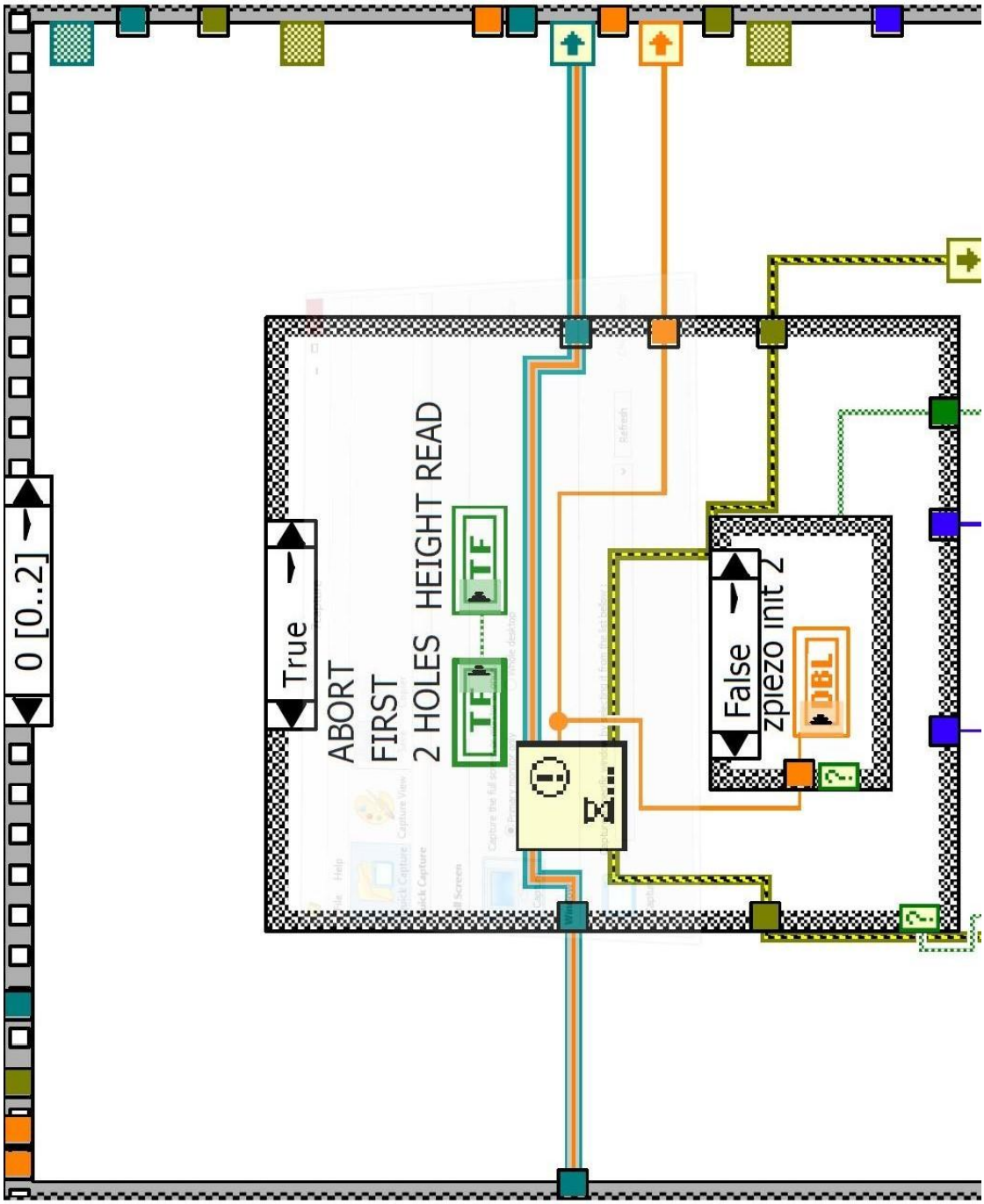
0 [0..2]
True
ABORT
FIRST
2 HOLES
HEIGHT READ
TF
TF
False
zpiezo init 2
DBL

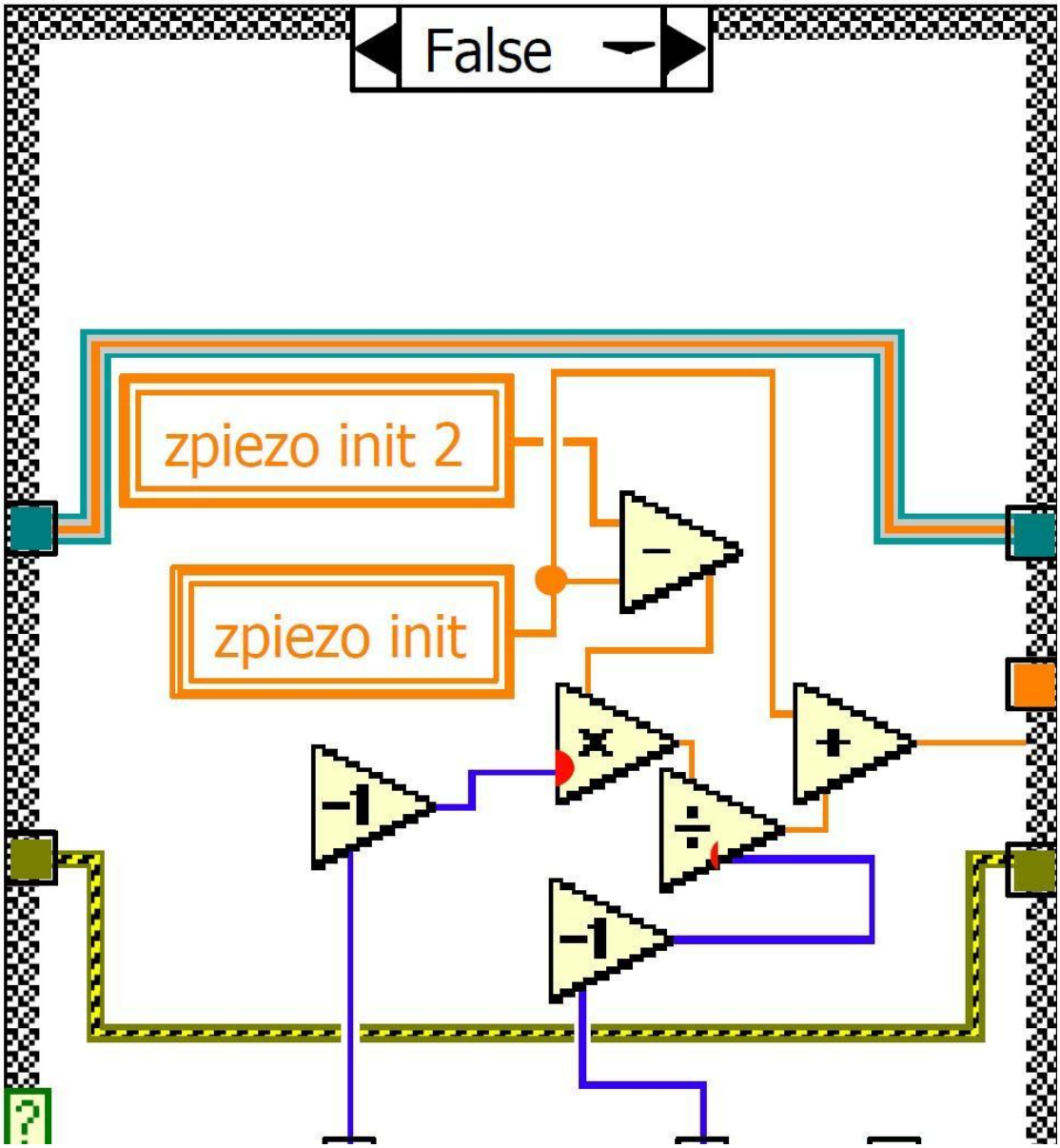
False
zpiezo init 2
zpiezo init
-1
-1

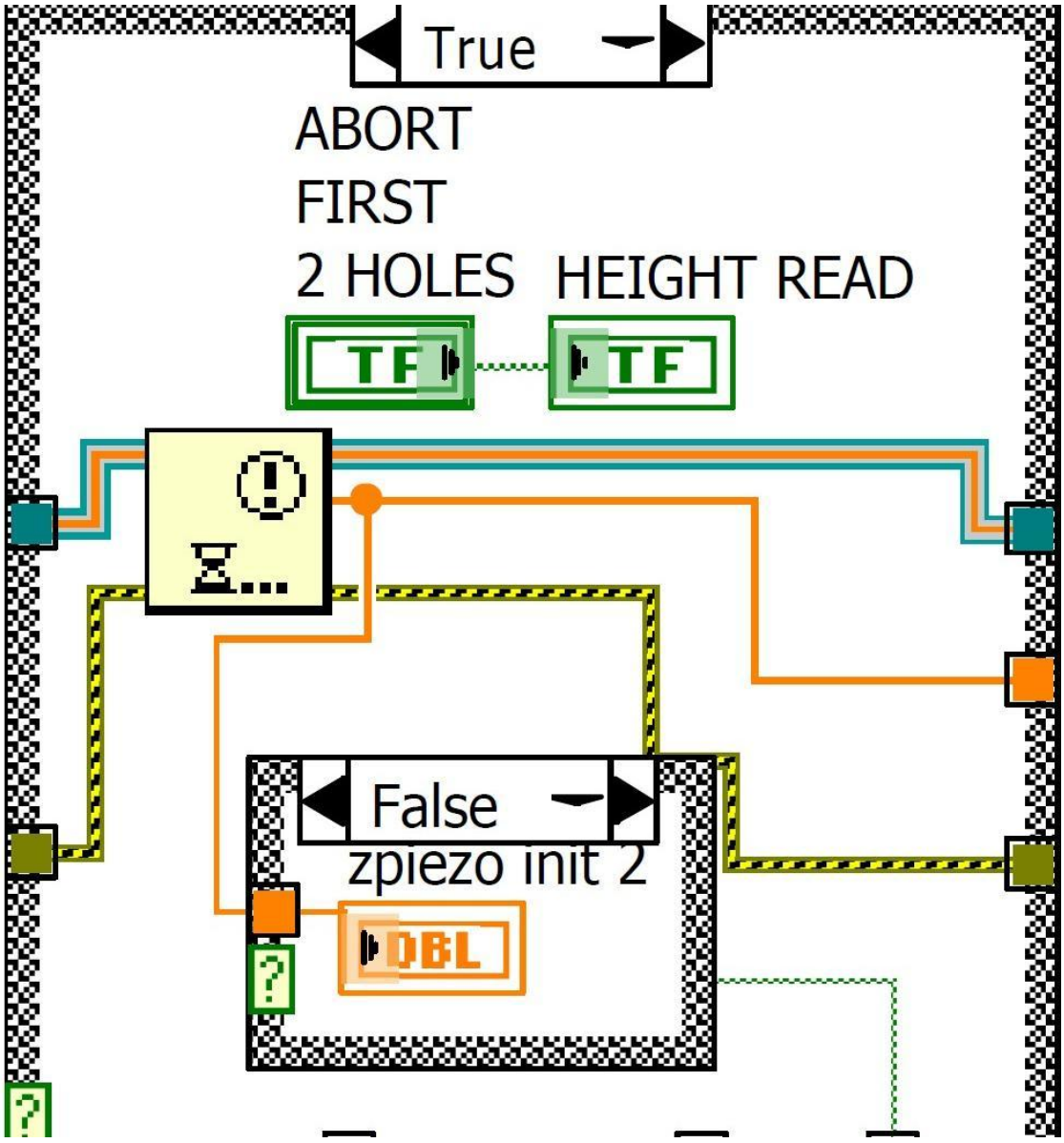
True
ABORT
FIRST
2 HOLES HEIGHT READ
TF
TF
False
zpiezo init 2
DBL

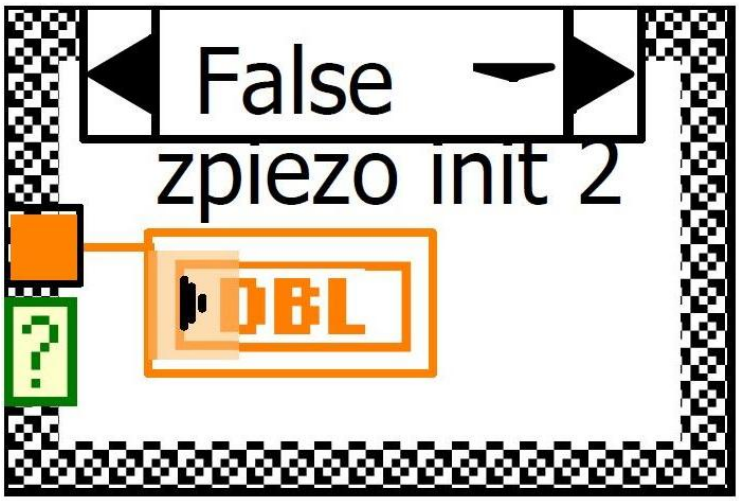
False
zpiezo init 2
DBL
?

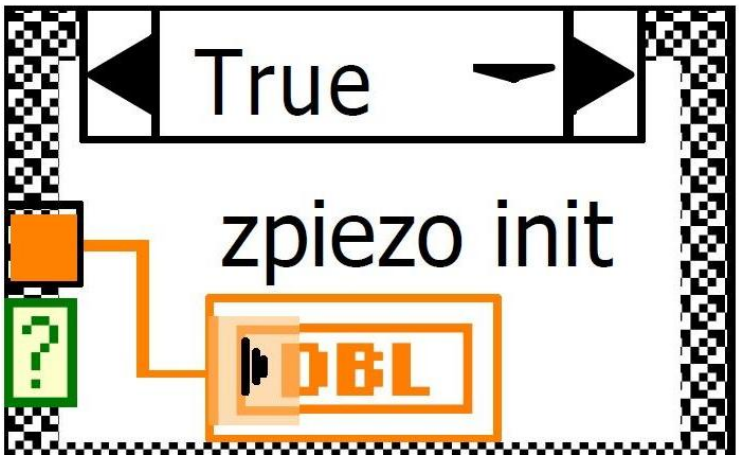
True
zpiezo init
DBL
?

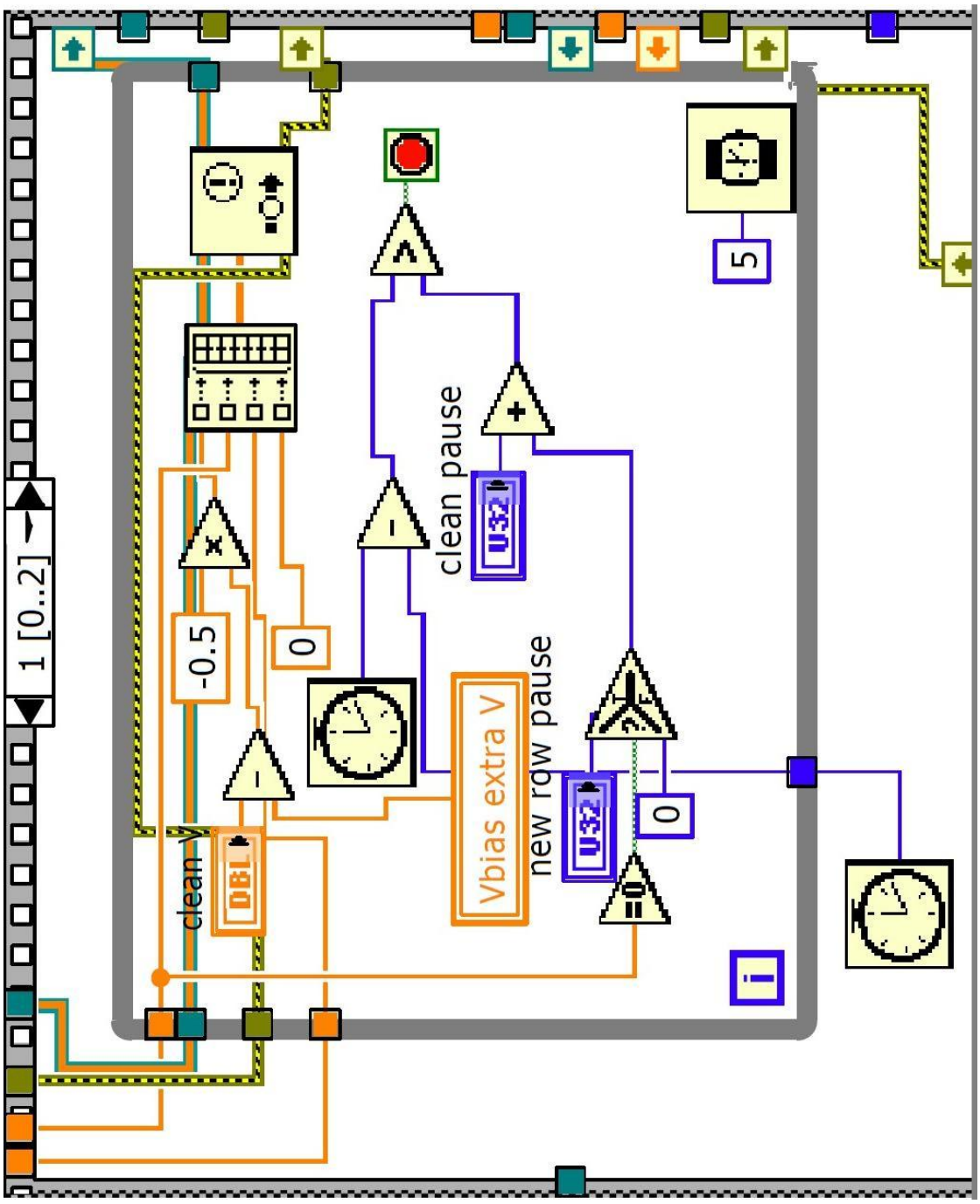
1 [0..2]
-0.5
0
clean V
DBL
clean pause
U32
Vbias extra V
new row pause
U32
0
5
i

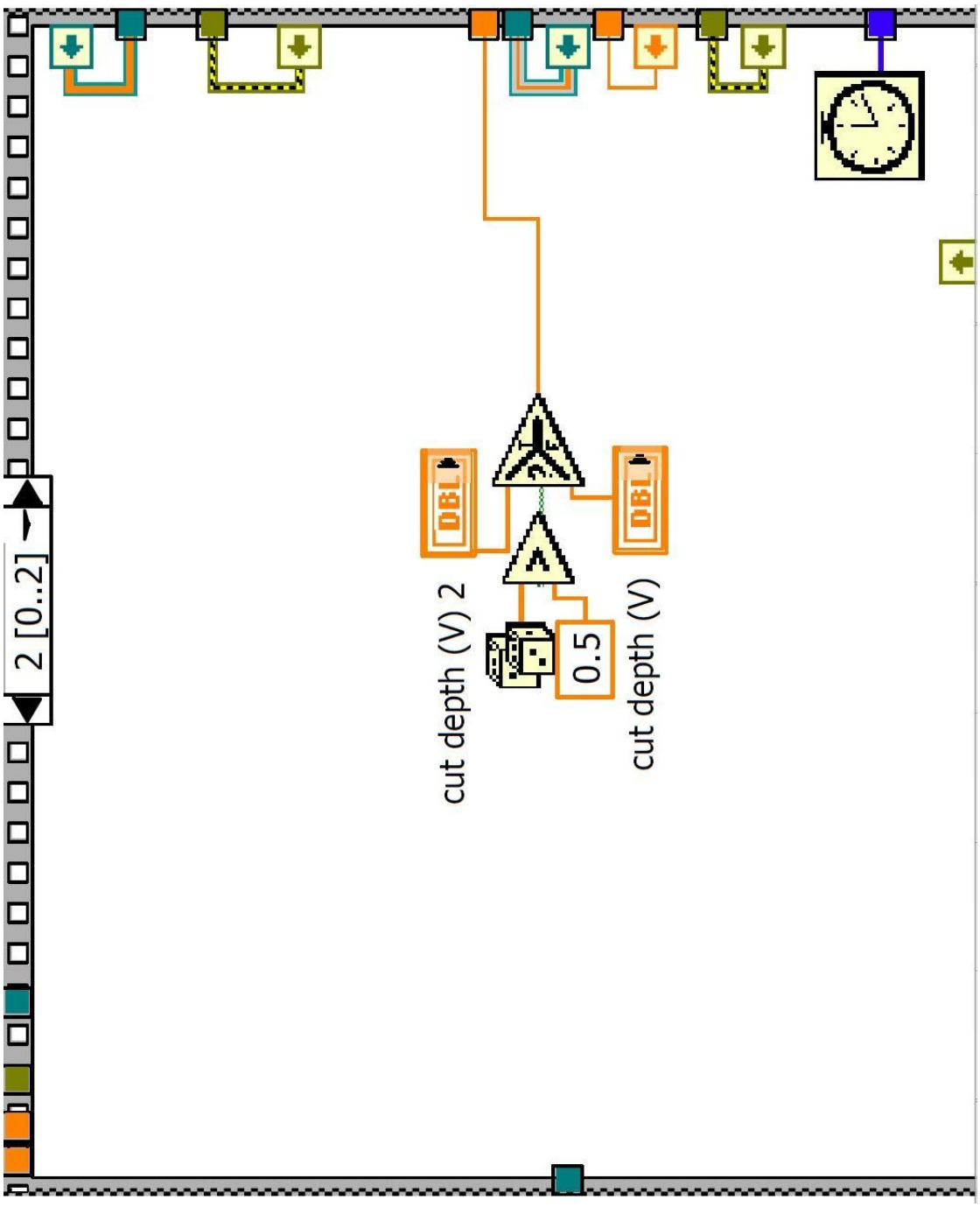
2 [0..2]
DBL
DBL
cut depth (V) 2
0.5
cut depth (V)

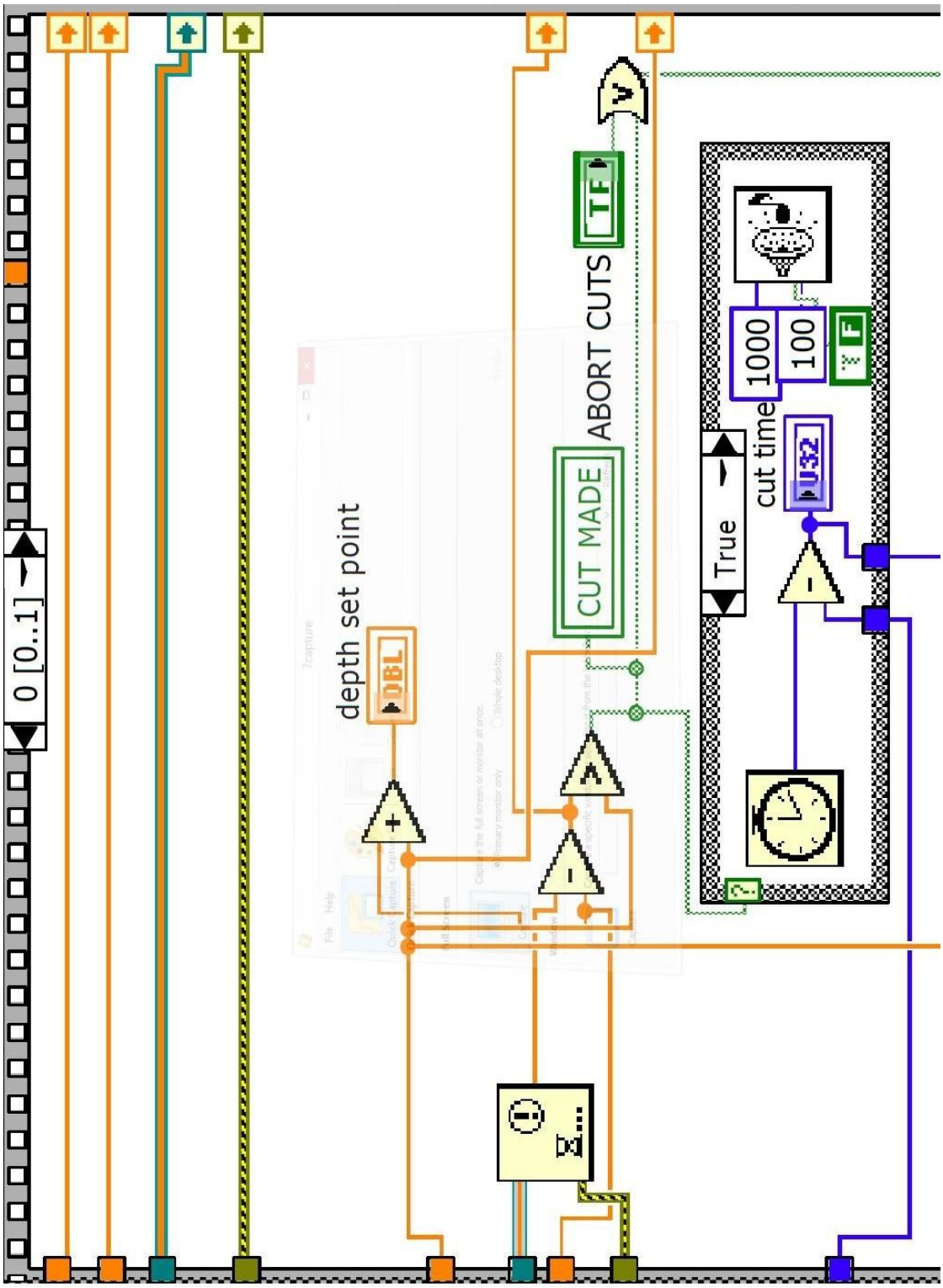
0 [0..1]
depth set point
DBL
CUT MADE
ABORT CUTS
TF
True
cut time
U32
1000
100
I16

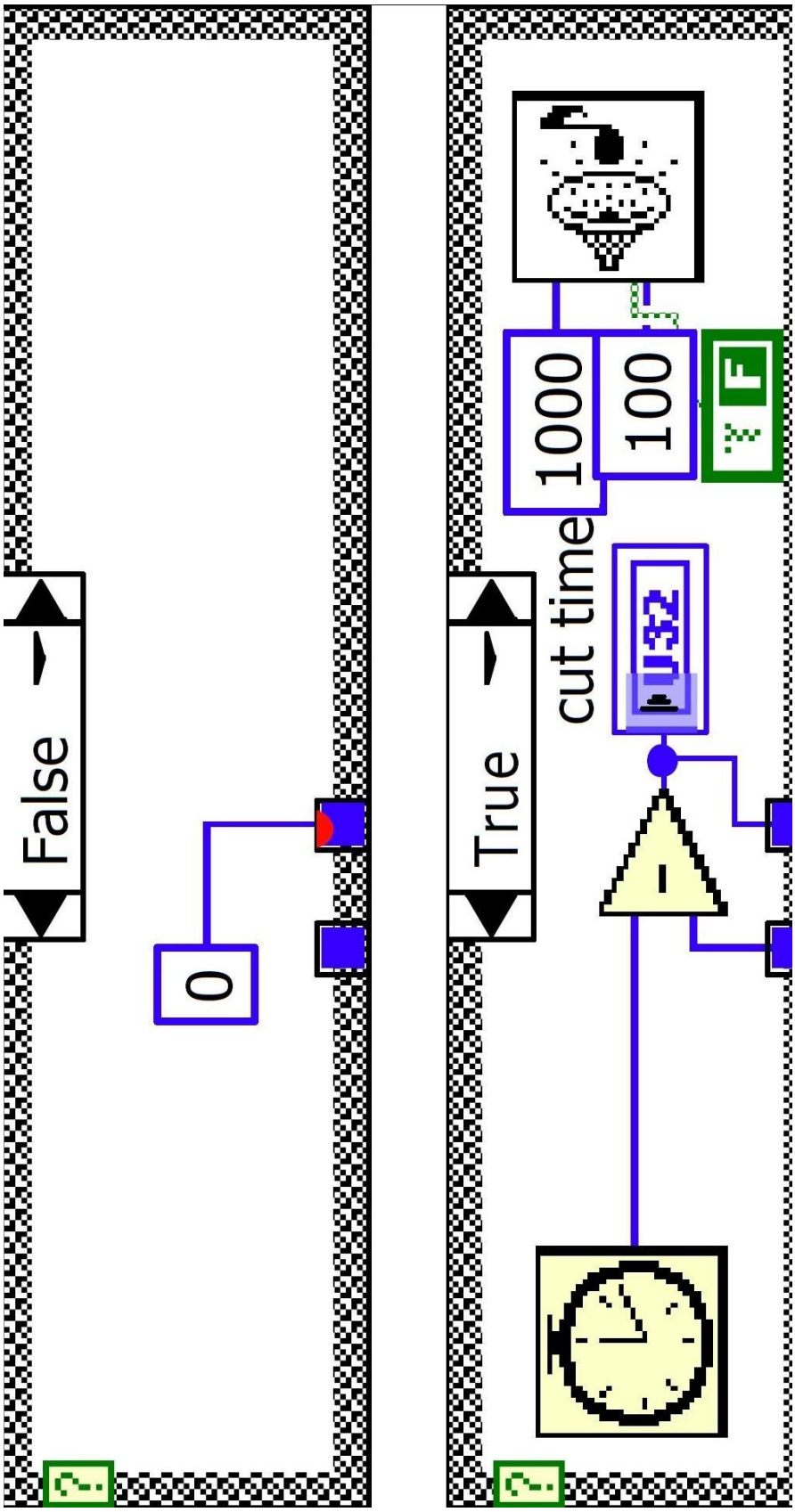
False
0
True
cut time
1000
100
F
U32
1

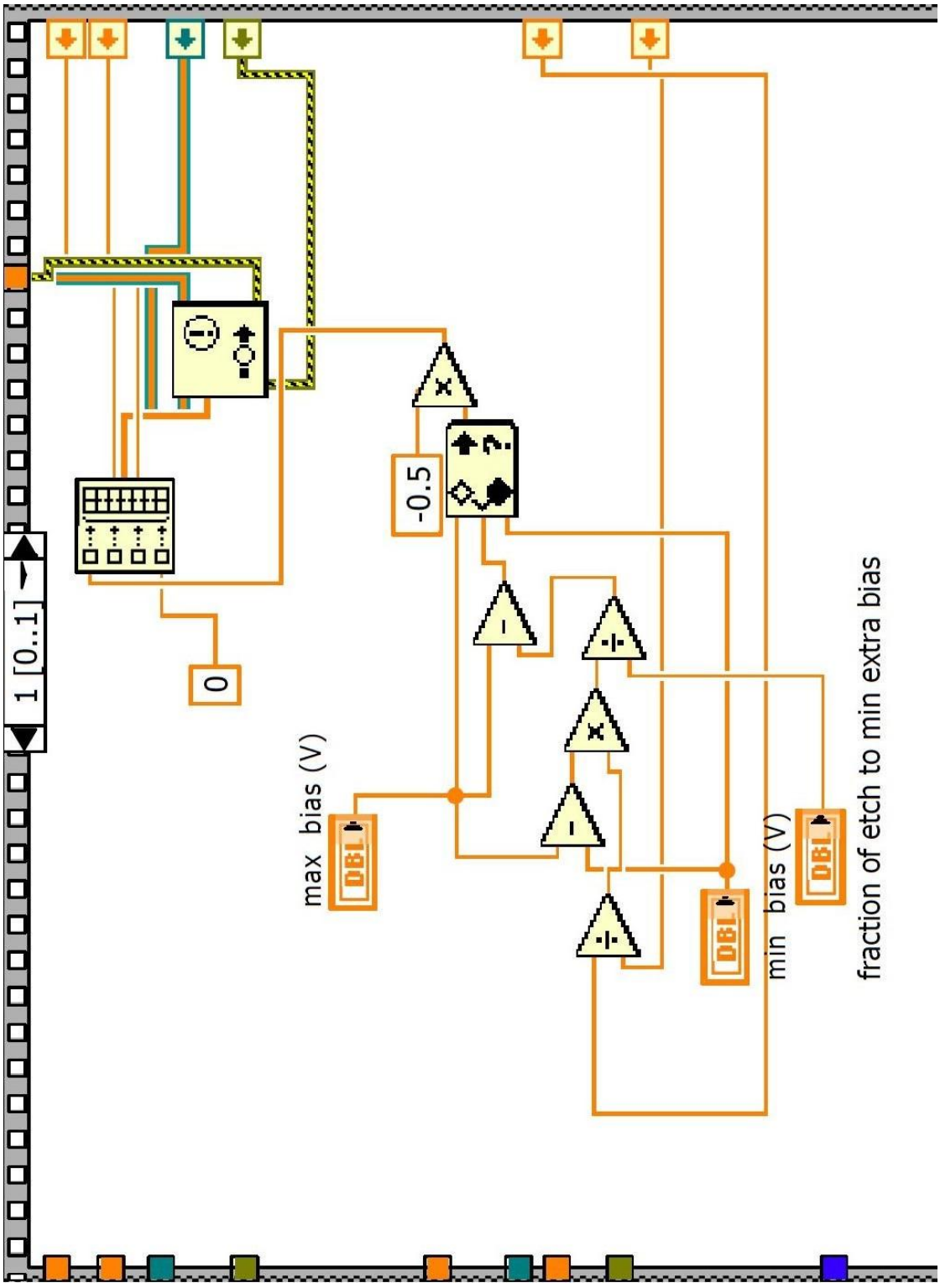
1 [0..1]
0
-0.5
max bias (V)
min bias (V)
fraction of etch to min extra bias
DBL
DBL
DBL

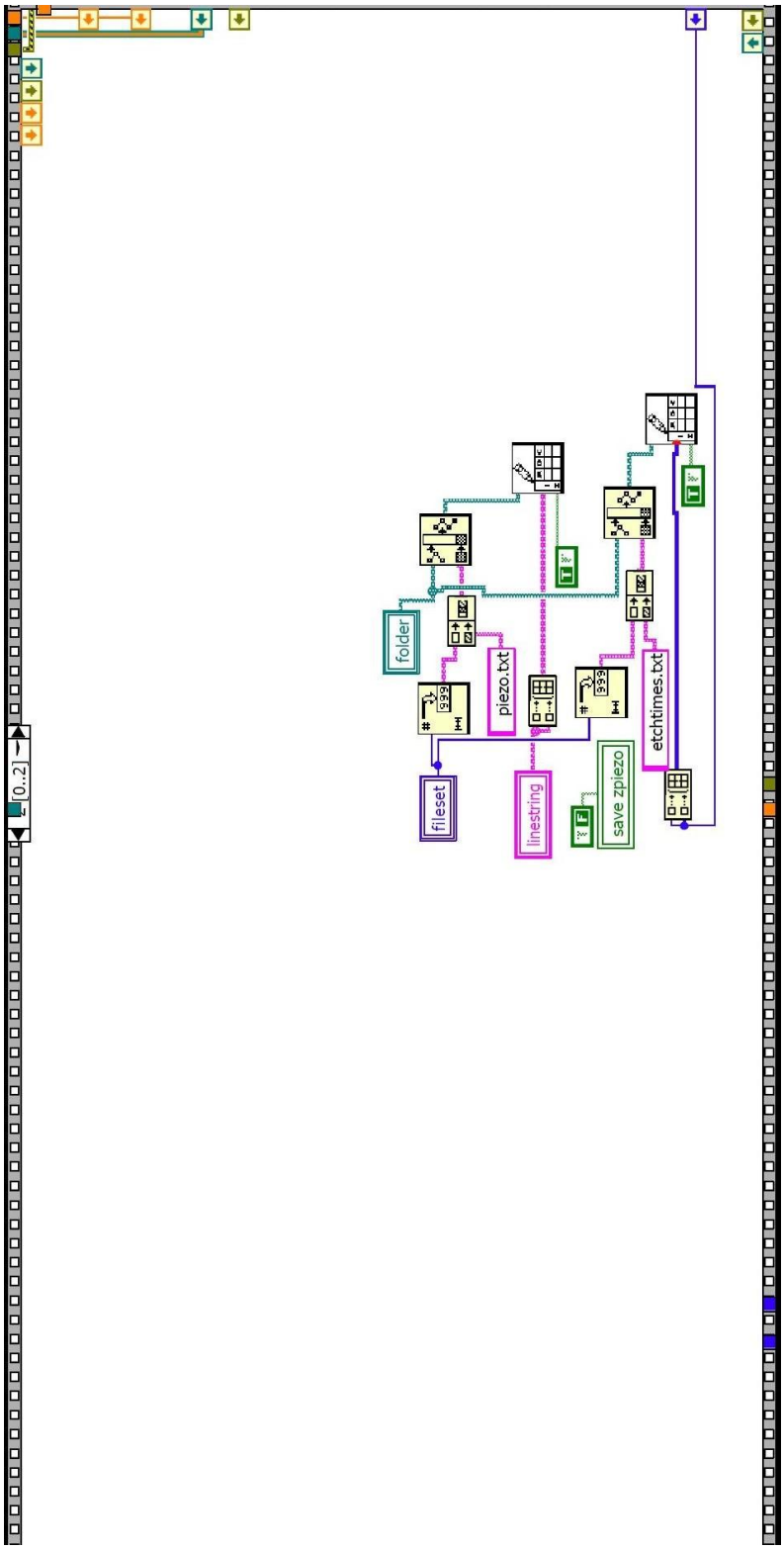
0..2
folder
piezo.txt
etchtimes.txt
fileset
linestring
save zpiezo

A6. MATLAB CODES

A. PIXEL IMAGING AND CROSS-CORRALATION CALCULATIONS

I. DFT REGISTRATION

```
function [output Greg] = dftregistration(buf1ft,buf2ft,usfac)
% function [output Greg] = dftregistration(buf1ft,buf2ft,usfac);
% Efficient subpixel image registration by crosscorrelation. This code
% gives the same precision as the FFT upsampled cross correlation in a
% small fraction of the computation time and with reduced memory
% requirements. It obtains an initial estimate of the crosscorrelation peak
% by an FFT and then refines the shift estimation by upsampling the DFT
% only in a small neighborhood of that estimate by means of a
% matrix-multiply DFT. With this procedure all the image points are used to
% compute the upsampled crosscorrelation.
% Manuel Guizar - Dec 13, 2007

% Portions of this code were taken from code written by Ann M. Kowalczyk
% and James R. Fienup.
% J.R. Fienup and A.M. Kowalczyk, "Phase retrieval for a complex-valued
% object by using a low-resolution image," J. Opt. Soc. Am. A 7, 450-458
% (1990).
% Citation for this algorithm:
% Manuel Guizar-Sicairos, Samuel T. Thurman, and James R. Fienup,
% "Efficient subpixel image registration algorithms," Opt. Lett. 33,
% 156-158 (2008).

% Inputs
% buf1ft    Fourier transform of reference image,
%           DC in (1,1)   [DO NOT FFTSHIFT]
% buf2ft    Fourier transform of image to register,
%           DC in (1,1) [DO NOT FFTSHIFT]
% usfac     Upsampling factor (integer). Images will be registered to
%           within 1/usfac of a pixel. For example usfac = 20 means the
%           images will be registered within 1/20 of a pixel. (default = 1)

% Outputs
% output =  [error,diffphase,net_row_shift,net_col_shift]
% error     Translation invariant normalized RMS error between f and g
% diffphase     Global phase difference between the two images (should be
%           zero if images are non-negative).
% net_row_shift net_col_shift     Pixel shifts between images
% Greg      (Optional) Fourier transform of registered version of buf2ft,
%           the global phase difference is compensated for.

% Default usfac to 1
if exist('usfac')~=1, usfac=1; end

% Compute error for no pixel shift
if usfac == 0,
   CCmax = sum(sum(buf1ft.*conj(buf2ft)));
   rfzero = sum(abs(buf1ft(:)).^2);
   rgzero = sum(abs(buf2ft(:)).^2);
   error = 1.0 - CCmax.*conj(CCmax)/(rgzero*rfzero);
   error = sqrt(abs(error));
   diffphase=atan2(imag(CCmax),real(CCmax));
   output=[error,diffphase];
% Whole-pixel shift - Compute crosscorrelation by an IFFT and locate the
% peak
elseif usfac == 1,
   [m,n]=size(buf1ft);
   CC = ifft2(buf1ft.*conj(buf2ft));
   [max1,loc1] = max(CC);
   [max2,loc2] = max(max1);
   rloc=loc1(loc2);
   cloc=loc2;
   CCmax=CC(rloc,cloc);
   rfzero = sum(abs(buf1ft(:)).^2)/(m*n);
   rgzero = sum(abs(buf2ft(:)).^2)/(m*n);
   error = 1.0 - CCmax.*conj(CCmax)/(rgzero(1,1)*rfzero(1,1));
   error = sqrt(abs(error));
   diffphase=atan2(imag(CCmax),real(CCmax));
   md2 = fix(m/2);
   nd2 = fix(n/2);
   if rloc > md2
```

```
    row_shift = rloc - m - 1;
  else
    row_shift = rloc - 1;
  end

  if cloc > nd2
    col_shift = cloc - n - 1;
  else
    col_shift = cloc - 1;
  end
  output=[error,diffphase,row_shift,col_shift];

% Partial-pixel shift
else
  % First upsample by a factor of 2 to obtain initial estimate
  % Embed Fourier data in a 2x larger array
  [m,n]=size(buf1ft);
  mlarge=m*2;
  nlarge=n*2;
  CC=zeros(mlarge,nlarge);
  CC(m+1-fix(m/2):m+1+fix((m-1)/2),n+1-fix(n/2):n+1+fix((n-1)/2)) = ...
    fftshift(buf1ft).*conj(fftshift(buf2ft));
  % Compute crosscorrelation and locate the peak
  CC = ifft2(ifftshift(CC)); % Calculate cross-correlation
  [max1,loc1] = max(CC);
  [max2,loc2] = max(max1);
  rloc=loc1(loc2);cloc=loc2;
  CCmax=CC(rloc,cloc);
  % Obtain shift in original pixel grid from the position of the
  % crosscorrelation peak
  [m,n] = size(CC); md2 = fix(m/2); nd2 = fix(n/2);
  if rloc > md2
    row_shift = rloc - m - 1;
  else
    row_shift = rloc - 1;
  end
  if cloc > nd2
    col_shift = cloc - n - 1;
  else
    col_shift = cloc - 1;
  end
  row_shift=row_shift/2;
  col_shift=col_shift/2;
  % If upsampling > 2, then refine estimate with matrix multiply DFT
  if usfac > 2,
    %%% DFT computation %%%
    % Initial shift estimate in upsampled grid
    row_shift = round(row_shift*usfac)/usfac;
    col_shift = round(col_shift*usfac)/usfac;
    dftshift = fix(ceil(usfac*1.5)/2); %% Center of output array at dftshift+1
    % Matrix multiply DFT around the current shift estimate
    CC = conj(dftups(buf2ft.*conj(buf1ft),ceil(usfac*1.5),ceil(usfac*1.5),usfac,...
      dftshift-row_shift*usfac,dftshift-col_shift*usfac))/(md2*nd2*usfac^2);
    % Locate maximum and map back to original pixel grid
    [max1,loc1] = max(CC);
    [max2,loc2] = max(max1);
    rloc = loc1(loc2); cloc = loc2;
    CCmax = CC(rloc,cloc);
    rg00 = dftups(buf1ft.*conj(buf1ft),1,1,usfac)/(md2*nd2*usfac^2);
    rf00 = dftups(buf2ft.*conj(buf2ft),1,1,usfac)/(md2*nd2*usfac^2);
    rloc = rloc - dftshift - 1;
    cloc = cloc - dftshift - 1;
    row_shift = row_shift + rloc/usfac;
    col_shift = col_shift + cloc/usfac;
  % If upsampling = 2, no additional pixel shift refinement
  else
    rg00 = sum(sum( buf1ft.*conj(buf1ft) ))/m/n;
    rf00 = sum(sum( buf2ft.*conj(buf2ft) ))/m/n;
  end
  error = 1.0 - CCmax.*conj(CCmax)/(rg00*rf00);
  error = sqrt(abs(error));
  diffphase=atan2(imag(CCmax),real(CCmax));
  % If its only one row or column the shift along that dimension has no
  % effect. We set to zero.
  if md2 == 1,
    row_shift = 0;
  end
  if nd2 == 1,
    col_shift = 0;
  end
  output=[error,diffphase,row_shift,col_shift];
end

% Compute registered version of buf2ft
if (nargout > 1)&&(usfac > 0),
  [nr,nc]=size(buf2ft);
  Nr = ifftshift([-fix(nr/2):ceil(nr/2)-1]);
  Nc = ifftshift([-fix(nc/2):ceil(nc/2)-1]);
  [Nc,Nr] = meshgrid(Nc,Nr);
  Greg = buf2ft.*exp(i*2*pi*(-row_shift*Nr/nr-col_shift*Nc/nc));
  Greg = Greg*exp(i*diffphase);
elseif (nargout > 1)&&(usfac == 0)
  Greg = buf2ft*exp(i*diffphase);
end
return

function out=dftups(in,nor,noc,usfac,roff,coff)
```

```
% function out=dftups(in,nor,noc,usfac,roff,coff);
% Upsampled DFT by matrix multiplies, can compute an upsampled DFT in just
% a small region.
% usfac         Upsampling factor (default usfac = 1)
% [nor,noc]     Number of pixels in the output upsampled DFT, in
%               units of upsampled pixels (default = size(in))
% roff, coff    Row and column offsets, allow to shift the output array to
%               a region of interest on the DFT (default = 0)
% Recieves DC in upper left corner, image center must be in (1,1)
% Manuel Guizar - Dec 13, 2007
% Modified from dftus, by J.R. Fienup 7/31/06

% This code is intended to provide the same result as if the following
% operations were performed
%   - Embed the array "in" in an array that is usfac times larger in each
%     dimension. ifftshift to bring the center of the image to (1,1).
%   - Take the FFT of the larger array
%   - Extract an [nor, noc] region of the result. Starting with the
%     [roff+1 coff+1] element.

% It achieves this result by computing the DFT in the output array without
% the need to zeropad. Much faster and memory efficient than the
% zero-padded FFT approach if [nor noc] are much smaller than [nr*usfac nc*usfac]

[nr,nc]=size(in);
% Set defaults
if exist('roff')~=1, roff=0; end
if exist('coff')~=1, coff=0; end
if exist('usfac')~=1, usfac=1; end
if exist('noc')~=1, noc=nc; end
if exist('nor')~=1, nor=nr; end
% Compute kernels and obtain DFT by matrix products
kernc=exp((-i*2*pi/(nc*usfac))*(    ifftshift([0:nc-1]).' - floor(nc/2) )*( [0:noc-1] - coff ));
kernr=exp((-i*2*pi/(nr*usfac))*(          [0:nor-1].' - roff )*( ifftshift([0:nr-1]) - floor(nr/2)  ));
out=kernr*in*kernc;
return
```

II. SNAP AVERAGE

```
% Currently, uses MT9P001-REV8.sdat; use register dialogue in sensor demo
% to find corresponding registers, etc:

% address(decimal)     description
% ----------------     -----------
% 0             chip_version_reg
% 1             row_window_start_reg
% 2             col_window_start_reg
% 3             row_window_size_reg
% 4             col_window_size_reg
% 5             horz_blank_reg
% 6             vert_blank_reg
% 7             control_mode_reg
% 8             shutter_width_hi
% 9             integ_time_reg
% 10            pixel_clock_control
% 11            restart_reg
% 12            shutter_delay_reg
% 13            reset_reg
% 16            pll_control
% 17            pll_config_1
% 18            pll_config_2
% 30            read_mode_1
% 32            read_mode_2
% 34            row_mode
% 35            col_mode
% 43            green1_gain_reg
% 44            blue_gain_reg
% 45            red_gain_reg
% 46            green2_gain_reg
% 53            global_gain_reg   cycles at every 64?
% 73            row_black_target
% 75            row_black_default_offset
% 91            blc_sample_size
% 92            blc_tune1
% 93            blc_thresholds
% 94            blc_tune2
% 95            cal_threshold
% 96            green1_offset
% 97            green2_offset
% 98            cal_ctrl
% 99            red_offset
%100            blue_offset
%106            grn1_channel_off
%107            red_channel_off
%108            blue_channel_off
%109            grn2_channel_off
```

```
%128            shutter_seq_len
%248            chip_enable_reg
%255            chip_version_reg2

reg_globalgain=53;
reg_integ=9;

h = actxserver ('DevWare.ImageSource.1');
h.invoke('WriteRegisterAddr', 0, 0, 32, 0, 80 );
h.invoke('WriteRegisterAddr', 0, 0, 91, 0, 1 );
h.invoke('WriteRegisterAddr', 0, 0, 98, 0, 24578); % RED calibration offset will be used for BLUE; GREEN1 calibrat offset will beuse

%change integration time (register 9) and global gain (register 53); having
%set registe 98 above, global gain will raise RBG gains equally.
%Global gain only goes to 0 to 63, so change integration time as well.

averages=5;
savedimages=[1 1 1];
clear data;  % saves normalized data
clear imagedata;

h.invoke('WriteRegisterAddr',0,0,reg_globalgain,0,63);
pause(1);

% Find a good exposure time

['at max gain, find min integration time']

for a=0:1:

   h.invoke('WriteRegisterAddr',0,0,reg_intetg,0,a);
   pause(0.2);
   i=h.invoke('Get

   if max(max(max(snap)))<255
      expstop=i;
      break;
   end

end

   expthresh=max(max(max(snap)))/2;
   expthresh

for i=0:expstop

   set(src,'Exposure',i);
   pause(0.2);
   snap=getsnapshot(vid);
   snap=double(snap);

   if max(max(max(snap)))>expthresh
      expstart=i;
      break;
   end

end

['expstart is ', num2str(expstart)]
['expstop  is ', num2str(expstop)]

set(src,'Exposure', 255);
set(src,'Exposure', expstart);
pause(1);

for i=expstart:expstop
   i

   set(src,'Exposure',   i);
   pause(0.2);
   images=0;

   for j=1:averages*3

      if images==averages
         break;
      end

      snap=getsnapshot(vid);
      snap=double(snap);

      if ( max(max(max(snap)))<255 ) % && min(min(min(snap)))>0
      images=images+1;

      datamean(1)=mean(mean(snap(:,:,1)));
      datamean(2)=mean(mean(snap(:,:,2)));
      datamean(3)=mean(mean(snap(:,:,3)));
      datastd(1) = std2(snap(:,:,1));
      datastd(2) = std2(snap(:,:,2));
      datastd(3) = std2(snap(:,:,3));

      snap(1:480,1:640,1)=(snap(1:480,1:640,1)-datamean(1))./(datastd(1));
      snap(1:480,1:640,2)=(snap(1:480,1:640,2)-datamean(2))./(datastd(2));
      snap(1:480,1:640,3)=(snap(1:480,1:640,3)-datamean(3))./(datastd(3));

         switch exist('data')
            case 0
               data=snap;
            case 1
               data(:,:,:,size(data,4)+1)=snap;
         end

      end

   end
```

```
savedimages(1)=savedimages(2);
savedimages(2)=savedimages(3);
savedimages(3)=images;

if sum(savedimages)==0
   break;
end

clear eval;
if exist('data')
   %eval([ 'image_i', num2str(i), '_I=mean(data,4);' ]);
   lastimage=i;

   if exist('imagedata')
      imagedata(:,:,:,2)=mean(data,4);
      imagedata=mean(imagedata,4);
   else
      imagedata=mean(data,4);
   end
   end

   clear data;

end
%{
for i=0:lastimage
   for j=1:480
      for k=1:640
         eval(      ['datamean(j,k)=mean(double(data(j,k,',
num2str(1), ',', num2str(1), ':images))'] );
         eval(    ['datastd    (j,k)=    std(double(data(j,k,',
num2str(1), ',', num2str(1), ':images))'] );
      end
   end
end
%}



h.invoke('Quit');
```

III. SNAP AVERAGE APTINA

```
% Currently, uses MT9P001-REV8.sdat; use register
                                    dialogue in sensor demo
% to find corresponding registers, etc:

% address(decimal)     description
% ----------------      -----------
% 0                chip_version_reg
% 1                row_window_start_reg
% 2                col_window_start_reg
% 3                row_window_size_reg
% 4                col_window_size_reg
% 5                horz_blank_reg
% 6                vert_blank_reg
% 7                control_mode_reg
% 8                shutter_width_hi
% 9                integ_time_reg
% 10               pixel_clock_control
% 11               restart_reg
% 12               shutter_delay_reg
% 13               reset_reg
% 16               pll_control
% 17               pll_config_1
% 18               pll_config_2
% 30               read_mode_1
% 32               read_mode_2
% 34               row_mode
% 35               col_mode
% 43               green1_gain_reg
% 44               blue_gain_reg
% 45               red_gain_reg
% 46               green2_gain_reg
% 53               global_gain_reg    cycles at every 64?
% 73               row_black_target
% 75               row_black_default_offset
% 91               blc_sample_size
% 92               blc_tune1
% 93               blc_thresholds
% 94               blc_tune2
% 95               cal_threshold
% 96               green1_offset
% 97               green2_offset
% 98               cal_ctrl
% 99               red_offset
%100               blue_offset
%106               grn1_channel_off
%107               red_channel_off
%108               blue_channel_off
%109               grn2_channel_off
%128               shutter_seq_len
%248               chip_enable_reg
%255               chip_version_reg2

reg_globalgain=53;
reg_integ=9;
```

```
h = actxserver ('DevWare.ImageSource.1');
h.invoke('WriteRegisterAddr', 0, 0, 32, 0, 80 );
h.invoke('WriteRegisterAddr', 0, 0, 91, 0, 1 );
h.invoke('WriteRegisterAddr', 0, 0, 98, 0, 24578); % RED calibration offset will be used for BLUE; GREEN1 calibrat offset will beuse

h.invoke('WriteRegisterAddr',0,0,3,0,958); % set ROI width to 640 pixels
h.invoke('WriteRegisterAddr',0,0,4,0,1278); % set ROI height to 480 pixels

%change integration time (register 9) and global gain (register 53); having
%set registe 98 above, global gain will raise RBG gains equally.
%Global gain only goes to 0 to 63, so change integration time as well.

input('change camera to 12-bit; press enter\n');
['.']

averages=5;
savedimages=[0 0 0];
clear data;  % saves normalized data
clear imagedata;

h.invoke('WriteRegisterAddr',0,0,reg_globalgain,0,63);
pause(1);
['at max gain, find min integration time']

for b=1:1:5000 %(5000 => 593.4ms)
   clear image;
   h.invoke('WriteRegisterAddr',0,0,reg_integ,0,b);
   pause(0.5);
   image=h.invoke('GetRawImage');
   if (max(max(image))>3900)
      inttime=b-1;
      break;
   elseif (max(max(image))<4095)
      gainstop=b;
   end
end

h.invoke('WriteRegisterAddr',0,0,reg_integ,0,inttime);
['int time = ' num2str(inttime)]
expthresh=max(max(image))/2;
['threshold exposure = ' num2str(expthresh)]

expstart=1;

for a=1:63 %find minimum global gain

   clear image;
   h.invoke('WriteRegisterAddr',0,0,reg_globalgain,0,a);
   pause(0.5);
   image=h.invoke('GetRawImage');

   if max(max(image))>expthresh
      expstart=a;
      break;
   end

end

['expstart is ', num2str(expstart)]
['expstop  is ', num2str(63)]

h.invoke('WriteRegisterAddr',0,0,reg_globalgain,0,expstart);
pause(1);

for a=expstart:63

   h.invoke('WriteRegisterAddr',0,0,reg_globalgain,0,a);
   pause(0.2);
   Nimages=0;

   for j=1:averages

      if Nimages==averages
         break;
      end

      image=h.invoke('GetRawImage');
      image=double(image);
      if ( max(max(image))<4095 ) % && min(min(image))>0

         Nimages=Nimages+1;

         datamean = mean(mean(image));
         datastd  = std2(image);

         image=(image-datamean)./datastd; % normalize new image

         switch exist('data')
            case 0
               data=image;
            case 1
               data(:,:,size(data,3)+1)=image;
         end

      end

   end

   savedimages(1)=savedimages(2);
   savedimages(2)=savedimages(3);
   savedimages(3)=Nimages;

   if sum(savedimages)==0
```

```
    ['could not find any more images']
    break;
  end

  % average images
  imagedata=mean(data,3);

 clear data;

end
%%{
for i=0:lastimage
  for j=1:480
    for k=1:640
      eval( ['datamean(j,k)=mean(double(data(j,k,',
num2str(1), ',', num2str(1), ':images))'] );
      eval( ['datastd (j,k)= std(double(data(j,k,',
num2str(1), ',', num2str(1), ':images))'] );
    end
  end
end
%%}



%                                        h.invoke('Quit');
```

IV. SHIFT MEASURE APTINA DISCRETIZATION

```
function [measurex, measurey, measuretempx,
measuretempy] = shiftmeasure_APTINA (data)

pixelsize=2200;
upsample=1000;
B=512; % discretization levels

% set N based on ROI image
size %%%%
```

```
   if (r<N)
      for j=r+1:N
         measuretempx(k)=shiftsx(1,j)-
shiftsx(min(r,j),max(r,j));
         measuretempy(k)=shiftsy(1,j)-
shiftsy(min(r,j),max(r,j));
         k=k+1;
      end
   end

   measuretempx(k)=shiftsx(1,r);
   measuretempy(k)=shiftsy(1,r);

   measurex(r,1)=mean(measuretempx);
   measurex(r,2)=std(measuretempx);
   measurey(r,1)=mean(measuretempy);
   measurey(r,2)=std(measuretempy);

end
```

A7. CC2530 MICROCONTROLLER CODES

A. IMAGE CAPTURE AND SEND MODULE

I. MAIN

```
/*****************************************
  Filename: light_switch.c   Hadi changed to SWITCH
  Description:  This application function either as a light or a
  switch toggling the light. The role of the
  application is chosen in the menu with the joystick at initialisation.
  Push S1 to enter the menu. Choose either switch or
  light and confirm choice with S1.
  Joystick Up: Sends data from switch to light
*****************************************/
* INCLUDES
*/
#include <hal_lcd.h>
#include <hal_led.h>
#include <hal_joystick.h>
#include <hal_assert.h>
#include <hal_board.h>
#include <hal_int.h>
#include "hal_mcu.h"
#include "hal_button.h"
#include "hal_rf.h"
#include "util_lcd.h"
#include "basic_rf.h"
/*****************************************
* CONSTANTS
*/
// Application parameters
#define RF_CHANNEL                25      // 2.4 GHz RF channel
// BasicRF address definitions
#define PAN_ID              0x2007
#define SWITCH_ADDR         0x2520
#define LIGHT_ADDR          0xBEEF
#define APP_PAYLOAD_LENGTH      1
// Following two lines added by Hadi to extend switch light to two lights
#define LIGHT_CMD_BOTH          1
#define LIGHT_CMD_LEFT          2
#define LIGHT_CMD_RIGHT         3
// Application states
#define IDLE                0
#define SEND_CMD            1
// Application role
#define NONE                0
#define SWITCH              1
#define LIGHT               2
#define APP_MODES           2
/*****************************************
* LOCAL VARIABLES
*/
static uint8 pTxData[APP_PAYLOAD_LENGTH];
static uint8 pRxData[APP_PAYLOAD_LENGTH];
static basicRfCfg_t basicRfConfig;
// Mode menu
static menuItem_t pMenuItems[] =
{
  // SRF04EB and SRF05EB
  "Switch",   SWITCH,
  "Light",    LIGHT
};
static menu_t pMenu =
{
  pMenuItems,
  N_ITEMS(pMenuItems)
};
#ifdef SECURITY_CCM
// Security key
static uint8 key[]= {
    0xc0, 0xc1, 0xc2, 0xc3, 0xc4, 0xc5, 0xc6, 0xc7,
    0xc8, 0xc9, 0xca, 0xcb, 0xcc, 0xcd, 0xce, 0xcf,
};
#endif
/*****************************************
* LOCAL FUNCTIONS
*/
static void appSwitch();
static uint8 appSelectMode(void);
/*****************************************
* @fn        appSwitch
* @brief        Application code for switch application. Puts MCU in
*            endless loop to wait for commands from from switch
* @param        basicRfConfig - file scope variable. Basic RF configuration data
*            pTxData - file scope variable. Pointer to buffer for TX
```

```
*           payload
*                   appState - file scope variable. Holds application state
* @return     none
*/
static void appSwitch()
{
  halLcdWriteLine(HAL_LCD_LINE_1,           "Butterfly Ready!");
  halLcdWriteLine(HAL_LCD_LINE_2, "Fly: Up");
  halLcdWriteLine(HAL_LCD_LINE_3, "One Dir: L/R");
#ifdef ASSY_EXP4618_CC2420
  halLcdClearLine(1);
  halLcdWriteSymbol(HAL_LCD_SYMBOL_TX, 1);
#endif
  // Initialize BasicRF
  basicRfConfig.myAddr = SWITCH_ADDR;
  if(basicRfInit(&basicRfConfig)==FAILED) {
   HAL_ASSERT(FALSE);
  }
  // Keep Receiver off when not needed to save power
  basicRfReceiveOff();
  // Main loop
  while (TRUE) {
    if  (halJoystickGetDir()==HAL_JOYSTICK_EVT_RIGHT) {
      halMcuWaitMs(200);
      pTxData[0] = LIGHT_CMD_RIGHT;
      basicRfSendPacket(LIGHT_ADDR,           pTxData, APP_PAYLOAD_LENGTH);
    }
    else                                                if (halJoystickGetDir()==HAL_JOYSTICK_EVT_LEFT) {
      halMcuWaitMs(200);
      pTxData[0] = LIGHT_CMD_LEFT;
      basicRfSendPacket(LIGHT_ADDR,           pTxData, APP_PAYLOAD_LENGTH);
    }
    else                                                if (halJoystickGetDir()==HAL_JOYSTICK_EVT_UP) {
      halMcuWaitMs(200);
      pTxData[0] = LIGHT_CMD_BOTH;
      basicRfSendPacket(LIGHT_ADDR,           pTxData, APP_PAYLOAD_LENGTH);
    }
    // Put MCU to sleep. It will wake up on joystick interrupt
    halIntOff();
    halMcuSetLowPowerMode(HAL_MCU_LPM_3);  // Will turn on global
    // interrupt enable
    halIntOn();
  }
}
/*************************************************
* @fn         main

* @brief      This is the main entry of the "Light Switch" application.
*             After the application modes are chosen the switch can
*          send commands to a light device.
* @param      basicRfConfig - file scope variable. Basic RF configuration
*          data
*                   appState - file scope variable. Holds application state
* @return     none
*/
void main(void)
{
  uint8 appMode = NONE;
  // Config basicRF
  basicRfConfig.panId = PAN_ID;
  basicRfConfig.channel = RF_CHANNEL;
  basicRfConfig.ackRequest = TRUE;
#ifdef SECURITY_CCM
  basicRfConfig.securityKey = key;
#endif
  // Initalise board peripherals
  halBoardInit();
  halJoystickInit();
  // Initalise hal_rf
  if(halRfInit()==FAILED) {
   HAL_ASSERT(FALSE);
  }
  // Indicate that device is powered
  halLedSet(1);

/* Hadi Changed this part to make board directly goes to Switch App
  // Print Logo and splash screen on LCD
  utilPrintLogo("Light Switch");

  // Wait for user to press S1 to enter menu
  while (halButtonPushed()!=HAL_BUTTON_1);
  halMcuWaitMs(350);
  halLcdClear();
  // Set application role
  appMode = appSelectMode();
  halLcdClear();
  // Transmitter application
  if(appMode == SWITCH) {
    // No return from here
    appSwitch();
  }
  // Receiver application
  else if(appMode == LIGHT) {
    // No return from here
    appLight();
  }
HINT: If You Want To remove Hadi's correction, remove appSwitch(); in two lines later
*/
```

```
// Hadi Modification
    appSwitch();
    // Role is undefined. This code should not be
reached
   HAL_ASSERT(FALSE);
}
/*************************************************
*****************************************
* @fn          appSelectMode
*
* @brief      Select application mode
*
* @param      none
*
* @return     uint8 - Application mode chosen
*/
static uint8 appSelectMode(void)
{
   halLcdWriteLine(1, "Device Mode: ");

   return utilMenuSelect(&pMenu);
}
```

B. RECEIVING IMAGE MODOULE

I. MAIN PROGRAM

```
/*************************************************
 Filename: light_switch.c
 Description:  This application receives the image sent
from NORIS and sends the raw file to PC through
USB to process in Labview built-in MATLAB code for
cross-correlation. Adapted from light-switch code by
Hadi Hosseinzadegan.
 Push S1 to enter the menu. Choose either switch or
 light and confirm choice with S1.
 Joystick Up: Sends data from switch to light
*************************************/
* INCLUDES
*/
#include <hal_lcd.h>
#include <hal_led.h>
#include <hal_joystick.h>
#include <hal_assert.h>
#include <hal_board.h>
#include <hal_int.h>
#include "hal_mcu.h"
#include "hal_button.h"
#include "hal_rf.h"
#include "util_lcd.h"
#include "basic_rf.h"
* CONSTANTS
// Application parameters
#define RF_CHANNEL                25      // 2.4 GHz RF
channel
// BasicRF address definitions
#define PAN_ID              0x2007
#define SWITCH_ADDR         0x2520
#define LIGHT_ADDR          0xBEEF
#define APP_PAYLOAD_LENGTH      1
#define LIGHT_CMD_BOTH      1
#define LIGHT_CMD_LEFT      2
#define LIGHT_CMD_RIGHT     3
// Application states
#define IDLE                0
#define SEND_CMD            1
// Application role
#define NONE                0
#define SWITCH              1
#define LIGHT               2
#define APP_MODES           2
/*************************************************
* LOCAL VARIABLES
*/
static uint8 pTxData[APP_PAYLOAD_LENGTH];
static uint8 pRxData[APP_PAYLOAD_LENGTH];
static basicRfCfg_t basicRfConfig;
// Mode menu
static menuItem_t pMenuItems[] =
{
#ifdef ASSY_EXP4618_CC2420
  // Using Softbaugh 7-seg display
  " L S    ", SWITCH,
  " LIGHT  ", LIGHT
#else
  // SRF04EB and SRF05EB
  "Switch",   SWITCH,
  "Light",    LIGHT
#endif
};
static menu_t pMenu =
{
  pMenuItems,
  N_ITEMS(pMenuItems)
};
#ifdef SECURITY_CCM
// Security key
```

```
static uint8 key[]= {
   0xc0, 0xc1, 0xc2, 0xc3, 0xc4, 0xc5, 0xc6, 0xc7,
   0xc8, 0xc9, 0xca, 0xcb, 0xcc, 0xcd, 0xce, 0xcf,
};
#endif
/*************************************************
* LOCAL FUNCTIONS
*/
static void appLight();
static uint8 appSelectMode(void);
/*************************************************
* @fn          appLight
* @brief       Application code for light application. Puts MCU in endless
*              loop waiting for user input from joystick.
* @param       basicRfConfig - file scope variable. Basic RF configuration data
*              pRxData - file scope variable. Pointer to buffer for RX data
* @return      none
*/
static void appLight()
{
   halLcdWriteLine(HAL_LCD_LINE_1, "Light");
   halLcdWriteLine(HAL_LCD_LINE_2, "Ready");
#ifdef ASSY_EXP4618_CC2420
   halLcdClearLine(1);
   halLcdWriteSymbol(HAL_LCD_SYMBOL_RX, 1);
#endif
   // Initialize BasicRF
   basicRfConfig.myAddr = LIGHT_ADDR;
   if(basicRfInit(&basicRfConfig)==FAILED) {
     HAL_ASSERT(FALSE);
   }
   basicRfReceiveOn();
   // Main loop
   while (TRUE) {
      while(!basicRfPacketIsReady());
      if(basicRfReceive(pRxData, APP_PAYLOAD_LENGTH, NULL)>0) {
            if(pRxData[0] == LIGHT_CMD_BOTH) {
              halLedSet(1); halLedSet(2);
              halMcuWaitMs(2);
              halLedToggle(1); halLedToggle(2);
              halMcuWaitMs(40);
            }
         else if(pRxData[0] == LIGHT_CMD_LEFT) {
              halLedSet(1);
              halMcuWaitMs(2);
              halLedToggle(1);
              halMcuWaitMs(40);
         }
         else if(pRxData[0] == LIGHT_CMD_RIGHT) {
              halLedSet(2);
              halMcuWaitMs(2);
              halLedToggle(2);
              halMcuWaitMs(40);
         }
      }
   }
}
/*************************************************
* @fn          main
* @brief       This is the main entry of the "Light Switch" application.
*              After the application modes are chosen the switch can
*              send toggle commands to a light device.
* @param       basicRfConfig - file scope variable. Basic RF configuration
*              data
*                    appState - file scope variable. Holds application state
* @return      none
*/
void main(void)
{
   uint8 appMode = NONE;
   // Config basicRF
   basicRfConfig.panId = PAN_ID;
   basicRfConfig.channel = RF_CHANNEL;
   basicRfConfig.ackRequest = TRUE;
#ifdef SECURITY_CCM
   basicRfConfig.securityKey = key;
#endif
   // Initalise board peripherals
   halBoardInit();
   halJoystickInit();
   // Initalise hal_rf
   if(halRfInit()==FAILED) {
     HAL_ASSERT(FALSE);
   }

   // Indicate that device is powered
   halLedSet(1);
    appLight();

    // Role is undefined. This code should not be reached
   HAL_ASSERT(FALSE);
}
```

BIBLIOGRAPHY

[1] N. Yoshimizu, L. A. and C. Pollock, "Nanometrology optical ruler imaging system using diffraction from a quasiperiodic structure," *Optics Express,* vol. 18, no. 20, pp. 20827-20838, 2010.

[2] N. Amer and G. Meyer, "Novel optical approach to atomic force microscopy," *Appl. Phys. Lett.,* vol. 53, p. 1045, 1988.

[3] A. Boisen and H. O., "Noise in piezoresistive atomic force microscopy," *Nanotechnology,* vol. 10, pp. 51-60, 1999.

[4] M. Tortonese, H. Yamada, R. Barrett and C. Quate, "Atomic force microscopy using a piezoresistive cantilever," in *Solid-State Sensors and Actuators, Transducers '91,* June 1991.

[5] G. Tosolinil, G. Villanueva and J. Bausells, "Silicon microcantilevers with piezoresistive and MOSFET detection," in *Proceedings of the 2009 Spanish Conference on Electron Devices*, Santiago de Compostela, Spain , 11-13 Feb 2009 .

[6] G. Villanueva, F. Pérez-Murano, M. Zimmermann, J. Lichtenberg and J. Bausells, "Piezoresistive cantilevers in a commercial CMOS technology for intermolecular force detection," *MicroelectronicEngineering,* vol. 83, p. 1302–1305, 2006.

[7] G. Villanueva, J. Montserrat, F. Pérez-Murano, G. Rius and J. Bausells, "Submicron piezoresistive cantilevers in a CMOS-compatible technology for intermolecular force detection," *Micro and Nano Engineering 2003*, Vols. 73-74, p. 480–486, 2004.

[8] M. Ono, D. Lange, O. Brand, C. Hagleitner and H. Baltes, "A complementary-metal-oxide-semiconductor-field-effect-transistor-compatible atomic force microscopy tip fabrication process and integrated atomic force microscopy cantilevers fabricated with this process," in *Proceedings of the third International Conference on Scaning Prob e Microscopy, Sensors and Nanostructures*, 2002.

[9] E. Duriaua, T. Clarysse, T. Hantschel and W. Vandervorst, "Fabrication of cantilevers and double AFM tips for the NanoProfiler," *Microelectronic Engineering,* vol. 84, p. 1162–1167, 2007.

[10] D. Lange, T. Akiyama, C. Hagleitner, A. Tonin, H. R. Hidber, P. Niedermann, U. Staufer, N.-F. de Rooij, O. Brand and H. Baltes, "Parallel scanning AFM with on-

chip circuitry in CMOS technology," *Micro Electro Mechanical Systems, 1999. MEMS '99. Twelfth IEEE International Conference on,* pp. 447,452, 1999.

[11] N. Yoshimizu, "Atomic transition-based precision and accuracy in micro- and nanoscale systems," Cornell University, 2010.

[12] K. Cho, "Characterization of nano optical ruler system," M.Eng Project, Cornell University, May 2013.

[13] D. Steck, "Rubidium 87 D Line Data," available online at http://steck.us/alkalidata (revision 2.0.1,2 May 2008).

[14] N. Yoshimizu, A. Lal and C. Pollock, "Nanometrology Using a Quasiperiodic Pattern Diffraction OpticalRule," *J. Microelectromech.Syst.,* vol. 19, no. 4, p. 865–870, 2010.

[15] H. Vajihollahi, "TBN Project," M.Eng Project, Cornell University, May 2011.

[16] A. Ramkumar, A. Lal, D. Paduch and A. Schlegel, "An ultrasonically actuated silicon-microprobe-based testicular tubule assay," *IEEE Trans. on Biomedical Eng.,* vol. 56, no. 11, pp. 2666-267, 2009.

[17] P. Mélinon, B. Masenelli, F. Tournus and A. Perez, "Playing with carbon and silicon at the nanoscale," Nature Materials 6, 479 - 490 (2007).

[18] B. Kelly, Physics of graphite, London; Englewood, N.J.: Applied Science, 1981.

[19] K. Bolotin et al., "Ultrahigh Electron Mobility in Suspended Graphene," *Solid State Communications,* vol. 146, pp. 351-355, 2008.

[20] I. Frank and D. Tanenbaum, "Mechanical Properties of Suspended Graphene Sheets," *J. Vac. Sci. Technol.,* vol. 25, pp. 2558-2561, 2007.

[21] M. Poot and H. Van der Zant, "Nanomechanical Properties of Few-layer Graphene Membranes," *Applied Physics Letters,* vol. 92, pp. 3081-3083, 2008.

[22] Z. Ni et al., "Uniaxial Strain on Graphene: Raman Spectroscopy Study and Band-gap Opening," *ACS Nano,* vol. 2, pp. 2301-2305, 2008.

[23] C. Neto, F. Guinea and N. Peres, "The Electronic Properties of Graphene," *Review of Modern Physics,* vol. 81, pp. 109- 162, 2009.

[24] P. Huang et al., "Grains and Grain Boundaries n Single-layer Graphene Atomic Patchwork Quilts," *Nature,* vol. 469, p. 389–392, 2011.

[25] X. Li et al., "Graphene Films with Large Domain Size by a Two-step Chemical Vapor Deposition Process," *Nano Lett.,* vol. 10, p. 4328–4334, 2010.

[26] F. Xia, D. Farmer, Y.-m. Lin and P. Avouris, "Graphene Field-Effect Transistors with High On/Off Current Ratio and Large Transport Band Gap at Room Temperature," *Nano Letters* , vol. 10, no. 2, pp. 715-718, 2010.

[27] W. Thomson, "on the electrodynamic qualities of metals effects of magnetization on the electric conductivity of nickel and of iron," *Proceedings of the Royal Society of London,* vol. 8, pp. 546-550, 1856-57.

[28] M. Huang and J. Greer, "Measuring Graphene Piezoresistance via in-situ Nanoindentation," *ECS Transactions,* vol. 35, no. 3, pp. 211-216, 2011.

[29] Y. Kim et al., "Preparation of piezoresistive nano smart hybrid material based on graphene," *Current Applied Physics,* vol. 11, no. 1, pp. S350-S352, 2010.

[30] M. Allen and A. Frazier, "“Piezoreslstive Graphite/polyimide Thin Films for MicromachiningApplications”," *J. Appl. Phys.,* vol. 73, 1993.

[31] M. Cullinan and M. Culpepper, "Carbon nanotubes as piezoresistive microelectromechanical sensors: Theory and experiment," *Physical Review B,* vol. 82, no. 11, p. 115428, 2010.

[32] X. Zheng, X. Chen, J. Kim, D. Lee and X. Li, "Measurement of the gauge factor of few-layer graphene," *J. Micro/Nanolith. MEMS MOEMS* , vol. 12, no. 1, p. 013009, 2013.

[33] X. Li et al., "Large-Area Synthesis of High-Quality and Uniform Graphene Films on Copper Foils," *Science,* vol. 324, pp. 1312-1314, 2009.

[34] L. Malard, M. Pimenta, G. Dresselhaus and M. Dresselhaus, "Raman spectroscopy in graphene," *Physics Reports,* vol. 473, no. 5–6, p. 51–87, 2009.

[35] M. Berre, "Piezoresistive Properties of Boron-doped PECVD Micro- and Polycrystalline Silicon Films," *Polycrystalline Thin Films Symposium,* pp. 733-8, 1994.

[36] M. Huth, "Granular Metals: From Electronic Correlations to Strain-sensing Applications," *J. of Applied Phys.* , vol. 107, p. 113709, 2010.

[37] L. Lin, H. Chu and Y. Lu, "A Simulation Program for the Sensitivity and Linearity of Piezoresistive Pressure Sensors," *Journal of Microelectromechanical Systems,* vol. 8, pp. 514-522, 1999.

[38] Y. Kim et al., "Preparation of piezoresistive nano smart hybrid material based on graphene," *Current Applied Physics,* vol. 11, no. 1, pp. S350-S352, 2010.

[39] H. Hosseinzadegan, C. Todd, A. Lal, M. Pandey, M. Levendorf and J. Park, "Graphene Has Ultra High Piezoresistive Gauge Factor," in *25th IEEE Int. Conf. on MEMS,* Paris, France, 29 Jan - 2 Feb, 2012.

[40] A. Nath Pal, S. Ghatak, V. Kochat, S. E., A. B., S. Raghavan and A. Ghosh, "1/f noise as a probe for investigating band structure in graphene," in *American Physical Society, APS March Meeting 2011*, March 21-25, 2011.

[41] L. Vandamme and G. Leroy, "Analytical Expressions for Correction Factors for Noise Measurements with a Four-Point Probe," *Fluctuation and Noise Letters,* vol. 6, no. 2, pp. L161-L178, 2006.

[42] R. Malaric, Instrumentation and Measurement in Electrical Engineering, Brown Walker Press, 2011.

[43] Z. Cheng, Q. Li, Z. Li, Q. Zhou and Y. Fang, "Suspended Graphene Sensors with Improved Signal and Reduced Noise," *Nano Lett.,* vol. 10, no. 5, p. 1864–1868, 2010.

[44] I. Heller, S. Chatoor, J. Männik, M. Zevenbergen, J. Oostinga, A. Morpurgo, C. Dekker and S. Lemay, "Charge Noise in Graphene Transistors," *Nano Lett.,* vol. 10 , no. 5, p. 1563–1567, 2010.

[45] S. Rumyantsev, G. Liu, M. Shur, R. Potyrailo and A. Balandin, "Selective Gas Sensing with a Single Pristine Graphene Transistor," *Nano Lett.,* vol. 12, no. 5, p. 2294–2298, 2012.

[46] zzzzzzz, "Effect of Spatial Charge Inhomogeneity on 1/f Noise Behavior in Graphene".

[47] C. Liang, G. Leroy, J. Gest, L. Vandamme and J. Wojkiewicz, "1/f noise in polyaniline/polyurethane (PANI/PU) blends," *Synthetic Metals,* vol. 159, no. 1, pp. 1-6, 2009.

[48] G. Tsoukleri, J. Parthenios, K. Papagelis, R. Jalil, A. Ferrari, A. Geim, K. S. Novoselov and C. Galiotis, "Subjecting a Graphene Monolayer to Tension and Compression," *Small,* vol. 5, no. 21, p. 2397–2402, 2009.

[49] S. Habermehl and C. Carmignani, "Correlation of charge transport to local atomic strain in Si-rich silicon nitride thin films," *Appl. Phys. Lett. ,* vol. 80, no. 261, 2002.

[50] H. San, Z. Deng, Y. Yu, G. Li and X. Chen, "Study on dielectric charging in low-stress silicon nitride with the MIS structure for reliable," *J. Micromech. Microeng.* , vol. 21, p. 125019, 2011.

[51] D. Krick and P. ,. K. J. Lenahan, "Stable photoinduced paramagnetic defects in hydrogenated amorphous silicon nitride," *Appl. Phys. Lett.* , vol. 51, p. 608, 1987.

[52] J. Robertson and M. Powell, "Gap states in silicon nitride," *Appl. Phys. Lett.* , vol. 44, p. 415, 1984.

[53] S. LAU, J. SHANNON and B. SEALY, "Changes in the Poole-Frenkel coefficient with current induced defect band conductivity of hydrogenated amorphous silicon nitride," *Journal of non-crystalline solids,* vol. 227, no. 30, pp. 533-537, 1998.

[54] K. Nomura and A. MacDonald, "Quantum Hall Ferromagnetism in Graphene," *Phys. Rev. Lett.*, vol. 96, p. 256602, 2006.

[55] J. Chen, C. Jang, S. Adam, M. Fuhrer, E. Williams and M. Ishigami, "Charged-impurity scattering in graphene," *Nat Phys,* vol. 4, no. 5, pp. 377 - 381, 2008.

[56] S. Zhou, G. Gweon, A. Fedorov, P. First, W. Heer, D. Lee, F. Guinea, A. Castro Neto and A. Lanzara, "Substrate-induced bandgap opening in epitaxial graphene," *Nat Mater,* vol. 6, no. 10, pp. 770 - 775, 2007.

[57] W. Zhu, D. Neumayer, V. Perebeinos and P. Avouris, "Silicon Nitride Gate Dielectrics and Band Gap Engineering in Graphene Layers," *Nano Lett.,* vol. 10, no. 9, p. 3572–3576, 2010.

[58] M. Yang, C. Zhang, S. Wang, Y. Feng and Ariando, "Graphene on β-Si3N4: An ideal system for graphene-based electronics," *AIP Advances* , vol. 1, p. 032111, 2011.

[59] W. Wang, X. Lv and F. Sun, "Design of a novel MEMS gyroscope array," *Sensors,* vol. 13, no. 2, pp. 1651-63, 2013.

[60] M. Zalalutdinov, B. Ilic, D. Czaplewski, A. Zehnder, H. Craighead and J. Parpia, "Frequency-tunable micromechanical oscillator," *Appl. Phys. Lett.*, vol. 77, p. 3287, 2000.

[61] H. Baltes, O. Brand, A. Hierlemann, D. Lange and C. Hagleitner, "CMOS MEMS – present and future," in *15th IEEE Int. Conf. on MEMS,* 2002.

[62] S. Akin and T. Alper, "A single-crystal silicon symmetrical and decoupled MEMS gyroscope on an insulating substrate," *J. of Microelectromech. Sys.*, vol.

14, no. 4, pp. 707-717, 2005.

[63] R. Syms, "Electrothermal frequency tuning of folded and coupled vibrating micromechanical resonators," *J. Microelectromech. Syst.,* vol. 7, p. 164, 1998.

[64] K. Schwab, "Spring constant and damping constant tuning of nanomechanical resonators using a single-electron transistor," *Appl. Phys. Lett.*, vol. 80, p. 1276, 2002.

[65] V. Sazonova, Y. Yaish, H. Üstünel, D. Roundy, T. Arias and P. McEuen, "A tunable carbon nanotube electromechanical oscillator," *Nature,* vol. 431, pp. 284-287, 2004.

[66] C. Nguyen, "MEMS technologies and devices for single-chip RF front-ends," *2005 IMAPS/ACerS Int. Conf. on Cer. Intercon. and Cer. Microsys. Tech. (CICMT), Denver, Colorado,* no. April 25-26, 2006.

[67] E. Wright and P. Leland, "Resonance tuning of piezoelectric vibration energy scavenging generators using compressive axial preload," *Smart Mater. Struct.*, vol. 15, p. 1413–1420, 2006.

[68] R. Kubena et al., "Micro electrical mechanical system (MEMS) tuning using focused ion beams". US Patent Patent 2004/0085159 A1, 6 May 2004.

[69] M. Lin and L. Chiao, "Post-packaging frequency tuning of microresonators by pulsed laser deposition," *J. Micromech. Microeng.*, vol. 14, p. 1742–1747, 2004.

[70] X. Li et al., "Large-Area Synthesis of High-Quality and Uniform Graphene Films on Copper Foils," *Science,* vol. 324, pp. 1312-1314, 2009.

[71] B. Hicks, N. Yoshimizu, C. Connell, A. Lal and C. Pollock, "Tip-based patterning of HOPG and CVD graphene," *Micro and Nanotech. Sens. Sys. and App.,* p. 803104, 2011.

[72] I. Byun, D. Yoon, J. Choi, I. Hwang and D. Lee, "Nanoscale lithography on monolayer graphene using hydrogenation and oxidation," *J. ACS nano,* vol. 5, no. 8, pp. 6417-24, 2011.

[73] S. Ilanko, "Vibration and Post-buckling of In-Plane Loaded Rectangular Plates Using a Multiterm Galerkin's Method," *J. of Appl. Mech.,* vol. 69, pp. 589-592, 2002.

[74] C. Chen et al., "Performance of monolayer graphene nanomechanical resonators with electrical readout," *Nature Nanotechnology,* vol. 4, pp. 861 - 867, 2009.

[75] R. Henze, C. Pyrlik, A. Thies, J. Ward, A. Wicht and O. Benson, "Fine-tuning of whispering gallery modes in on-chip silica microdisk resonators within a full spectral range," *Appl. Phys. Lett.*, vol. 120, p. 041104, 2013.

[76] B. Hicks, "Surface patterning of highly ordered pyrolitic graphite," Masters Thesis, Cornell University, Ithaca, NY, May 2010.

[77] J. Cao, Q. Wang and H. Dai, "Electromechanical Properties of Metallic, Quasimetallic, and Semiconducting Carbon. Nanotubes under Stretching," *Physical Review Letter*, vol. 90, pp. 157601-157604, 2003.